Springer Theses
Recognizing Outstanding Ph.D. Research

Matt Thompson

Helium Nano-bubble Formation in Tungsten

Measurement with Grazing-Incidence Small Angle X-ray Scattering

Springer

Springer Theses

Recognizing Outstanding Ph.D. Research

Aims and Scope

The series "Springer Theses" brings together a selection of the very best Ph.D. theses from around the world and across the physical sciences. Nominated and endorsed by two recognized specialists, each published volume has been selected for its scientific excellence and the high impact of its contents for the pertinent field of research. For greater accessibility to non-specialists, the published versions include an extended introduction, as well as a foreword by the student's supervisor explaining the special relevance of the work for the field. As a whole, the series will provide a valuable resource both for newcomers to the research fields described, and for other scientists seeking detailed background information on special questions. Finally, it provides an accredited documentation of the valuable contributions made by today's younger generation of scientists.

Theses are accepted into the series by invited nomination only and must fulfill all of the following criteria

- They must be written in good English.
- The topic should fall within the confines of Chemistry, Physics, Earth Sciences, Engineering and related interdisciplinary fields such as Materials, Nanoscience, Chemical Engineering, Complex Systems and Biophysics.
- The work reported in the thesis must represent a significant scientific advance.
- If the thesis includes previously published material, permission to reproduce this must be gained from the respective copyright holder.
- They must have been examined and passed during the 12 months prior to nomination.
- Each thesis should include a foreword by the supervisor outlining the significance of its content.
- The theses should have a clearly defined structure including an introduction accessible to scientists not expert in that particular field.

More information about this series at http://www.springer.com/series/8790

Matt Thompson

Helium Nano-bubble Formation in Tungsten

Measurement with Grazing-Incidence Small Angle X-ray Scattering

Doctoral Thesis accepted by
the Australian National University, Canberra, Australia

Springer

Author
Dr. Matt Thompson
Research School of Physics and Engineering
Australian National University
Canberra, ACT, Australia

Supervisor
Prof. Cormac Corr
Research School of Physics and Engineering
Australian National University
Canberra, ACT, Australia

ISSN 2190-5053 ISSN 2190-5061 (electronic)
Springer Theses
ISBN 978-3-319-96010-4 ISBN 978-3-319-96011-1 (eBook)
https://doi.org/10.1007/978-3-319-96011-1

Library of Congress Control Number: 2018948597

This Springer imprint is published by the registered company Springer Nature Switzerland AG
The registered company address is: Gewerbestrasse 11, 6330 Cham, Switzerland

Supervisor's Foreword

The construction of the international plasma fusion experiment ITER represents an important step for the realisation of nuclear fusion power. In the ITER reactor, two hydrogen isotopes, deuterium and tritium, will fuse together at temperatures in excess of 150,000,000 °C to produce a heavier element, helium, one neutron and 17.6 MeV of energy. Through this process, ITER aims to deliver 500 MW of fusion power from 50 MW input power. If successful, the world will be at the threshold of realising fusion power that can provide a nearly limitless sustainable clean energy source.

The exhaust region of a fusion reactor, known as the divertor, is one of the key components as it controls the exhaust of waste gas and impurities from the reactor. The divertor material must be capable of withstanding high heat loads (more than 10 MW/m^2) due to energetic charged and neutral particle bombardment (eV to keV), as well as the high-energy neutron flux (14.1 MeV) created by the fusion reactions. Material performance under these conditions determines the component lifetime and can affect the plasma performance, and is thus a high priority issue for ITER.

Tungsten has been selected as the divertor material for ITER due to its high melting temperature, high thermal conductivity, low erosion yield and low hydrogen solubility. However, the synergistic effects of simultaneous exposure of materials to steady-state heat loads and high particle fluences are extremely complex and not well understood. The overarching goal of the research is to improve our ability to predict the performance of materials in a working fusion reactor by understanding and untangling the effects of high power plasma fluences and heat loads.

Plasma irradiation of a material creates a dynamic surface with a changing interface and changing surface morphology and chemistry. It has previously been demonstrated that low energy ($\sim$20 eV) helium ions can greatly affect the material surface, reduce thermal conductivity and can lead to significant nano-structuring of the material. The degree to which both surface morphology and subsurface defects caused by the plasma–material interaction influence the diffusion, trapping and precipitation of hydrogen and helium species into gas bubbles is an outstanding

question. This is dependent on the ion energy, fluence, surface temperature and mixed plasma species. While not fully understood, molecular dynamic simulations have provided some insight.

Although helium is insoluble in tungsten it can self-trap, allowing helium to accumulate to form clusters and eventually nano-bubbles, which result in the dislocation of tungsten atoms closer to the surface. The nano-bubbles can serve as traps for tritium, which reduces the amount of tritium available for the fusion reaction and introduces a radiological hazard. In ITER, tritium retention is limited by the nuclear licensing. Nano-bubbles have been formed up to 100 nm beneath the surface, despite an implantation depth of <2 nm, indicating that significant diffusion can occur prior to helium trapping. Once near the surface, the over-pressurised helium nano-bubbles can eventually burst. It is at temperatures above 900 K that a "nano-fuzz" structure begins to form. The "nano-fuzz" can be up to a micrometre in length and 10–50 nm in width. The formation of this "nano-fuzz" or indeed other subsurface structures is strongly dependent on surface temperature and ion energy. Above 2000 K, recrystallisation of tungsten occurs and micrometre-sized helium bubbles or large voids become apparent on the surface.

Responding to this need, Matt's Ph.D. research employed fusion-relevant plasma–surface interaction experiments under controlled conditions along with advanced material characterisation techniques to study the interaction of plasma with tungsten.

The research provided seminal results on:

(i) Quantifying changes in tungsten morphology, helium nano-bubble formation and hydrogen fuel retention.
(ii) Determining how the mechanical properties of tungsten are affected by plasma irradiation.
(iii) Understanding the impact of neutron irradiation by using ion beam irradiation as a surrogate for neutrons.

A particularly exciting aspect of his Ph.D. research is the investigation of helium nano-bubbles in tungsten using Grazing-Incidence Small Angle X-Ray Scattering (GISAXS) at the Australian Synchrotron. Matt made world-first measurements of helium nano-bubbles in tungsten exposed to plasma using GISAXS. These results have generated enormous international interest in our research. He has led this effort on the international front and has applied GISAXS to samples from the Large Helical Device in Japan, the DIII-D tokamak in the US, Magnum-PSI in the Netherlands, and Jule-PSI in Germany. Indeed, he has received numerous invitations to present international institutions and has also received invitations to present at national and international conferences.

Canberra, Australia
June 2018

Prof. Cormac Corr

Abstract

The behaviour of helium in tungsten is an important concern for the fusion materials community. Under helium plasma exposure, small nano-scale bubbles form beneath the material surface as helium precipitates from the tungsten matrix. Under certain conditions, this can lead to the subsequent formation of a surface "nano-fuzz", though the mechanisms of this process are not presently understood.

For subsurface nano-bubble formation, transmission electron microscopy (TEM) has been the most widely used technique. While certainly a powerful technique, TEM suffers from a number of significant drawbacks: sample preparation is difficult and destructive, and there are sampling limitations as nano-structures must be located and characterised individually. This makes quantitative characterisation of nano-scale modification in tungsten challenging, which in turn makes it difficult to perform systematic studies on the effects of factors such as temperature and plasma composition on nano-scale modification.

Here, Grazing-Incidence Small Angle X-ray Scattering (GISAXS) is presented as a powerful addition to the field of fusion materials. With GISAXS, one can measure the X-ray scattering from nano-scale features throughout a relatively large volume, allowing information about full nano-bubble size distributions to be obtained from a simple, non-destructive measurement. Where it typically takes days or weeks to prepare a sample and study it under TEM, GISAXS measurements can be performed in a matter of minutes, and the data analysis can be performed autonomously by a computer in hours.

This thesis describes the work establishing GISAXS as a viable technique for fusion materials. A GISAXS pattern fitting model was first developed, and then validated via comparison between GISAXS and TEM measurements of helium-induced nano-bubble formation in tungsten exposed to a helium discharge in the large helical device. Under these conditions, nano-bubbles were found to follow an approximately exponential diameter distribution, with a mean nano-bubble diameters $\mu = 0.596 \pm 0.001$ nm and $\mu = 068 \pm 0.04$ nm computed for GISAXS and TEM, respectively. Depth distributions were also approximately exponential, with average bubble depths estimated at $\tau = 9.1 \pm 0.4$ nm and $\tau = 8.4 \pm 0.5$ for GISAXS and TEM, respectively.

GISAXS was then applied to study the effects of plasma fluence, sample temperature and large transient heat and particle loads on nano-bubble formation. Nano-bubble sizes were found to saturate with increasing fluence at fluences less than 2.7×10^{24} He/m^2 at 473 K. At higher temperatures, larger nano-bubbles are able to form, suggesting a shift in the growth mechanisms, possibly from vacancy capture to bubble coalescence. Evidence is also presented which indicates that nano-bubble size distributions are qualitatively different for tungsten exposed to transient heat and particle loads due edge localised modes (ELMs) in the DIII-D tokamak, with a relatively large population of smaller (0.5–1 nm) nano-bubbles forming in this case. This is posited to be a consequence of rapid precipitation due to either extremely high helium concentrations during the ELM, or rapid cooling after it.

Finally, synergistic effects between plasma composition and sample temperature are explored to determine which factors are most relevant for hydrogen and helium retention. Here, evidence has been found that helium ions from the plasma require a minimum energy of 9.0 ± 1.4 eV in order to be implanted into tungsten. This was the dominant factor governing helium retention in this experiment. On the other hand, sample temperature is the dominant factor for hydrogen retention.

Preface

As I make the final preparations to submit this thesis, it seems appropriate to take a moment to reflect on the journey I have been on over the past 4 years of my Ph.D.. Like many aspiring Ph.D. candidates, I believed I was setting off on a great intellectual pursuit, to be carried forward by my wits and ingenuity. This, I think, was a dangerous misconception.

Within a few months of starting, the reality dawned on me that scientific discovery is more a matter of grit and determination. Rather than some great new breakthrough in the field, I seemed destined instead to produce only the most incremental of advances, producing in years what a more senior scientist could do in months. With my delusions of grandeur shattered, I turned my attention to finding some hole in the existing fusion literature I could fill.

Initially, I focussed on the problem of hydrogen retention in tungsten. It is something which has been studied widely before, but it is an important problem and was a good exercise in local expertise building. It was also a dead-end: not because we couldn't get results, but because there wasn't really much scope to build on what was already out there (well, not quite, but that's another story). This realisation led me to search out for an ever wider range of techniques which could potentially provide some new insight into damage in fusion materials.

After 18 months or so, I decided to investigate a small angle scattering technique to look for subsurface helium nano-bubbles. I had initially dismissed the idea as I expected that the bubbles would be too small to scatter strongly, and X-ray attenuation in tungsten too great. However, the opportunity to perform some scoping experiments at the Australian Synchrotron presented itself, so there was nothing to lose. To my delight, a clear scattering pattern was produced. Thus, what started as a haphazard stab in the dark quickly transformed into the core focus of my Ph.D.

From there, my project was able to recover some of the grandeur I had first envisioned in the very early days. Small angle scattering is, after all, a powerful technique which hitherto had been inaccessible to the field. Over the next year,

I worked almost exclusively on developing methods to reliably interpret the scattering data I was taking (that, I can assure you, was not trivial), and from there I began to organise new experiments to study nano-bubble formation in tungsten using the unprecedented detail available via small angle scattering.

Canberra, Australia Matt Thompson

Parts of this thesis have been published in the following articles:

The work described in this thesis has produced a significant contribution to the field of fusion materials, as evidenced by the publication output relating to this work. To date, the author has been first author in six peer-reviewed papers, and a co-author in a further two. A further manuscript is presently undergoing peer review, and another is being prepared for submission. All work listed below is relevant to this thesis.

1. M. Thompson, A. Deslandes, T.W. Morgan, R.G. Elliman, G. De Temmerman, P. Kluth, D. Riley, C.S. Corr, Observation of a helium ion energy threshold for retention in tungsten exposed to hydrogen/helium mixture plasma, Nucl. Fusion. 56 (2016) 104002. https://doi.org/10.1088/0029-5515/56/10/104002.
2. M. Thompson, R. Sakamoto, E. Bernard, N. Kirby, P. Kluth, D. Riley, C. Corr, GISAXS modelling of helium-induced nano-bubble formation in tungsten and comparison with TEM, J. Nucl. Mater. 473 (2016) 6–12. https://doi.org/10.1016/j.jnucmat.2016.01.038.
3. M. Thompson, P. Kluth, R.P.P. Doerner, N. Kirby, D. Riley, C.S.S. Corr, Measuring helium bubble diameter distributions in tungsten with grazing incidence small angle X-ray scattering (GISAXS), Phys. Scr. T167 (2016) 014014. https://doi.org/10.1088/0031-8949/2016/T167/014014.
4. R.P. Doerner, D.L. Rudakov, C.P. Chrobak, A.R. Briesemeister, C. Corr, G. De Temmerman, P. Kluth, C.J. Lasnier, A.G. McLean, D.C. Pace, R.A. Pitts, O. Schmitz, M. Thompson, V. Winters, Investigation of He-W interactions using DiMES on DIII-D, in: Phys. Scr., 2016. https://doi.org/10.1088/0031-8949/T167/1/014054.
5. M. Thompson, P. Kluth, R.P. Doerner, N. Kirby, C. Corr, Probing helium nano-bubble formation in tungsten with grazing incidence small angle X-ray scattering, Nucl. Fusion. 55 (2015) 42001. http://stacks.iop.org/0029-5515/55/i=4/a=042001.
6. M. Thompson, R. Doerner, N. Ohno, N. Kirby, P. Kluth, D. Riley, C. Corr, Measuring temperature effects on nano-bubble growth in tungsten with grazing incidence small angle X-ray scattering, Nucl. Mater. Energy. (2017). https://doi.org/10.1016/j.nme.2016.11.025.
7. M. Thompson, D. Drummond, J. Sullivan, R. Elliman, P. Kluth, N. Kirby, D. Riley, C.S. Corr, Effect of W self-implantation and He plasma exposure on early-stage defect and bubble formation in tungsten, Nucl. Fusion. 58 (2018) 66010. https://doi.org/10.1088/1741-4326/aab96c.
8. C.S. Corr, S. O'Ryan, C. Tanner, M. Thompson, J.E. Bradby, G. De Temmerman, R.G. Elliman, P. Kluth, D. Riley, Mechanical properties of tungsten following rhenium ion and helium plasma exposure, Nucl. Mater. Energy. 12 (2017). https://doi.org/10.1016/j.nme.2017.04.012.

Acknowledgements

Nothing is created in a vacuum, and this thesis is no exception. A great many people have been involved in the work which underpins this thesis in one way or another; their contributions too numerous to list in any great detail. What follows is rather an extensive list of the people who made this thesis possible, which will be presented in roughly chronological order of appearance.

First of all, I would like to thank my primary supervisor, Cormac Corr, for his patience, feedback, and support, especially during the earlier days of the project. I am especially appreciative of his assistance in connecting me with other members of the research community, and for having the confidence in me to allow me great liberty in determining the scope of my project. I will happily confess that I didn't have the faintest idea what I was doing in those early days, and I am grateful that Cormac allowed me so much time and freedom to home in on the work which now makes up the bulk of this document.

Second, my second supervisor Daniel Riley from the Australian Nuclear Science and Technology Organisation. I am grateful for many things, but in particular your support in allowing me to access many of Australia's finest research infrastructure. On that note, I would also like to thank everyone at (or formerly at) ANSTO who has contributed to my project, especially Alec Deslandes, Mihail Ionescu, Mathew Guenette, and the ANSTO Metallography team for their various contributions. Thank you also to Nigel Kirby and the team at the Australian Synchrotron's SAXS/WAXS beamline, without which I would no doubt be at least a year away from submission.

Thank you to the other members of my advisory panel, Rob Elliman and Boyd Blackwell, for your time and many valuable discussions. Thank you also to Kidane Belay, James Sullivan, and Jodie Bradby, and Patrick Kluth for your assistance with the many research facilities I have been able to access through your help.

I would also like to thank my many collaborators for their various contributions, including Greg De Temmerman, Thomas Morgan and their past and present colleagues at Dutch Institute for Fundamental Energy Research (The Netherlands), Russ Doerner from the University of California, San Diego (US), Noriyasu Ohno

from Nagoya University (Japan), Ryuichi Sakamoto from the National Institute for Fusion Science (Japan), Elodie Bernard from Aix-Marseille University (France) and Arkadi Kreter from Forschungszentrum Juelich (Germany).

Finally, I would like to thank my wife Sayoko for her patient support throughout my studies, and my son Souma for allowing me more sleep than most new parents. I dedicate this thesis to you both.

Contents

Chapter 1
Introduction

1.1 Overview

1.1.1 Fusion and ITER

ITER, Latin for *the way*, is a next-step tokamak reactor presently under construction in Cadarache in the south of France. The project is being organized as a joint venture between China, the European Union, India, Japan, Korea, Russia, and the United States, with an estimated cost now exceeding AU$18 billion [1]. ITER's goal is to push the boundaries of fusion science by achieving a total fusion power output of 500 MW, with only 50 MW of input heating power. Once completed, ITER will be the largest fusion device ever constructed, with an outer radius of the vacuum vessel of 19 m and a height of 11 m [1]. The next largest tokamak, JET, has an outer radius of 2.93 m [2].

Building a device of unprecedented scale such as ITER brings with it many challenges. Development of ITER has been based largely on empirical scaling laws derived from comparisons between smaller devices, in addition to extensive plasma modelling efforts [3–5]. However, there is a great deal of uncertainty with these calculations, particularly with respect to plasma performance after deuterium-tritium fusion ignition [6, 7]. Interactions between the plasma and wall material will also be of critical importance to ITER's performance [8]. Thus, the role of ITER will be much deeper than a technological demonstration. It will also play an important role in advancing the world's understanding of plasma physics, particularly in the regimes of interest for fusion energy, and how these plasmas behave in very large devices. Understanding plasma instabilities, which can lead to a loss of confinement and large amounts of energy being dumped on the walls, will be especially important [9–11].

M. Thompson, *Helium Nano-bubble Formation in Tungsten*, Springer Theses,
https://doi.org/10.1007/978-3-319-96011-1_1

ITER will also serve as a test bed for new technologies which may be employed in future reactors. For a commercially operating fusion reactor, some tritium breeding from lithium will need to occur within the reactor. To develop this technology, ITER will also be working with breeder blanket test modules and other technology relating to tritium production and handling [12]. ITER will also work entirely with liquid He cooled superconducting magnets. This brings with it its own challenges. Global production of Nb_3Sn superconducting wire for these magnets was increased from 15 tons to 100 tons annually over the period 2008 to 2015 to meet the demands of the ITER project [1]. As is often the case in large cutting-edge projects, the demanding requirements have also provided new opportunities for development of supporting technology which may have broad applications beyond the field of fusion energy.

1.1.2 ITER Design

Figure 1.1 shows a schematic of ITER's cross section, highlighting a number of key components [13]. The plasma's magnetic field configuration can be modified by altering the currents which flow through the toroidal and poloidal superconducting magnets. Fusion of deuterium (D) and tritium (T) will occur within the plasma core, situated roughly within the inner most magnetic contour, which will release stored nuclear energy in the form of the kinetic energy of the resultant neutrons (14.1 meV) and helium (He) ions (3.5 meV). Neutrons, which have no electric charge, will pass straight out of the plasma and deposit their energy in the beryllium (Be) first wall. He ions, on the other hand, will be charged and so will be confined within the plasma by following the closed magnetic field lines.

Perfect confinement cannot be achieved in practice, as collisions and turbulence within the plasma will eventually lead charged particles to drift outwards towards the wall. To improve plasma performance and reduce heat loads on the first wall, ITER has been designed to operate in the "divertor" magnetic field geometry [14]. Here, the magnetic field is designed such that any particles which drift outward and cross the last closed magnetic field line will be carried down towards a specially designed chamber in the lower part of the tokamak call the "divertor". Consequently the divertor, which will be made of tungsten (W), will be exposed to the highest heat and particle fluxes within the reactor. Recombination of plasma ions and electrons will occur predominantly within the divertor, either due to energy loss via collisions with gas inside the divertor, or through direct collision with the divertor walls. Once recombined, gaseous species can then be pumped out, allowing He to be removed and unspent T to be recycled.

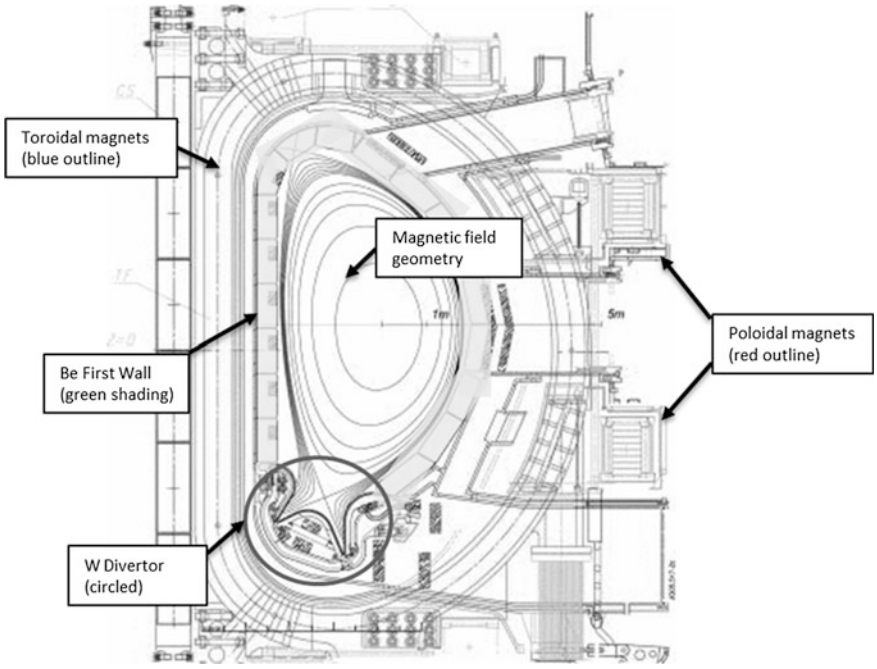

Fig. 1.1 Schematic cross-section of the ITER tokamak highlighting selected key features. The magnetic field can be controlled by altering the currents within the toroidal and poloidal superconducting magnets. The tokamak will be operated with a "divertor" magnetic field geometry, where outward drifting plasma will be carried down towards the divertor region in the bottom (circled) where ions and electrons will undergo recombination and the resultant neutral gas be pumped out of the reactor vessel. Reprinted from M.J. Rubel et al., Rev. Sci. Instrum. 77 (2006) 63501 with permission from AIP publishing [13]

1.2 Tungsten

1.2.1 The Divertor and Material Requirements

The plasma facing armour in ITER's divertor will be subject to some of the most extreme conditions of any system built by man. During burning plasma operation heat fluxes of approximately 10 MW/m^2 are expected [15], with sharp periodic thermal spikes due to transient plasma instabilities. The divertor has been designed such that ions will be neutralised before making contact with the divertor, thereby reducing the energy with which the ions impact with the walls. Most energy is instead dissipated through radiation. This configuration is known as a "detached divertor" configuration [16]. In the event of reattachment, where the plasma ions directly impinge on the first wall without first being neutralised, higher heat fluxes may be expected. To allow for this, the ITER divertor is being designed to withstand heat fluxes as high as 20 MW/m^2 [17].

The sharp periodic thermal spikes caused by transient events are not the result of "accidents" during operation, but are in fact a normal feature of high-confinement plasma operation in a tokamak. Serious disruptions may also occur over ITER's lifetime, where large amounts of the stored energy of the plasma are swiftly dumped onto the surrounding walls. Components will therefore need to perform well under repeated thermal shocks, and across a wide range of operating temperatures.[1] This latter point is especially important as there will be a large temperature gradient between the surface of a divertor tile and the cooling structure beneath it, not to mention the rapid temperature ramping and cooling during start-up and shut-down cycles.

The divertor will also be exposed to very high particle fluxes. These particles will be predominantly D and T, with a smaller amount of He "ash", Be (eroded from the first wall), W (from the divertor), and other impurity species. ITER may also be operated with pure He plasma in early stages during experiments dedicated to understanding plasma physics within the device. As a result, W performance under pure He is also important.

Divertor materials will also be exposed to neutron irradiation, which has several important implications for armour materials. First of all, neutron irradiation can lead to knock-on damage, where a collision between a neutron and W atom can transfer significant amounts of kinetic energy from the neutron to the atom, knocking it from its lattice position [18]. These knock-on atoms can then collide with other atoms, knocking more out of place and leading to the generation of defect structures such as interstitial atoms, vacancies, vacancy clusters, dislocation loops, and voids. Over ITER's lifetime, divertor components are expected to experience neutron knock-on damage rates as high as 0.5 displacements per atom (dpa) [19]. That is, on average one in two atoms will be physically displaced from its lattice site over the lifetime of the reactor. These damage rates will be much higher in any future DEMO[2] device [20–22]. A second important effect is neutron capture and transmutation, which will slowly change the tungsten to rhenium, and this rhenium to osmium [23, 24]. Material properties will be progressively changed over the life of the reactor through this chemical change, and brittle secondary phases may form, which could have an adverse impact on the mechanical properties of the divertor. Some of these transmutation events will lead to the formation of radioactive isotopes, which will lead to the progressive activation of the divertor over time. This has important implications for reactor safety and waste disposal. Finally, neutrons will be a significant source of

[1] Ideally, the steady-state operating temperature of the divertor will be maintained below $\sim$1273 K so that it remains below the recrystalisation temperature of tungsten, however, certain factors such as the shape of and spacing between divertor tiles could have a significant effect on material temperatures, especially near the corners and edges. The specific configuration of divertor tiles has been a topic of significant debate amongst the ITER divertor design team.

[2] "DEMO" is the tentative name used to describe any hypothetical fusion program aimed at developing a DEMOnstration electricity generating power station, and is widely understood within the fusion community to represent the next step after ITER. DEMO is not likely to be a single international project like ITER, but rather many separate projects run by individual countries.

heating for all armour materials. Due to their highly penetrating nature, this heating will occur throughout the volume of a material rather than conducting inward from its surface. Material activation will also lead to further heating due to radioactive decay, including when the device is not operating [25].

Presently, there are plans to replace ITER's divertor at least once over the machine's operating life [26]. As ITER is a nuclear device, and radioactivity will build up within the core, any repair or replacement must be conducted by remote handling which complicates design considerably. Divertor components must therefore be both highly reliable, and very precisely aligned to maximise performance and reduce damage to components over time [27]. Any misalignment may result in a tile receiving a much higher heat flux than it was originally designed for, while faulty joins between tiles and their cooling structures could reduce heat flow to the sink enough to lead to overheating of the surface. Adding to this challenge is the sheer scale of the divertor, which will have a total surface area of 190 m^2 and will be comprised of 54 separate modular cassettes [15].

1.2.2 Physical Properties

Tungsten (see Table 1.1), is an attractive material for the divertor as it has the highest melting point of all metals (3695 K), does not bind chemically to T (reducing T retention), does not lead to the formation of long-lived radioisotopes under neutron irradiation [28], and has a low sputtering rate under He and D plasma [29]. This low sputtering rate comes about on account of tungsten's high average atomic mass of 183.8 amu. Sputtering is caused due to momentum transfer between an impinging plasma ion and the stationary wall atoms, so momentum (and therefore energy) transfer for hydrogen (H) or He ions impacting W is generally not sufficient to overcome the bonds between W atoms. W's low chemical reactivity with H also eliminates chemical erosion, which can lead to significant mass loss in carbon-based materials.

There are many drawbacks with W, however. For a start its very high melting point makes casting materials from melt prohibitively difficult, requiring W-based materials to be fabricated by other means; typically via powder metallurgical processes [30]. W is also brittle at low temperatures which may increase its susceptibility to cracking during thermal cycling or other stresses induced by plasma exposure. Above a certain temperature, known as the ductile-to-brittle transition temperature, the ductility of W improves dramatically, but its mechanical strength is greatly diminished. This transition temperature can be changed by altering the microstructure or alloying W with other metals, and can range from 260 to 1223 K depending on the fabrication method and composition [31].

Without improving the toughness and ductility of W components under its full range of operating temperatures any plasma facing armour will need to be bonded to a substrate of a different material. This raises many technical challenges. As any fusion reactor component is expected to be exposed to high thermal gradients and

Table 1.1 Selected physical properties of pure tungsten

Property	Value
Atomic number	74
Atomic mass (amu)	183.8
Crystal structure	Body-centred cubic
Lattice constant at 20 °C (Å)	3.1585
Density (g/cm^3)	19.3
Melting point (K)	3695
Vickers hardness	3430

severe thermal cycling, thermal expansion between the armour and substrate must be matched, limiting the available options. These options are further constrained by the fact that the substrate must also be a low-activation material under neutron radiation, and must maintain its toughness and ductility after severe radiation damage. Ideally, W itself would be used as a substrate via some method of improving its thermo-mechanical properties.

There are several ways to achieve this. The most obvious option would be alloying. Rhenium (Re) is known to improve W's ductility and toughness, however due to Re's higher degree of neutron activation any addition of Re must be carefully limited to ensure that the divertor can still be classified as low-level nuclear waste after the reactor's useful life [32]. Re is also a precious metal, making this a very expensive option. An alternative option would be to use oxide dispersion [33–35]. In this approach, W is fabricated with oxide nano-particles dispersed into the matrix. These are typically yttrium-titanium oxides. These nano-particles act to anchor the corners of crystalline grains, allowing the microstructure to be optimised. Smaller grains improve ductility by increasing the density of grain boundaries, which act as sinks for defects which are generated during deformation.

W-fibre reinforced W is another option [36]. Here, the component is fabricated around W-fibres which have been coated in an oxide to enhance the pseudo-ductile behaviour of the material [37, 38]. When a crack emerges, the fibres help dissipate energy through friction as they slide against the matrix they are enclosed in rather than allowing all energy to be dissipated through crack formation. This leads to significantly improved fracture toughness. An alternative approach is through the use of W laminate materials [39]. W laminates are structures consisting of many thin foils bonded together. Individual W foils possess much greater ductility than bulk W, as the surfaces of the foil act as sink sites for defects which are generated during deformation. This improved ductility is preserved even in bulk materials consisting of many conjoined foils, provided that the interfaces between these foils can maintain their integrity.

These microstructural improvements may be compromised if the component is exposed to a higher temperature than the recrystallization temperature for W, which may destroy the desired microstructure through the formation of larger crystalline grains. Components should therefore be operated at temperatures much lower than this recrystallization temperature (the precise temperature depends on the

microstructure). This should be the case for all components except the plasma-facing armour. It is also important that these microstructural improvements do not lose their benefits even under neutron irradiation, which can lead to significant embrittlement [40].

1.2.3 Thermal Shock

Thermal shock occurs where a material is exposed to a rapid temperature rise, which may be subsequently followed by rapid cooling. This leads to large thermal stresses due to thermal expansion and contraction where materials have little time to respond to these changes. Understanding the performance of W under thermal shocks is important as plasma facing materials will be exposed to many plasma instabilities which will deposit large amounts of energy in a very short space of time. The most common of these events will be edge localised modes, which will each last 0.2–0.5 ms. Larger plasma disruptions can also occur, depositing several megajoules of energy per square metre in less than a millisecond [41].

The main consequence of thermal shocks is the formation of cracks in the W surface. Hirai et al. [42] have observed two distinctly different types of cracking behaviour for pre-heated W exposed to high thermal loads via electron heating to power densities ranging from 0.15 to 0.88 GW/m^2, which they referred to as major cracks and micro-cracks. As the name implies, major cracks are wide, deep cracks which occur as a result of the brittle nature of W. However, these disappear at higher temperatures (>473 K before thermal shocks are applied) as the metal becomes more ductile. Micro-cracks, on the other hand, are much narrower and form along grain boundaries due to plastic deformation resulting from rapid thermal expansion and subsequent contraction. At sufficiently high temperatures ($\sim$1073 K before thermal shocks) these too disappear, most likely as a consequence of W's increased ductility at higher temperatures.

Other effects may also result from rapid heat loading, including enhanced erosion, surface roughening, and surface melting. The effects of plasma loading on thermal shock behaviour is also important. Wirtz et al. [41] found W pre-loaded with H produced much denser crack networks than W without H pre-loading, which was attributed to H embrittlement and pressure build-up within the material due to H supersaturation. Some level of crack formation may be beneficial, as it provides a means for the material to compensate for stresses in subsequent thermal shock events. However, if cracking cannot fully compensate for these stresses then damage is likely to accumulate, leading to enhanced erosion and dust formation.

As with W's physical properties, resistance to thermal transients can be improved through the development of advanced materials. For instance, dispersion of titanium carbide (TiC) within the W matrix has been found to dramatically improve performance under thermal shocks, to the point where crack formation has been completely suppressed for base temperatures as low as room temperature [43].

However, this process requires careful optimisation of TiC particle sizes and W grain sizes, and development of these advanced materials is yet to be demonstrated on an industrially relevant scale.

1.2.4 Plasma Poisoning

If an impurity atom is able to enter the core plasma and is not fully ionised, collisions with plasma particles can excite the electrons within the atom to higher energy levels, which will later release this energy in the form of a photon. As photons are unaffected by the external magnetic fields they can escape from the core, carrying their energy with them. This means that where impurities are present the energy confinement of the plasma is reduced [44]. This energy loss is proportional to the atomic number of the impurity squared. All else being equal, a given number of W atoms ($Z^2 = 5476$) within the plasma core will be substantially worse than an equivalent number of carbon atoms ($Z^2 = 36$); 152 times worse, to be precise. The plasma tolerance for carbon may be much greater than implied by these numbers as carbon atoms are likely to be fully ionised in the ITER plasma core, so will have no electrons to excite. This will not be the case with W [45].

This process of impurity-driven energy losses is known as plasma poisoning, and can lead to serious plasma instabilities if impurity levels are able to build up too far. For W a concentration of 1 part per 100,000 is sufficient to prevent burning plasma operation in ITER [46]. If W is to be successfully used in ITER, it will be essential that it is not able to accumulate in the core. W accumulation will be governed by the plasma physics within the scrape-off layer (the region outside the last closed flux surface), pedestal (the region of high pressure gradients which "holds up" the high pressures of the core), and core regions of the plasma more-so than the erosion of plasma facing components. For this reason, the region of the wall where material erosion occurs is more important for impurity build-up than the magnitude of this erosion. In ASDEX-Upgrade, W migrating from the first wall was responsible for most of the W accumulation in the core, despite the divertor having an erosion rate almost an order of magnitude higher [46]. For this reason, ITER will be using a Be ($Z = 4$) first wall, and W will be limited strictly to the divertor.

For the divertor the greatest potential source of W for core impurities will be dust formation. W dust is little more than micro- or nano-scale pieces of W which have broken off from the bulk material, which can occur via many processes such as thermal shock-induced cracking [41], plasma-induced surface modification, arcing [47], or droplet formation from melted surfaces [48]. As these particles are much larger and have much greater mass than individual atoms, they are better able to penetrate through the scrape-off layer and into the plasma core. Dust formation would also increase the surface area within the reactor vessel, which would increase the potential for tritium retention, and may become airborne in an accident where the reactor vessel is breached. For these reasons, France's nuclear regulator has

imposed strict limits on the amount of dust formation which will be allowed in ITER under the terms of its operating license. Dust formation must therefore be minimised.

1.3 Helium-Induced Nanostructure Formation in W

1.3.1 He Self-Trapping and Bubble Formation

He will be an inevitable component in fusion plasma, so special attention must be given to the influence it has on W divertor performance. He is insoluble in W, with relatively large amounts of energy being required to insert it into an interstitial site. Instead, He acts as a substitutional impurity by binding strongly to vacant lattice sites [49]. If present, H will be ejected from a vacancy to accommodate an incoming He atom. For this reason He retention is relatively insensitive to H fluence in mixed plasma experiments [50]. By contrast, H retention is generally reduced in the presence of He [51, 52].

Unlike H, He exhibits self-trapping, causing a strong tendency for He to cluster [49]. As these clusters grow, many different types of nano-structures have been observed, including nano-bubbles [53–55], surface pits [56, 57], and fine hair-like structures, dubbed "nano-fuzz", which grow from the surface of W under certain conditions [58–63]. These structures are believed to be related, with He precipitation into bubbles playing a key role in their formation [64–67]. Understanding the nucleation and growth of these structures is therefore an important step in assessing the risk that helium-induced material modification poses to the operation of a fusion device such as ITER, and in particular, whether these nano-structures are likely to lead to the development of tungsten dust, or provide a source of high-Z impurities which could potentially enter the plasma core.

Experimental observation of the formation of these nano-structures is challenging, as these structures can be as small as a single He atom bound to a vacancy. Transmission electron microscopy (TEM) [54, 67, 68] and scanning electron microscopy (SEM) [59, 62, 69] are both powerful techniques when studying more advanced stages of nano-structure formation, but taken by themselves cannot provide a complete picture of the early-stage formation of these structures.

Modelling He nano-structure evolution has provided great insight into the likely (time-dependent) evolution processes of these nano-structures. For tungsten exposed to He plasma, He enters the material via an implantation process, where the He ions from the plasma are accelerated across the plasma sheath and injected a short distance below the surface. From here, He migrates via diffusion, binding with vacancies within the material where available, forming He-vacancy complexes. Complexes with less than 7 He atoms are relatively mobile, and are able to diffuse

through the material and merge with other He-vacancy complexes[3] [66]. Once they reach a critical size of approximately 7–8 atoms, He-vacancy complexes are able to relieve internal pressure through a process known as "trap mutation", where a tungsten atom in the surrounding matrix is knocked out of its lattice site and into an interstitial position. This process pins the He-vacancy complexes in place, rendering them (relatively) immobile. These structures then grow via the accumulation of smaller, more mobile He-vacancy complexes.

The presence of crystal imperfections, such as grain boundaries, has a dramatic effect on nano-bubble growth. For instance, Sefta et al. [66] found that introducing a grain boundary to their model significantly reduced the size of nano-bubbles which formed in their models. This effect was attributed to He trapping along the grain boundary, leading to the nucleation of a larger number of smaller structures.

The nano-bubbles themselves are not spherical. Molecular dynamics simulations by Smirnov et al. [64] found that He nano-bubbles grow as irregular polygons, with faces lying parallel to crystallographic planes with low Miller indices and edges lying parallel to the <111> directions. Dislocation loops formed in the vicinity of these bubbles, which in turn guided new He atoms towards the vertices of the bubble, promoting anisotropic growth.

These dynamics are very sensitive to the temperature of the material in question. Miyamoto et al. [68] provided an excellent demonstration of this in an in situ TEM experiment, where thin tungsten samples were exposed to a 3 keV He ion beam while being simultaneously imaged by TEM. For sample temperatures up to 1073 K, nano-bubble diameters appeared to saturate at around 1–2 nm (Fig. 1.2). However, at 1273 K nano-bubbles continued to grow with increasing He fluence, while the density of nano-bubbles actually declined. This experiment indicates that nano-bubbles larger than 1–2 nm grow via agglomeration of smaller bubbles, and demonstrates that even relatively large nano-bubbles are mobile at 1273 K.

1.3.2 Nano-fuzz and Dust Formation

The formation of "nano-fuzz" is of particular interest to the fusion materials research community, as it is not yet clear what impact this structure may have on the performance of tungsten-based materials. Nano-fuzz is observed to occur only in tungsten between $\sim$1000 and $\sim$2000 K, where the energy of the He ion being implanted into the material exceeds 20–30 eV [70]. This behaviour is summarised in Fig. 1.3.

[3]These numbers should be seen as indicative of behaviour, rather than definitive. Real material systems are considerably more complex than the idealised model systems used for computer simulations of material behaviour.

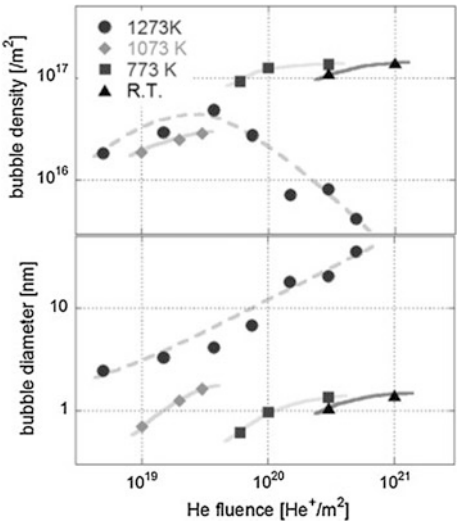

Fig. 1.2 Results from Miyamoto et al.'s [68] in situ TEM study, showing the effect of sample temperature and He ion fluence on the number density and size of He nano-bubbles in W. Used with permission

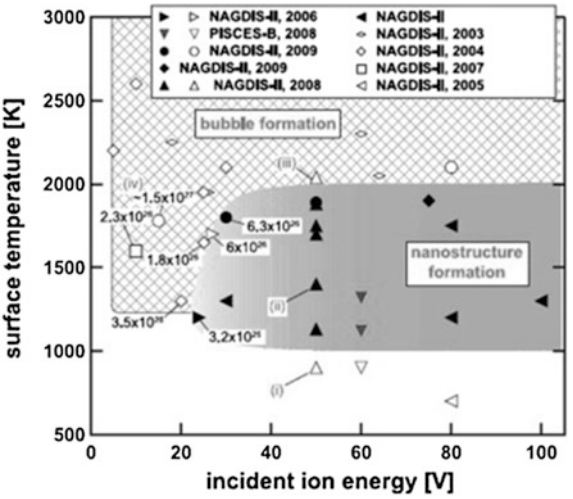

Fig. 1.3 Summary of the conditions under which nano-bubbles and nano-fuzz have been observed in W, as presented in [70]. Closed shapes indicate experiments where nano-fuzz formation was observed. Used with permission

Kajita et al. [67, 70] have suggested that nano-fuzz may form as a consequence of nano-bubbles rising to the surface and bursting, where the long, thin structures which form are the product of many repeated bubble growth and bursting cycles. This hypothesis was supported by TEM images which appear to show large helium nano-bubbles growing at the base of the fuzz-like structure, and in different stages of bursting. This view has been supported by a number of molecular dynamics models [66, 71], which at the very least demonstrate that this mechanism is

plausible.[4] Nano-bubbles are also frequently observed within the thin hairs of the tungsten fuzz itself [70].

Importantly, W loss need not occur as bubbles rupture [71], so nano-fuzz formation does not necessarily need to correspond to an increased rate of material erosion. In fact, Nishijima et al. [72] have actually noted a significant reduction in the sputtering rate of "fuzzy" tungsten surfaces under Ar exposure, which could reduce W sputtering by up to a factor of 10 for surfaces completely covered in nano-fuzz. This advantage may be offset by potentially higher rates of material loss during the transient high heat loads which will occur in ITER. For instance, simulations of these high transient heat loads with sub-millisecond laser pulses has produced melting in the outer surface of the nano-fuzz, most likely as a consequence of the lower thermal conductivity of the fuzz layer [73]. More concerning is the possibility of unipolar arcing occurring within the material, which would ablate material, enhancing erosion and introducing a potential source of high-Z impurities for the plasma. Arcing on nano-fuzz covered surfaces and its associated material loss has been demonstrated for laser-irradiated tungsten [74, 75], demonstrating the importance of developing a better understanding of He-induced nanostructure.

1.3.3 Influence of He on H Retention

Even without the formation of nano-fuzz, He induced changes in W could still have a significant impact on the performance of a fusion device such as ITER. In particular, the presence of He is known to have a significant impact on H retention. This is an important issue for ITER, as there are strict limits on the amount of tritium which may be retained within the device.

Interactions between H and He in tungsten are complicated, and are sensitive to the material temperature and the nature of the nano-structures which have developed. H and He are able to migrate via interstitial sites, however, this is a relatively high-energy state. Consequently, most retention occurs due to H or He binding with vacancy clusters, or in the case of larger voids or bubbles, the precipitation of a gaseous phase. As mentioned, He binds much more strongly to vacancies than H, and can kick out a H atom from a vacancy site [49]. As a result, He retention tends to increase as a function of He fluence, independent of the H concentration in the material. H, on the other hand, does not self-trap, so its retention within W depends on the availability of vacancies and other defect sites where H atoms can bind to. In the absence of trapping sites, excess H and He will eventually escape through the sample surface.

[4]That being said, surface diffusion may also play an important role in fuzz formation. I would encourage readers to familiarise themselves with the work of Martynenko and Nagel' [90] which presents an alternative view on how surface diffusion could be the driver behind fuzz formation.

In a room temperature experiment, Hino et al. [76] found that pre-irradiation of W with He prior to H exposure had little effect on the total H retention, but dramatically changed the way in which H was being trapped. Thermal desorption spectroscopy revealed that when He was present H was being shifted to lower-energy traps. This meant that H would be mostly released from trapping sites within the material at only 473 K, rather than 673 K for W without He. As a result, in any experiment performed above 473 K, one may expect thermal de-trapping to allow most hydrogen to escape from the material. This may be explained by the molecular dynamics modelling work of Juslin and Wirth [77], who found that where He bubbles are present H is bound in the first few W atomic layers surrounding the bubble, while being excluded from the inside of the bubble itself.

Nano-bubbles are expected to play an important role in H retention in He-exposed W. In a study by Nishijima et al. [78], W samples were pre-exposed to He plasma with material temperatures of 700 and 1600 K, before being exposed to D plasma at 550 K. Here, the 700 K He pre-exposed sample showed reduced D retention relative to a reference sample which had only been exposed to D plasma, while the 1600 K pre-exposed sample showed a six-fold increase in D retention compared to the reference sample. This dramatic increase in D retention for the 1600 K sample was attributed to the formation of micrometer-scale bubbles beneath the surface. As this example demonstrates, understanding the mechanisms which drive H retention is essential in order to understand why He is observed to both increase [52, 79], and decrease [80, 81] H retention.

In addition to temperature effects, He fluence also has a complex influence on H retention in W. Nobuta et al. [82] found that T retention increased with He pre-irradiation fluence up to 10^{17} He/cm^2, before declining at higher He fluences. This effect is believed to result from changes to the W microstructure at higher He fluence. Specifically, as He fluence increases, nano-bubbles precipitate from the matrix and generate stress-fields within the material. Eventually, these stresses lead to the formation of a network micro-cracks extending some distance into the material, which provide additional pathways for H to escape [55], and significantly reduce H diffusion into the bulk [80, 83].

1.3.4 The Importance of Statistically Significant Empirical Validation of Computational Models

Modelling efforts are essential in order to gauge the likely effects of accumulated damage over the lifetime of a fusion reactor. One of the challenges in modelling fusion reactor first wall materials is that changes can occur over a very wide range of scales—from femtoseconds to years, nanometres to metres. No single modelling technique can effectively cover such a wide range of conditions. Instead, researchers can chain modelling techniques that are better suited to different temporal or spatial scales together in an approach known as “multi-scale modelling” [84].

One of the drawbacks of a modelling approach to materials research is that errors within the model can accumulate. This is especially the case for multi-scale models, where higher scale models require information from smaller-scale models as input. The "chain" of models is therefore only as strong as its weakest link. Robust empirical validation of models is therefore essential.

Nano-bubble nucleation, migration and growth are ongoing, dynamic processes and cannot be considered in isolation. However, the scales required to model these processes differ by many orders of magnitude, necessitating several different linked models in a multi-scale approach. Migration of small H–He clusters [85] and nucleation of bubbles [86] occurs on a nm/ns scale, and is well-suited for study with molecular dynamics simulations. On the other hand, bubble migration and coalescence occur on a scale of mm/minutes (or larger/longer), making Kinetic Monte Carlo methods more appropriate [87]. For a full-scale divertor simulation, a m/year scale would be required, thereby necessitating higher and higher scale models [84].

To have any confidence in these higher-scale models, one must be able to verify that the initial parameters from the smaller-scale models are valid. Thus, these models must be able to make quantitative predictions about the behaviour of bubbles (for instance) that can be tested empirically. To date, most quantitative experimental work has focussed on measuring H or He retention through either ion beam techniques (such as [88]) or thermal desorption spectroscopy (e.g. [89]). As nano-bubbles themselves occur below the surface, they have primarily been studied via Transmission Electron Microscopy (TEM). TEM, insofar as it is relevant to this thesis, is discussed in more detail in Sect. 2.1.1. To summarise briefly here, TEM is a technique that excels at studying fine details of individual features, but is poorly suited for the study of entire populations of nano-bubbles.

Growth processes such as those behind nano-bubble formation are stochastic in nature, so population level studies are essential in order to validate nucleation and growth models. To fill this gap within the field, the author has developed Grazing Incidence Small Angle X-day Scattering (GISAXS) as a new method of obtaining population-level statistically significant information about nano-bubbles, including their (average) shapes, size distributions, and depth distributions. Competing computational models that make different assumptions about bubble growth processes can be tested against this new suite of empirical information, allowing researchers to form objective judgements about the effectiveness of these different models. This process will be essential in linking the molecular dynamics nm/ns scale of bubble nucleation to the larger mm/minute scale more relevant for bubble coalescence processes, which in turn can be linked to the truly macroscopic m/year scale of materials engineering.

1.4 Thesis Outline

The work described within this thesis is concerned primarily with the formation of nano-scale structures in W exposed to He or mixed H/He plasma. To achieve this, the synchrotron based technique GISAXS has been applied to the study of fusion materials for the first time. This pioneering work represents the single most significant contribution the author has made to the field of fusion materials at the time of submission, and is the main focus of this document.

Chapter 2 introduces the GISAXS technique and its use to study nano-bubble formation in W, and provides a detailed description of the scattering model and fitting algorithm which was used for GISAXS pattern analysis. This model is then benchmarked against TEM data in Chap. 3, demonstrating excellent agreement between these two very different techniques. In Chaps. 4 and 5 GISAXS is then applied to the study of nano-bubble formation in W under varying plasma fluence and temperature (respectively).

Chapter 6 then shifts focus to the broader problem of synergistic effects of temperature, plasma composition, and radiation damage on H and He retention in W, and nano-structure formation. Here, GISAXS is used to determine whether nano-bubbles are present, and estimate their sizes where they are. The key findings of this thesis are then presented in Chap. 7, along with a brief discussion of how this work has contributed to the field of fusion materials research.

References

1. ITER, Vacuum Vessel, Online (2015)
2. A.W. Edwards, D.J. Campbell, W.W. Engelhardt, H.-U. Fahrbach, R.D. Gill, R.S. Granetz, S. Tsuji, B.J.D. Tubbing, A. Weller, J. Wesson, D. Zasche, Rapid collapse of a plasma sawtooth oscillation in the JET tokamak. Phys. Rev. Lett. **57**, 210–213 (1986). https://doi.org/10.1103/PhysRevLett.57.210
3. R. Albanese, G. Ambrosino, E. Coccorese, A. Pironti, J.B. Lister, D.J. Ward, Modelling and engineering aspects of the plasma shape control in ITER, in *19th Symposium Fusion Technology SOFT* (1996)
4. G.P. Maddison, E.S. Hotston, D. Reiter, P. Boerner, T. Baelmans, Towards fully authentic modelling of ITER divertor plasmas, in *18th European Conference Control Fusion Plasma Physics* (1991)
5. R.D. Pillsbury jr, J.H. Schultz, Modelling of plasma start-up in ITER. Magn. IEEE Trans. **28**, 1462–1465 (1992). https://doi.org/10.1109/20.123971
6. B.J. Green, I.I. Team, P. Teams, ITER: burning plasma physics experiment. Plasma Phys. Control. Fusion **45**, 687 (2003). http://stacks.iop.org/0741-3335/45/i=5/a=312
7. Y. Shimomura, Y. Murakami, A.R. Polevoi, P. Barabaschi, V. Mukhovatov, M. Shimada, ITER: opportunity of burning plasma studies. Plasma Phys. Control. Fusion **43**, A385 (2001). http://stacks.iop.org/0741-3335/43/i=12A/a=329

8. G.F. Matthews, M. Beurskens, S. Brezinsek, M. Groth, E. Joffrin, A. Loving, M. Kear, M.-L. Mayoral, R. Neu, P. Prior, V. Riccardo, F. Rimini, M. Rubel, G. Sips, E. Villedieu, P. de Vries, M.L. Watkins, E.-J. contributors, JET ITER-like wall—overview and experimental programme. Phys. Scr. **2011**, 14001 (2011). http://stacks.iop.org/1402-4896/2011/i=T145/a=014001
9. G. Federici, P. Andrew, P. Barabaschi, J. Brooks, R. Doerner, A. Geier, A. Herrmann, G. Janeschitz, K. Krieger, A. Kukushkin, A. Loarte, R. Neu, G. Saibene, M. Shimada, G. Strohmayer, M. Sugihara, Key ITER plasma edge and plasma–material interaction issues. J. Nucl. Mater. **313–316**, 11–22 (2003). https://doi.org/10.1016/S0022-3115(02)01327-2
10. R.A. Pitts, S. Carpentier, F. Escourbiac, T. Hirai, V. Komarov, S. Lisgo, A.S. Kukushkin, A. Loarte, M. Merola, A. Sashala Naik, R. Mitteau, M. Sugihara, B. Bazylev, P.C. Stangeby, A full tungsten divertor for ITER: physics issues and design status. J. Nucl. Mater. **438**, S48–S56 (2013). https://doi.org/10.1016/j.jnucmat.2013.01.008
11. A. Loarte, B. Lipschultz, A.. Kukushkin, G.. Matthews, P.. Stangeby, N. Asakura, G.. Counsell, G. Federici, A. Kallenbach, K. Krieger, A. Mahdavi, V. Philipps, D. Reiter, J. Roth, J. Strachan, D. Whyte, R. Doerner, T. Eich, W. Fundamenski, A. Herrmann, M. Fenstermacher, P. Ghendrih, M. Groth, A. Kirschner, S. Konoshima, B. LaBombard, P. Lang, A.. Leonard, P. Monier-Garbet, R. Neu, H. Pacher, B. Pegourie, R. Pitts, S. Takamura, J. Terry, E. Tsitrone, the I.S.L. and D. Group, Chapter 4: Power and particle control. Nucl. Fusion **47**, S203–S263 (2007). https://doi.org/10.1088/0029-5515/47/6/s04
12. D. Demange, C.G. Alecu, N. Bekris, O. Borisevich, B. Bornschein, S. Fischer, N. Gramlich, Z. Köllö, T.L. Le, R. Michling, F. Priester, M. Röllig, M. Schlösser, S. Stämmler, M. Sturm, R. Wagner, S. Welte, Overview of R&D at TLK for process and analytical issues on tritium management in breeder blankets of ITER and {DEMO}. Fusion Eng. Des. **87**, 1206–1213 (2012). https://doi.org/10.1016/j.fusengdes.2012.02.105
13. M.J. Rubel, G. De Temmerman, J.P. Coad, J. Vince, J.R. Drake, F. Le Guern, A. Murari, R.A. Pitts, C. Walker, Mirror test for international thermonuclear experimental reactor at the JET tokamak: an overview of the program. Rev. Sci. Instrum. **77**, 63501 (2006). https://doi.org/10.1063/1.2202915
14. F. Wagner, G. Becker, K. Behringer, D. Campbell, A. Eberhagen, W. Engelhardt, G. Fussmann, O. Gehre, J. Gernhardt, G.V. Gierke, G. Haas, M. Huang, F. Karger, M. Keilhacker, O. Klüber, M. Kornherr, K. Lackner, G. Lisitano, G.G. Lister, H.M. Mayer, D. Meisel, E.R. Müller, H. Murmann, H. Niedermeyer, W. Poschenrieder, H. Rapp, H. Röhr, F. Schneider, G. Siller, E. Speth, A. Stäbler, K.H. Steuer, G. Venus, O. Vollmer, Z. Yü, Regime of improved confinement and high beta in neutral-beam-heated divertor discharges of the ASDEX tokamak. Phys. Rev. Lett. **49**, 1408–1412 (1982). https://doi.org/10.1103/physrevlett.49.1408
15. M. Merola, D. Loesser, A. Martin, P. Chappuis, R. Mitteau, V. Komarov, R.A. Pitts, S. Gicquel, V. Barabash, L. Giancarli, J. Palmer, M. Nakahira, A. Loarte, D. Campbell, R. Eaton, A. Kukushkin, M. Sugihara, F. Zhang, C.S. Kim, R. Raffray, L. Ferrand, D. Yao, S. Sadakov, A. Furmanek, V. Rozov, T. Hirai, F. Escourbiac, T. Jokinen, B. Calcagno, S. Mori, ITER plasma-facing components. Fusion Eng. Des. **85**, 2312–2322 (2010). https://doi.org/10.1016/j.fusengdes.2010.09.013
16. O. Gruber, A. Kallenbach, M. Kaufmann, K. Lackner, V. Mertens, J. Neuhauser, F. Ryter, H. Zohm, M. Bessenrodt-Weberpals, K. Büchl, S. Fiedler, A. Field, C. Fuchs, C. Garcia-Rosales, G. Haas, A. Herrmann, W. Herrmann, S. Hirsch, W. Köppendörfer, P. Lang, G. Lieder, K. Mast, C. Pitcher, M. Schittenhelm, J. Stober, W. Suttrop, M. Troppmann, M. Weinlich, M. Albrecht, M. Alexander, K. Asmussen, M. Ballico, K. Behler, K. Behringer, H. Bosch, M. Brambilla, A. Carlson, D. Coster, L. Cupido, H. DeBlank, S. De Pena Hempel, S. Deschka, C. Dorn, R. Drube, R. Dux, A. Eberhagen, W. Engelhardt, H. Fahrbach, H. Feist, D. Fieg, G. Fu beta mann, O. Gehre, J. Gernhardt, P. Ignacz, B. Jüttner, W. Junker, T. Kass, K. Kiemer, H. Kollotzek, M. Kornherr, K. Krieger, B. Kurzan, R. Lang, M. Laux, Observation of continuous divertor detachment in H-mode discharges in ASDEX upgrade. Phys. Rev. Lett. **74**, 4217–4220 (1995). https://doi.org/10.1103/physrevlett.74.4217

17. T. Hirai, F. Escourbiac, S. Carpentier-Chouchana, A. Fedosov, L. Ferrand, T. Jokinen, V. Komarov, A. Kukushkin, M. Merola, R. Mitteau, R.A. Pitts, W. Shu, M. Sugihara, B. Riccardi, S. Suzuki, R. Villari, ITER tungsten divertor design development and qualification program. Fusion Eng. Des. **88**, 1798–1801 (2013). https://doi.org/10.1016/j.fusengdes.2013.05.010
18. M.R. Gilbert, J. Marian, J.-C. Sublet, Energy spectra of primary knock-on atoms under neutron irradiation. J. Nucl. Mater. **467**, 121–134 (2015). https://doi.org/10.1016/j.jnucmat.2015.09.023
19. R. Villari, V. Barabash, F. Escourbiac, L. Ferrand, T. Hirai, V. Komarov, M. Loughlin, M. Merola, F. Moro, L. Petrizzi, S. Podda, E. Polunovsky, G. Brolatti, Nuclear analysis of the ITER full-tungsten divertor. Fusion Eng. Des. **88**, 2006–2010 (2013). https://doi.org/10.1016/j.fusengdes.2013.02.156
20. D. Stork, P. Agostini, J.L. Boutard, D. Buckthorpe, E. Diegele, S.L. Dudarev, C. English, G. Federici, M.R. Gilbert, S. Gonzalez, A. Ibarra, C. Linsmeier, A. Li Puma, G. Marbach, P.F. Morris, L.W. Packer, B. Raj, M. Rieth, M.Q. Tran, D.J. Ward, S.J. Zinkle, Developing structural, high-heat flux and plasma facing materials for a near-term DEMO fusion power plant: the EU assessment. J. Nucl. Mater. **455**, 277–291 (2014). https://doi.org/10.1016/j.jnucmat.2014.06.014
21. M.R. Gilbert, Comparative assessment of material performance in DEMO fusion reactors. Fusion Sci. Technol. **66** (2014). https://doi.org/10.13182/fst13-751
22. J.W. Coenen, S. Antusch, M. Aumann, W. Biel, J. Du, J. Engels, S. Heuer, A. Houben, T. Hoeschen, B. Jasper, F. Koch, J. Linke, A. Litnovsky, Y. Mao, R. Neu, G. Pintsuk, J. Riesch, M. Rasinski, J. Reiser, M. Rieth, A. Terra, B. Unterberg, T. Weber, T. Wegener, J.-H. You, C. Linsmeier, Materials for DEMO and reactor applications—boundary conditions and new concepts. Phys. Scr. **T167**, 14002 (2016). https://doi.org/10.1088/0031-8949/2016/T167/014002
23. U. Fischer, P. Pereslavtsev, A. Möslang, M. Rieth, Transmutation and activation analysis for divertor materials in a HCLL-type fusion power reactor. J. Nucl. Mater. **386–388**, 789–792 (2009). https://doi.org/10.1016/j.jnucmat.2008.12.221
24. T. Tanno, A. Hasegawa, J.C. He, M. Fujiwara, M. Satou, S. Nogami, K. Abe, T. Shishido, Effects of transmutation elements on the microstructural evolution and electrical resistivity of neutron-irradiated tungsten. J. Nucl. Mater. **386–388**, 218–221 (2009). https://doi.org/10.1016/j.jnucmat.2008.12.091
25. H. Sakane, Y. Kasugai, M. Shibata, T. Iida, A. Takahashi, T. Fukahori, K. Kawade, Measurement of activation cross-sections of (n, np + d) reactions producing short-lived nuclei in the energy range between 13.4 and 14.9 MeV using an intense neutron source OKTAVIAN. Ann. Nucl. Energy **29**, 53–66 (2002). https://doi.org/10.1016/S0306-4549(01)00025-1
26. S. Esqué, C. van Hille, R. Ranz, C. Damiani, J. Palmer, D. Hamilton, Progress in the design, R&D and procurement preparation of the ITER divertor remote handling system. Fusion Eng. Des. **89**, 2373–2377 (2014). https://doi.org/10.1016/j.fusengdes.2014.01.060
27. F. Escourbiac, M. Richou, R. Guigon, S. Constans, A. Durocher, M. Merola, J. Schlosser, B. Riccardi, A. Grosman, Definition of acceptance criteria for the ITER divertor plasma-facing components through systematic experimental analysis. Phys. Scr. **T138**, 14002 (2009). https://doi.org/10.1088/0031-8949/2009/T138/014002
28. K. Seidel, R. Eichin, R. Forrest, H. Freiesleben, S. Goncharov, V. Kovalchuk, D. Markovskij, D. Maximov, S. Unholzer, Activation experiment with tungsten in fusion peak neutron field. J. Nucl. Mater. **329–333**, 1629–1632 (2004). https://doi.org/10.1016/j.jnucmat.2004.04.145
29. W. Eckstein, J. László, Sputtering of tungsten and molybdenum. J. Nucl. Mater. **183**, 19–24 (1991). https://doi.org/10.1016/0022-3115(91)90466-K

30. V. Krsjak, S.H. Wei, S. Antusch, Y. Dai, Mechanical properties of tungsten in the transition temperature range. J. Nucl. Mater. **450**, 81–87 (2014). https://doi.org/10.1016/j.jnucmat.2013.11.019
31. Q. Yan, X. Zhang, T. Wang, C. Yang, C. Ge, Effect of hot working process on the mechanical properties of tungsten materials. J. Nucl. Mater. **442**, S233–S236 (2013). https://doi.org/10.1016/j.jnucmat.2013.01.307
32. A. Jaber, L. El-Guebaly, A. Robinson, D. Henderson, T. Renk, Rhenium and molybdenum coatings for dendritic tungsten armors of plasma facing components: concept, problems, and solutions. Fusion Eng. Des. **87**, 641–645 (2012). https://doi.org/10.1016/j.fusengdes.2012.01.041
33. R. Liu, Y. Zhou, T. Hao, T. Zhang, X.P. Wang, C.S. Liu, Q.F. Fang, Microwave synthesis and properties of fine-grained oxides dispersion strengthened tungsten. J. Nucl. Mater. **424**, 171–175 (2012). https://doi.org/10.1016/j.jnucmat.2012.03.008
34. R. Liu, Z.M. Xie, T. Hao, Y. Zhou, X.P. Wang, Q.F. Fang, C.S. Liu, Fabricating high performance tungsten alloys through zirconium micro-alloying and nano-sized yttria dispersion strengthening. J. Nucl. Mater. **451**, 35–39 (2014). https://doi.org/10.1016/j.jnucmat.2014.03.029
35. Z. Zhou, J. Tan, D. Qu, G. Pintsuk, M. Rödig, J. Linke, Basic characterization of oxide dispersion strengthened fine-grained tungsten based materials fabricated by mechanical alloying and spark plasma sintering. J. Nucl. Mater. **431**, 202–205 (2012). https://doi.org/10.1016/j.jnucmat.2011.11.039
36. J. Du, T. Höschen, M. Rasinski, S. Wurster, W. Grosinger, J.-H. You, Feasibility study of a tungsten wire-reinforced tungsten matrix composite with ZrOx interfacial coatings. Compos. Sci. Technol. **70**, 1482–1489 (2010). https://doi.org/10.1016/j.compscitech.2010.04.028
37. J. Riesch, J.-Y. Buffiere, T. Höschen, M. di Michiel, M. Scheel, C. Linsmeier, J.-H. You, In situ synchrotron tomography estimation of toughening effect by semi-ductile fibre reinforcement in a tungsten-fibre-reinforced tungsten composite system. Acta Mater. **61**, 7060–7071 (2013). https://doi.org/10.1016/j.actamat.2013.07.035
38. J.W. Coenen, Y. Mao, J. Almanstötter, A. Calvo, S. Sistla, H. Gietl, B. Jasper, J. Riesch, M. Rieth, G. Pintsuk, F. Klein, A. Litnovsky, A.V. Mueller, T. Wegener, J.-H. You, C. Broeckmann, C. Garcia-Rosales, R. Neu, C. Linsmeier, Advanced materials for a damage resilient divertor concept for DEMO: powder-metallurgical tungsten-fibre reinforced tungsten. Fusion Eng. Des. (2016). https://doi.org/10.1016/j.fusengdes.2016.12.006
39. J. Reiser, M. Rieth, A. Möslang, B. Dafferner, A. Hoffmann, X. Yi, D.E.J. Armstrong, Tungsten foil laminate for structural divertor applications—Tensile test properties of tungsten foil. J. Nucl. Mater. **434**, 357–366 (2013). https://doi.org/10.1016/j.jnucmat.2012.12.003
40. R. Neu, J. Riesch, J.W. Coenen, J. Brinkmann, A. Calvo, S. Elgeti, C. García-Rosales, H. Greuner, T. Hoeschen, G. Holzner, F. Klein, F. Koch, C. Linsmeier, A. Litnovsky, T. Wegener, S. Wurster, J.-H. You, Advanced tungsten materials for plasma-facing components of DEMO and fusion power plants. Fusion Eng. Des. **109**, 1046–1052 (2016). https://doi.org/10.1016/j.fusengdes.2016.01.027
41. M. Wirtz, J. Linke, G. Pintsuk, G. De Temmerman, G.M. Wright, Thermal shock behaviour of tungsten after high flux H-plasma loading. J. Nucl. Mater. **443**, 497–501 (2013). https://doi.org/10.1016/j.jnucmat.2013.08.002
42. T. Hirai, G. Pintsuk, J. Linke, M. Batilliot, Cracking failure study of ITER-reference tungsten grade under single pulse thermal shock loads at elevated temperatures. J. Nucl. Mater. **390–391**, 751–754 (2009). https://doi.org/10.1016/j.jnucmat.2009.01.313
43. G. Pintsuk, H. Kurishita, J. Linke, H. Arakawa, S. Matsuo, T. Sakamoto, S. Kobayashi, K. Nakai, Thermal shock response of fine- and ultra-fine-grained tungsten-based materials. Phys. Scr. **2011**, 14060 (2011). http://stacks.iop.org/1402-4896/2011/i=T145/a=014060

44. T. Pütterich, R. Neu, R. Dux, A.D. Whiteford, M.G. O'Mullane, H.P. Summers and the ASDEX Upgrade Team, Calculation and experimental test of the cooling factor of tungsten. Nucl. Fusion **50**, 25012 (2010). https://doi.org/10.1088/0029-5515/50/2/025012
45. T Pütterich, R Neu1, R Dux, A D Whiteford, M G O'Mullane and the ASDEX Upgrade Team, Modelling of measured tungsten spectra from ASDEX Upgrade and predictions for ITER. Plasma Phys. Control. Fusion **50**, 85016 (2008). https://doi.org/10.1088/0741-3335/50/8/085016
46. V. Philipps, Tungsten as material for plasma-facing components in fusion devices. J. Nucl. Mater. **415**, S2–S9 (2011). https://doi.org/10.1016/j.jnucmat.2011.01.110
47. D L Rudakov, C P C Wong, R P Doerner, G M Wright, T Abrams, M J Baldwin, J A Boedo, A R Briesemeister, C P Chrobak, H Y Guo, E M Hollmann, A G McLean, M E Fenstermacher, C J Lasnier, A W Leonard, R A Moyer, D C Pace, D M Thomas and J G Watkins, Exposures of tungsten nanostructures to divertor plasmas in DIII-D. Phys. Scr. **T167**, 14055 (2016). https://doi.org/10.1088/0031-8949/t167/1/014055
48. G F Matthews, B Bazylev, A Baron-Wiechec, J Coenen, K Heinola, V Kiptily, H Maier, C Reux, V Riccardo, F Rimini, G Sergienko, V Thompson, A Widdowson and JET Contributors, Melt damage to the JET ITER-like Wall and divertor. Phys. Scr. **T167**, 14070 (2016). https://doi.org/10.1088/0031-8949/t167/1/014070
49. K.O.E. Henriksson, K. Nordlund, A. Krasheninnikov, J. Keinonen, Difference in formation of hydrogen and helium clusters in tungsten. Appl. Phys. Lett. **87** (2005). http://dx.doi.org/10.1063/1.2103390
50. H.T.T. Lee, A.A.A. Haasz, J.W.W. Davis, R.G.G. Macaulay-Newcombe, D.G.G. Whyte, G. M.M. Wright, Hydrogen and helium trapping in tungsten under simultaneous irradiations. J. Nucl. Mater. **363–365**, 898–903 (2007). https://doi.org/10.1016/j.jnucmat.2007.01.111
51. Y. Ueda, H.Y.Y. Peng, H.T.T. Lee, N. Ohno, S. Kajita, N. Yoshida, R. Doerner, G. De Temmerman, V. Alimov, G. Wright, G. De Temmerman, V. Alimov, G. Wright, Helim effects on tungsten surface morphology and deuterium retention. J. Nucl. Mater. **442**, S267–S272 (2013). https://doi.org/10.1016/j.jnucmat.2012.10.023
52. Y. Sakoi, M. Miyamoto, K. Ono, M. Sakamoto, Helium irradiation effects on deuterium retention in tungsten. J. Nucl. Mater. **442**, S715–S718 (2013). https://doi.org/10.1016/j.jnucmat.2012.10.003
53. E. Bernard, R. Sakamoto, N. Yoshida, H. Yamada, Temperature impact on W surface exposed to He plasma in LHD and its consequences for the material properties. J. Nucl. Mater. **463**, 316–319 (2015). https://doi.org/10.1016/j.jnucmat.2014.11.041
54. S. Kajita, N. Yoshida, R. Yoshihara, N. Ohno, T. Yokochi, M. Tokitani, S. Takamura, TEM analysis of high temperature annealed W nanostructure surfaces. J. Nucl. Mater. **421**, 22–27 (2012). https://doi.org/10.1016/j.jnucmat.2011.11.044
55. M. Miyamoto, D. Nishijima, M.J.J. Baldwin, R.P.P. Doerner, Y. Ueda, K. Yasunaga, N. Yoshida, K. Ono, Microscopic damage of tungsten exposed to deuterium-helium mixture plasma in PISCES and its impacts on retention property. J. Nucl. Mater. **415**, S657–S660 (2011). https://doi.org/10.1016/j.jnucmat.2011.01.008
56. D. Nishijima, M.Y. Ye, N. Ohno, S. Takamura, Formation mechanisms of bubbles and holes on tungsten surface with low-energy and high-flux helium plasma irradiation in NAGDIS-II. J. Nucl. Mater. **329–333**, 1029–1033 (2004). https://doi.org/10.1016/j.jnucmat.2004.04.129
57. D. Nishijima, M.Y. Ye, N. Ohno, S. Takamura, Incident ion energy dependence of bubble formation on tungsten surface with low energy and high flux helium plasma irradiation. J. Nucl. Mater. **313–316**, 97–101 (2003). https://doi.org/10.1016/S0022-3115(02)01368-5
58. M.J. Baldwin, R.P. Doerner, Helium induced nanoscopic morphology on tungsten under fusion relevant plasma conditions. Nucl. Fusion **48**, 35001 (2008). http://stacks.iop.org/0029-5515/48/i=3/a=035001
59. M.J. Baldwin, R.P. Doerner, Formation of helium induced nanostructure “fuzz” on various tungsten grades. J. Nucl. Mater. **404**, 165–173 (2010). https://doi.org/10.1016/j.jnucmat.2010.06.034

60. M.J. Baldwin, R.P. Doerner, W.R. Wampler, D. Nishijima, T. Lynch, M. Miyamoto, Effect of He on D retention in W exposed to low-energy, high-fluence (D, He, Ar) mixture plasmas. Nucl. Fusion **51**, 103021 (2011). http://stacks.iop.org/0029-5515/51/i=10/a=103021
61. G.M. Wright, D. Brunner, M.J. Baldwin, R.P. Doerner, B. Labombard, B. Lipschultz, J.L. Terry, D.G. Whyte, Tungsten nano-tendril growth in the Alcator C-Mod divertor. Nucl. Fusion **52**, 42003 (2012). http://stacks.iop.org/0029-5515/52/i=4/a=042003
62. M.J. Baldwin, T.C. Lynch, R.P. Doerner, J.H. Yu, Nanostructure formation on tungsten exposed to low-pressure rf helium plasmas: a study of ion energy threshold and early stage growth. J. Nucl. Mater. **415**, S104–S107 (2011). https://doi.org/10.1016/j.jnucmat.2010.10.050
63. M. Yamagiwa, S. Kajita, N. Ohno, M. Takagi, N. Yoshida, R. Yoshihara, W. Sakaguchi, H. Kurishita, Helium bubble formation on tungsten in dependence of fabrication method. J. Nucl. Mater. **417**, 499–503 (2011). https://doi.org/10.1016/j.jnucmat.2011.02.007
64. R.D. Smirnov, S.I. Krasheninnikov, J. Guterl, Atomistic modeling of growth and coalescence of helium nano-bubbles in tungsten. J. Nucl. Mater. **463**, 359–362 (2015). https://doi.org/10.1016/j.jnucmat.2014.10.033
65. S. Sharafat, A. Takahashi, K. Nagasawa, N. Ghoniem, A description of stress driven bubble growth of helium implanted tungsten. J. Nucl. Mater. **389**, 203–212 (2009). https://doi.org/10.1016/j.jnucmat.2009.02.027
66. F. Sefta, K.D. Hammond, N. Juslin, B.D. Wirth, Tungsten surface evolution by helium bubble nucleation, growth and rupture. Nucl. Fusion **53**, 73015 (2013). https://doi.org/10.1088/0029-5515/53/7/073015
67. S. Kajita, N. Yoshida, R. Yoshihara, N. Ohno, M. Yamagiwa, TEM observation of the growth process of helium nanobubbles on tungsten: Nanostructure formation mechanism. J. Nucl. Mater. **418**, 152–158 (2011). https://doi.org/10.1016/j.jnucmat.2011.06.026
68. M. Miyamoto, S. Mikami, H. Nagashima, N. Iijima, D. Nishijima, R.P. Doerner, N. Yoshida, H. Watanabe, Y. Ueda, A. Sagara, Systematic investigation of the formation behavior of helium bubbles in tungsten. J. Nucl. Mater. **463**, 333–336 (2015). https://doi.org/10.1016/j.jnucmat.2014.10.098
69. M.J.J. Baldwin, R.P.P. Doerner, D. Nishijima, K. Tokunaga, Y. Ueda, The effects of high fluence mixed-species (deuterium, helium, beryllium) plasma interactions with tungsten. J. Nucl. Mater. **390–391**, 886–890 (2009). https://doi.org/10.1016/j.jnucmat.2009.01.247
70. S. Kajita, W. Sakaguchi, N. Ohno, N. Yoshida, T. Saeki, Formation process of tungsten nanostructure by the exposure to helium plasma under fusion relevant plasma conditions. Nucl. Fusion **49**, 95005 (2009). https://doi.org/10.1088/0029-5515/49/9/095005
71. K.O.E. Henriksson, K. Nordlund, J. Keinonen, Molecular dynamics simulations of helium cluster formation in tungsten. Nucl. Instrum. Meth. Phys. Res. Sect. B Beam Interact. Mater. Atoms. **244**, 377–391 (2006). https://doi.org/10.1016/j.nimb.2005.10.020
72. D. Nishijima, M.J. Baldwin, R.P. Doerner, J.H. Yu, Sputtering properties of tungsten "fuzzy" surfaces. J. Nucl. Mater. **415**, S96–S99 (2011). https://doi.org/10.1016/j.jnucmat.2010.12.017
73. S. Kajita, S. Takamura, N. Ohno, D. Nishijima, H. Iwakiri, N. Yoshida, Sub-ms laser pulse irradiation on tungsten target damaged by exposure to helium plasma. Nucl. Fusion **47**, 1358–1366 (2007). https://doi.org/10.1088/0029-5515/47/9/038
74. S. Kajita, S. Takamura, N. Ohno, Prompt ignition of a unipolar arc on helium irradiated tungsten. Nucl. Fusion **49**, 32002 (2009). https://doi.org/10.1088/0029-5515/49/3/032002
75. S. Kajita, N. Ohno, S. Takamura, Tungsten blow-off in response to the ignition of arcing: revival of arcing issue in future fusion devices. J. Nucl. Mater. **415**, S42–S45 (2011). https://doi.org/10.1016/j.jnucmat.2010.08.030
76. T. Hino, K. Koyama, Y. Yamauchi, Y. Hirohata, Hydrogen retention properties of polycrystalline tungsten and helium irradiated tungsten. Fusion Eng. Des. **39–40**, 227–233 (1998). https://doi.org/10.1016/S0920-3796(98)00157-4
77. N. Juslin, B.D. Wirth, Molecular dynamics simulation of the effect of sub-surface helium bubbles on hydrogen retention in tungsten. J. Nucl. Mater. **438**, S1221–S1223 (2013). https://doi.org/10.1016/j.jnucmat.2013.01.270

78. D. Nishijima, T. Sugimoto, H. Iwakiri, M.Y. Ye, N. Ohno, N. Yoshida, S. Takamura, Characteristic changes of deuterium retention on tungsten surfaces due to low-energy helium plasma pre-exposure. J. Nucl. Mater. **337–339**, 927–931 (2005). https://doi.org/10.1016/j.jnucmat.2004.10.011
79. K. Tokunaga, T. Fujiwara, K. Ezato, S. Suzuki, M. Akiba, H. Kurishita, S. Nagata, B. Tsuchiya, A. Tonegawa, N. Yoshida, Effects of high heat flux hydrogen and helium mixture beam irradiation on surface modification and hydrogen retention in tungsten materials. J. Nucl. Mater. **390–391**, 916–920 (2009). https://doi.org/10.1016/j.jnucmat.2009.01.235
80. M. Miyamoto, D. Nishijima, Y. Ueda, R.P. Doerner, H. Kurishita, M.J. Baldwin, S. Morito, K. Ono, J. Hanna, Observations of suppressed retention and blistering for tungsten exposed to deuterium–helium mixture plasmas. Nucl. Fusion **49**, 65035 (2009). https://doi.org/10.1088/0029-5515/49/6/065035
81. V.K. Alimov, W.M. Shu, J. Roth, K. Sugiyama, S. Lindig, M. Balden, K. Isobe, T. Yamanishi, Surface morphology and deuterium retention in tungsten exposed to low-energy, high flux pure and helium-seeded deuterium plasmas. Phys. Scr. **T138**, 14048 (2009). https://doi.org/10.1088/0031-8949/2009/T138/014048
82. Y. Nobuta, Y. Hatano, M. Matsuyama, S. Abe, Y. Yamauchi, T. Hino, Helium irradiation effects on tritium retention and long-term tritium release properties in polycrystalline tungsten. J. Nucl. Mater. **463**, 993–996 (2015). https://doi.org/10.1016/j.jnucmat.2014.12.047
83. H.T. Lee, N. Tanaka, Y. Ohtsuka, Y. Ueda, Ion-driven permeation of deuterium through tungsten under simultaneous helium and deuterium irradiation. J. Nucl. Mater. **415**, S696–S700 (2011)
84. J. Knaster, A. Moeslang, T. Muroga, Materials research for fusion. Nat. Phys. **12**, 424–434 (2016). https://doi.org/10.1038/nphys3735
85. P. Grigorev, D. Terentyev, G. Bonny, E.E. Zhurkin, G. van Oost, J.-M. Noterdaeme, Mobility of hydrogen-helium clusters in tungsten studied by molecular dynamics. J. Nucl. Mater. **474**, 143–149 (2016). https://doi.org/10.1016/j.jnucmat.2016.03.022
86. R. Kobayashi, T. Hattori, T. Tamura, S. Ogata, A molecular dynamics study on bubble growth in tungsten under helium irradiation. J. Nucl. Mater. **463**, 1071–1074 (2015). https://doi.org/10.1016/j.jnucmat.2014.12.049
87. S. Sharafat, A. Takahashi, Q. Hu, N.M. Ghoniem, A description of bubble growth and gas release of helium implanted tungsten. J. Nucl. Mater. **386–388**, 900–903 (2009)
88. E. Markina, M. Mayer, H.T. Lee, Measurement of He and H depth profiles in tungsten using ERDA with medium heavy ion beams. Nucl. Instrum. Meth. Phys. Res. B. **269**, 3094–3097 (2011)
89. Y. Zayachuk, M.H.J. 't Hoen, I. Uytdenhouwen, G. van Oost, Thermal desorption spectroscopy of W–Ta alloys, exposed to high-flux deuterium plasma. Phys. Scr. **T145**, 14041 (2011). https://doi.org/10.1088/0031-8949/2011/t145/014041
90. Y.V. Martynenko, M.Y. Nagel, Model of fuzz formation on a tungsten surface. Plasma Phys. Reports **38**, 996–999 (2012). https://doi.org/10.1134/S1063780X12110074

Chapter 2
Developing a GISAXS Model to Enable Study of Nano-bubble Formation

2.1 The Case for Grazing-Incidence Small Angle X-ray Scattering (GISAXS)

2.1.1 Limitations of TEM as a Tool to Study Nano-structures in W

Materials scientists have access to a wide range of characterisation techniques, each with their own strengths and shortcomings. Thus, to understand why GISAXS is important to future fusion materials research, it is instructive to first review the role of TEM in this field.

Much of the present understanding of He-induced nano-structure formation in W has come from detailed TEM studies; whether it be the experimental evidence for bubble bursting driving nano-fuzz growth shown by Kajita et al. [1], or the nano-scale crack networks observed by Miyamoto et al. [2] which inhibit H diffusion into the bulk. Considering the critical role that TEM plays in many areas of material science, it is worth taking a moment to consider what the technique actually does. Given the extraordinary depth and breadth of TEM, it would be well beyond the scope of this thesis to discuss the technique in any great detail. For the sake of brevity, this discussion will focus mostly on the shortcomings of the technique which are most relevant to the latter part of this chapter. For a more comprehensive overview of the technique, readers are referred to the outstanding text by Williams and Carter [3].

TEM is performed by passing a highly coherent electron beam through a sample, as summarised in Fig. 2.1. A well-focussed electron beam scatters from the sample and then is focused into a high-magnification image in the imaging plane of the instrument via a series of electromagnetic lenses. By using high energy electrons (typically >30 keV), the resolution limits imposed by the electron wavelength can be minimised. Generally, resolution is not limited by diffraction. As electrons must be able to pass *through* the sample, the sample itself must be made thin enough to

M. Thompson, *Helium Nano-bubble Formation in Tungsten*, Springer Theses,
https://doi.org/10.1007/978-3-319-96011-1_2

be transparent to electrons. This typically means up to a few hundred nanometres thick at most. To reduce multiple scattering of electrons within the sample, which reduces image quality, samples should ideally be made as thin as possible.

This presents two challenges. First of all, the process of thinning a bulk sample to nano-scale thicknesses is time-consuming, and one must be careful that the methods used do not introduce artefacts which may affect the structures the researcher is studying. One must also be mindful of the fact that surface effects are likely to be much more significant in thin samples than bulk ones. The other challenge is that this process requires one to cut their sample, damaging it and making it unsuitable for further study with many other techniques. One common method for preparing W samples for TEM is to cut a cross-sectional TEM specimen from the sample of interest using a focused-ion beam (FIB). Samples are typically no more than a few millimetres wide.

The actual volume imaged in a typical TEM study is very small, and will generally be smaller the higher the magnification required. TEM is therefore at its best when used to study fine details in small regions of a sample, but does suffer from sampling limitations. If generalizations about large volumes of the sample are required, one must be careful to prepare many specimens from different regions of the sample. For instance, grain boundaries act as defect sinks, so bubble growth in these regions is likely to differ substantially from other parts of the sample. Grain orientation is also known to have a significant influence on He-induced nanostructure formation [4]. Accounting for these differences may be difficult in practice. A proper statistical analysis should then be performed, to provide some indication of the sampling limitations.

An excellent demonstration of TEM is the study performed by Miyamoto et al. [5], which describes a systematic investigation designed to determine how

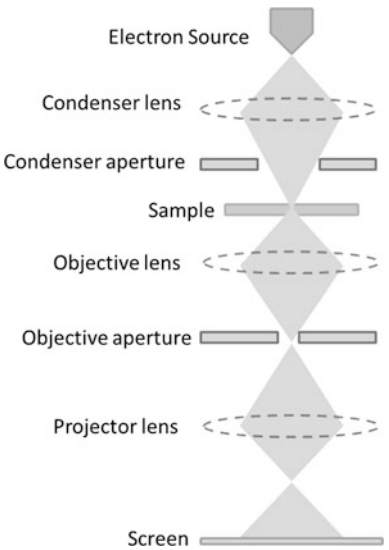

Fig. 2.1 Simplified schematic of a TEM operating in bright field imaging mode. Electrons are generated by an electron gun at the top of the column before being focussed into a small beam in the sample plane by the condenser lens. Electrons are then forward scattered from the sample and focussed onto a screen by the objective and projector lenses. Apertures are used to control beam intensity and reduce imaging defects such as spherical aberration from imperfect lenses

temperature affects the formation of He nano-bubbles in tungsten, and includes a detailed in situ experiment where W was irradiated with a He ion beam under TEM. In this paper, the authors present a dozen or so TEM micrographs from different samples which have been exposed to He plasma at different temperatures, and under different plasma fluences (see Fig. 2.2 for examples). This would have been a very time-intensive process, with data taken from only a small part of the plasma-exposed surface. Average nano-bubble diameters were estimated, but no attempt was made to describe their size distributions. A comprehensive study of this nature is a valuable contribution to the field of fusion materials research, but ultimately suffers from the sampling limitations of TEM.

Small-angle scattering (SAS) techniques are much better suited to studying sample-wide properties such as nano-bubble size distributions as much larger volumes can be probed, allowing one to gain information on millions of structures simultaneously. In these techniques, a scattering pattern is produced from either neutrons or X-rays which are incident on the sample. Unlike conventional X-ray or neutron diffraction, which are used to study the spacing and arrangement of individual atoms, SAS focusses on studying the properties of larger structures, hence scattering occurs at smaller angles. As He nano-bubbles in W occur within tens or hundreds of nanometres from the sample surface, SAS experiments are best performed in a grazing incidence to maximise the path length of the X-rays or neutrons within the volume in which bubbles are present. In particular, grazing incidence

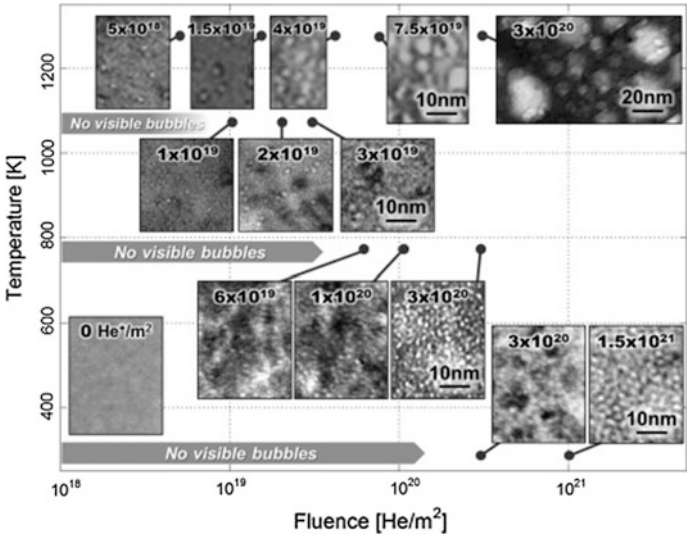

Fig. 2.2 Bright-field TEM images taken by Miyamoto et al. [5] showing nano-bubble formation in W for samples exposed to in situ He ion implantation for sample temperatures of 293, 773, 1073, and 1273 K. Qualitative differences are readily apparent between samples, but difficult to quantify. Used with permission

small-angle X-ray scattering has been found to be well-suited to studying this problem, and is a powerful, non-destructive alternative to the use of TEM to study He nano-bubble size distributions in W.

2.1.2 GISAXS Overview

Grazing Incidence Small Angle X-ray Scattering (GISAXS) works by illuminating a material with a highly collimated, monochromatic X-ray beam, then measuring the diffracted intensity at small angles opposite the incident beam. X-rays scatter from electrons, both free and bound, and so for scattering to occur there must be some fluctuation in the electron density within the material. It does not matter whether the fluctuation in electron density is lower, such as a void, or higher, due to a high density inclusion, both particles will produce identical scattering patterns. This phenomenon is known as Babinet's principle [6], and is widely employed in the field of small angle scattering. For He nano-bubbles in W, the electron density is much lower in the bubble than in the matrix, so one would expect some scattering to occur for this system.

GISAXS was originally developed as a tool to study thin polymer films [7], and is now used to study a wide range of material systems including thin films [8, 9], interfaces [10], surface and sub-surface nano-structures [11], and in situ nano-structure growth [12]. Standard small angle scattering techniques use a transmission geometry. If samples are not sufficiently thick scattering can be weak, which makes measurement difficult. By aligning the sample such that the incident X-ray beam strikes the sample at a grazing angle, the X-ray path length within the material can be increased, leading to much stronger scattering. This scattering intensity can be further increased by depositing the film on a substrate with a lower index of refraction to allow total external reflection at the interface at low angles.

Modifying the incidence angle can also be used to change the depth sensitivity of the measurement [13]. At smaller angles (from sample surface), the X-ray beam must pass through more material to reach the same depth as an X-ray beam incident at a higher angle. For features buried beneath the sample surface one can select an incident angle that provides good X-ray illumination of the features of interest, while excluding the bulk signal below. He nano-bubble formation in W occurs predominantly within a few tens of nanometres from the material surface. By using incident X-rays at grazing incidence scattering from this region can be maximised, with minimal interference from bulk scattering.

The use of grazing incidence angles brings with it its own challenges. The incident X-ray beam must be highly collimated to reduce the angular deviation of the X-ray beam. W absorbs X-rays strongly, so the X-ray source must be very intense to compensate (interestingly, polymers have the opposite problem: weak scattering means higher intensities are required to compensate). And one must be

careful to avoid X-ray absorption edges, which can lead to X-ray fluorescence and much stronger absorption. These conditions are best achieved with a synchrotron light source.

2.1.3 GISAXS Beamline Setup

All GISAXS measurements described in this thesis were performed at the Australian Synchrotron (AS) on the SAXS/WAXS beamline. In a synchrotron, high energy electrons are confined in a polygonal "storage ring". To maximise the intensity of radiation coming into the SAXS/WAXS beamline electrons are passed through an "undulator" which is inserted into the storage ring. In the undulator, the electrons are forced to oscillate by a periodic magnetic structure, which causes the electron to emit highly collimated synchrotron radiation during each oscillation. This radiation is composed of X-rays of the characteristic frequency of the undulator, along with its higher harmonics [14]. A synchrotron X-ray beam can also be generated simply from the bending magnets used at each corner of the storage ring, however, the X-rays would be less collimated and the intensity generated by this set-up would be much lower.

Figure 2.3 shows a simplified schematic of a GISAXS synchrotron beamline. Monochromatic X-rays are required for GISAXS measurements, so the polychromatic radiation from the undulator must first be passed through a monochromator. For the AS SAXS/WAXS beamline a double crystal monochromator is used, which allows one to select any wavelength for an experiment. After this, the X-ray beam is then collimated using a series of slits to reduce the beam divergence. To minimise scattering from X-ray collisions with air molecules, both the X-ray optical components and detector are kept under vacuum, with only the sample holder exposed to atmosphere. Kapton windows are used to allow X-rays to pass from regions of vacuum to atmosphere. Kapton is a polymide film composed of the chemical elements H, C, N and O, and is used for the low atomic numbers of its constituent elements and for the fact that it can be fabricated into strong yet very thin sheets. These features mean fewer electrons are available to scatter X-rays as they pass through the windows.

Samples are mounted on a motorised sample stage. To align a sample, it is first raised into the X-ray beam until the X-ray intensity is reduced by half. The sample is then rotated to maximise the X-ray intensity, before being raised once more into the beam from below. This process is outlined in Fig. 2.4, and ensures that the sample surface lies parallel to the incident X-ray beam for a nominal incident angle of 0°.

After scattering from the sample, X-rays pass through a second kapton window into the detector chamber. The detector, a Dectris—Pilatus 1 M 2D CCD array, is mounted on a moveable stage, allowing one to adjust the sample-detector distance.

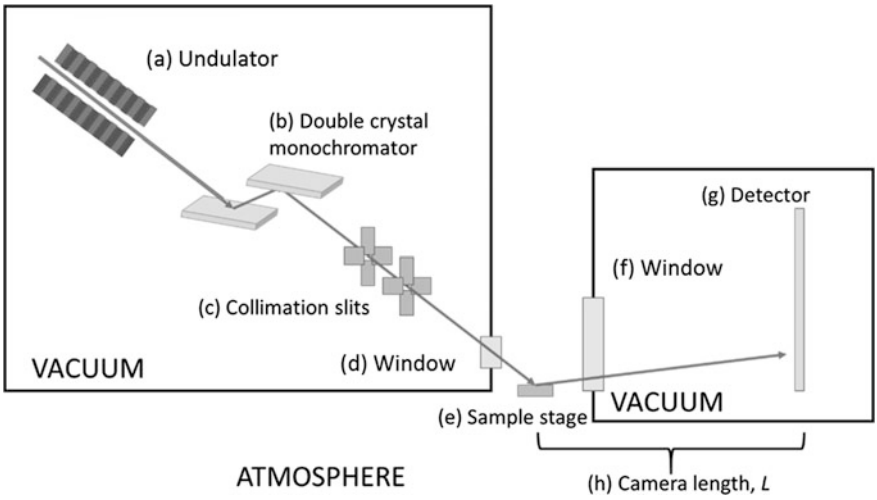

Fig. 2.3 Schematic of a synchrotron GISAXS beamline. High-intensity synchrotron radiation is generated by forcing electrons to oscillate by passing them through a periodic magnetic structure known as an "undulator" (**a**), before unwanted wavelengths are filtered out with a monochromators (**b**). The beam is then collimated to reduce beam divergence (**c**). A thin kapton window (**d**) is used to separate these optical components from the sample stage (**e**) to reduce stray scattering. Scattered X-rays pass through a second kapton window (**f**) towards the detector (**g**), which is also held under vacuum. The camera length (**h**), *L*, is the distance from the sample to the detector, and can be adjusted to probe different size features

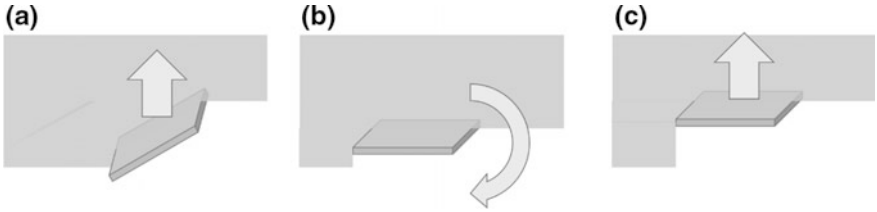

Fig. 2.4 Illustration of the GISAXS sample alignment procedure. **a** Samples are first raised into the X-ray beam at a nominal incident angle of 0° until the intensity is reduced by half. **b** Next, they are rotated until the beam intensity is maximised, ensuring the surface lies parallel to the X-ray beam. **c** Finally, the sample is raised once more into the beam until the intensity is reduced by half again

This distance is known as the "camera length", and can be adjusted to measure X-ray scattering at different angular ranges. To compensate for gaps between CCD modules in the detector, for each scattering pattern three X-ray exposures are performed where the detector is translated diagonally between each exposure (Fig. 2.5).

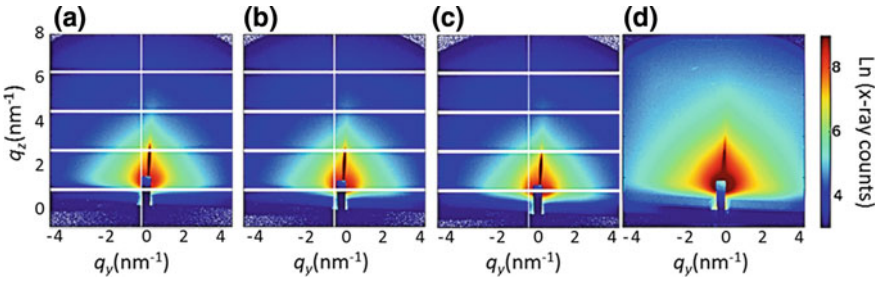

Fig. 2.5 Three X-ray scattering patterns are taken for each measurement (**a**–**c**) which are then combined into a single image (**d**) for analysis. These images show the natural log of the raw data. q_y and q_z are defined in Eq. 2.12

2.2 Building a GISAXS Model to Facilitate Analysis of He Nano-bubble Formation

2.2.1 Model Overview

X-ray scattering occurs primarily from electrons, so X-ray scattering patterns form as a consequence of electron density fluctuations within a material. For He-filled nano-bubbles in W, the electron density in the bubbles is obviously much lower than that in the W matrix, so strong scattering can occur. One of the challenges with X-ray scattering techniques is that there may be many potential structures in a material which can produce a given scattering pattern. At the detector, scattered X-rays have both a definite change in direction and phase relative to the incident beam. However, X-ray detectors are only able to measure the number of X-rays which strike them (i.e. intensity); all phase information is lost.[1] This means that real-space information about structures in the material must be reconstructed from incomplete information.

Due to this loss of information, real-space structures cannot be reconstructed from an inverse Fourier transform of the scattering pattern. Instead, accurate determination of the sizes/shapes of diffracting particles is best done by fitting a model to the experimental data. Making an appropriate choice of particle model is thus essential. In practice, one generally has some idea about what structures are present within a material. In the current case nano-bubbles in tungsten are the structures of interest. A good starting point would be to model scattering from spherical particles, which could later be generalised to spheroidal or ellipsoidal particles. Obviously, when looking at a scattering pattern with 1,000,000+ diffracting particles the model will never be truly representative of all of them, but

[1]This isn't strictly true. It is possible to reconstruct phase information form scattered X-rays using a technique known as phase contrast imaging. While not relevant to this thesis, the interested reader is referred to a discussion of the technique in Ref. [15].

some quick generalisations can be sufficient to produce a solid approximation. In a sense, one can model the "average" properties of the particles, rather than their individual natures.

The remainder of this chapter aims to provide a concise overview of the GISAXS model which was developed to facilitate the work described in the subsequent chapters of this thesis. In addition, it is hoped that this section will be of use to others who are starting out with small-angle scattering techniques, and in particular those who may be contemplating writing fitting software of their own.

2.2.2 X-ray Propagation Through Materials

For photon energies above $\sim$30 eV, the optical properties of materials can be described in terms of atomic scattering factors. In particular, the refractive index n is given by [16]:

$$n = 1 - \frac{r_e}{2\pi}\lambda^2 \sum_i N_i f_i(0, E) \tag{2.1}$$

where r_e is the classical electron radius, λ the X-ray wavelength, N_i the number of atoms of type i per unit volume, and $f_i(0, E)$ the atomic scattering factor in the forward direction[2] for atoms of type i. E emphasises the energy (equivalently, wavelength) dependence of the function. $f(0, E)$ is complex, and can be expressed in terms of its real and imaginary components as:

$$f(0, E) = f_0(0) + f_1(E) + if_2(E) \tag{2.2}$$

The imaginary component, f_2, comes about due to photo-absorption within the material, and is proportional to the absorption cross-section of the material, σ_a:

$$f_2(E) = \frac{\sigma_a}{2r_e\lambda} \tag{2.3}$$

Note that the absorption cross-section itself varies with photon energy. $f_0(0)$ is approximately equal to the atomic number, Z, minus a small relativistic correction factor:

$$f_0(0) \approx Z^* = Z - (Z/82.5)^{2.37} \tag{2.4}$$

In the absence of absorption, $f_1(E) = 0$. In this case, the sum $\sum_i N_i f_i(0, E)$ is approximately equal to the electron density [17]. As W has a relatively high atomic number (Z = 74), the binding energies of inner electrons are on the order of tens of

[2]This is the direction where the scattering vector, $\boldsymbol{q}$ = 0, hence the 0. $\boldsymbol{q}$ is defined in Eq. 2.12.

keV, so absorption effects cannot be ignored except at very high X-ray energies (i.e. much higher than the binding energies of the material's innermost electrons). Where absorption effects cannot be neglected, $f_1(E)$ can be calculated from $f_2(E)$ using the Kramers-Kronig mathematical relations, giving:

$$f_1(E) = \frac{1}{\pi r_e hc} \int_0^\infty \frac{E'^2 \sigma_a(E')}{E^2 - E'^2} dE' \tag{2.5}$$

Here, h is Planck's constant, c is the speed of light, and E is the energy of the photon. Figure 2.6 shows the atomic scattering factors for W for X-ray energies of interest to GISAXS at the Australian Synchrotron [18]. At the ionisation energies of inner electron orbitals, sharp changes in both $f_1(E)$ and $f_2(E)$ can be seen, which come about due to increased photoelectric absorption at these energies.

The refractive index can alternatively be re-written in terms of its real and imaginary contributions as:

$$n = 1 - \delta - i\beta \tag{2.6}$$

where:

$$\delta = \frac{r_e}{2\pi} \lambda^2 \sum_i N_i \left(f_{0,i}(0) + f_{1,i}(E) \right) \tag{2.7}$$

$$\beta = \frac{r_e}{2\pi} \lambda^2 \sum_i N_i f_{2,i}(E) \tag{2.8}$$

This notation is useful, as the real part, δ, governs refraction within the material, while the imaginary part, β, governs attenuation. For 10 keV $\left(\lambda = 1.24\text{Å}\right)$ X-rays in W, $\delta = 2.79 \times 10^{-5}$, and $\beta = 1.78 \times 10^{-6}$ [19]. The linear attenuation factor of the material, μ, can be readily calculated from β by [20]:

$$\mu = 4\pi\beta/\lambda \tag{2.9}$$

As the refractive index is somewhat less than 1, an X-ray may be totally externally reflected if it is incident below the critical angle for the vacuum-material (or atmosphere-material) interface. For X-rays incident from vacuum (n = 1), the critical angle, α_c, is:

$$\alpha_c = \sqrt{2\delta} \tag{2.10}$$

Even where total external reflection does occur, an evanescent wave is able to penetrate a short distance beneath the surface of the material, so scattering from sub-surface features is still possible for X-rays incident below the critical angle. However, the shallow depth of this wave would require any diffracting particle to be very close to the sample surface. Consequently, by using X-rays which are incident

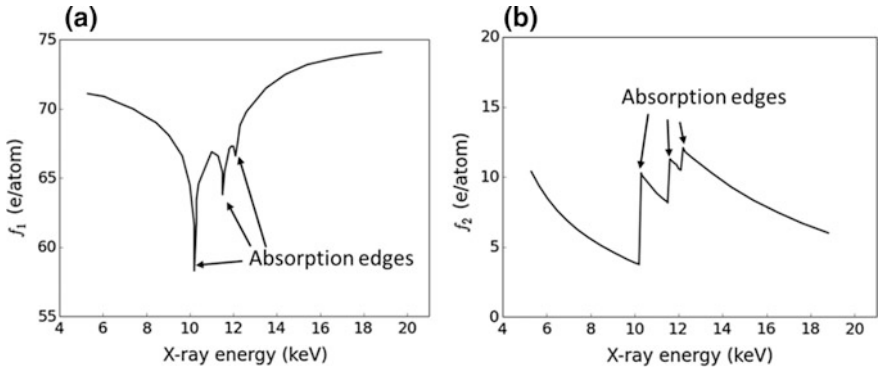

Fig. 2.6 **a** real and **b** imaginary components of the atomic scattering factor for W between 5 and 20 keV. At energies corresponding to the binding energies of inner electron orbitals sharp changes in the scattering factor are observed. Figure generated from data obtained from [18]

at an angle below the critical angle, one would produce scattering almost exclusively from the near-surface region of the material.

2.2.3 The GISAXS "Master Equation"

For monochromatic X-rays incident on a flat surface the diffracted intensity from uniform particles suspended beneath the surface at any point in the detector plane is given by [21]:

$$I \propto |T(\alpha_i)|^2 \left|T\left(\alpha_f\right)\right|^2 V^2 |F(\boldsymbol{q}')|^2 |S(\boldsymbol{q}')| A\left(\alpha_i, \alpha_f\right) \tag{2.11}$$

Each of the individual elements of this equation will be described in detail in the subsequent sections, including the mathematics used in the GISAXS model developed for pattern fitting. In short, $T(\alpha_i)$ and $T\left(\alpha_f\right)$ are the Fresnel transmission coefficients for incident and emergent X-rays, respectively, V the scattering particles' volume, $F(\boldsymbol{q}')$ is the scattering particles' form factor, $S(\boldsymbol{q}')$ is their structure factor, and $A\left(\alpha_i, \alpha_f\right)$ is an attenuation factor to account for intensity loss of X-rays as they travel through the material. α_i and α_f are the incident and emergent angles the X-rays make with the plane of the sample surface. $\boldsymbol{q}'$ is the scattering vector within the medium. This quantity will be described shortly. Throughout this thesis, the prime symbol will be used to indicate a quantity within the material matrix, while the absence of this symbol indicates a value in vacuum. These various angles are illustrated in Fig. 2.7.

For the incident and scattered X-rays, we can define wavevectors $\boldsymbol{k}^i$ and $\boldsymbol{k}^f$ which are aligned with their respective X-ray and have a magnitude $2\pi/\lambda$ (see Fig. 2.7). Outside the material the scattering vector $\boldsymbol{q}$ is given by the difference

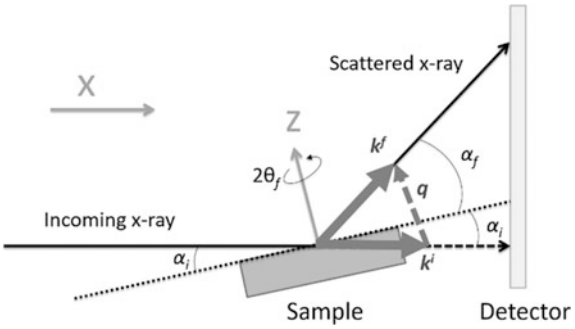

Fig. 2.7 Naming conventions for axes, angles and vectors in GISAXS are shown [22]. The direction of the y-axis is out of the page. Used with permission

between the scattered and incident wavevectors. For scattering at small angles the x-components of each wavevector are approximately equal (i.e. $q_x = k_x^f - k_x^i \approx 0$), allowing $\boldsymbol{q}$ to be approximated as:

$$\boldsymbol{q} = \boldsymbol{k^f} - \boldsymbol{k^i} = \begin{bmatrix} q_y \\ q_z \end{bmatrix} = \frac{2\pi}{\lambda} \begin{bmatrix} \sin(2\theta_f)\cos(\alpha_f) \\ \sin(\alpha_f) + \sin(\alpha_i) \end{bmatrix} \tag{2.12}$$

Here, $2\theta_f$ (rather than θ_f) is the azimuthal angle of the emergent X-ray, in line with the conventions used in Bragg scattering. The incident X-ray is assumed to lie in the x-z plane, so $2\theta_i = 0$. In Eq. 2.11 the scattering vector in the medium $\boldsymbol{q}'$, not the scattering vector in vacuum $\boldsymbol{q}$, is needed. This can be determined by accounting for refraction, and is given by (see Sect. 2.2.2):

$$\boldsymbol{q}' = \frac{2\pi}{\lambda} \begin{bmatrix} \sin(2\theta_f)\cos(\alpha_f) \\ \sqrt{n^2 - \cos^2(\alpha_f)} + \sqrt{n^2 - \cos^2(\alpha_i)} \end{bmatrix} \tag{2.13}$$

2.2.4 *Transmission Factors:* $\mathbf{T}(\alpha_i)$ *and* $\mathbf{T}(\alpha_f)$

As the name implies, the transmission factors account for how much of the incident and scattered X-ray beam are transmitted into or out of the material. They are simply the Fresnel transmission coefficients for the X-ray-material system and are given by:

$$T(\alpha_{i,f}) = \frac{2k_z^{i,f}}{k_z^{i,f} + k_z^{\prime i,f}} \tag{2.14}$$

$$k_z^i = -\sin(\alpha_i) \tag{2.15}$$

$$k_z^f = \sin(\alpha_f) \tag{2.16}$$

$$k_z'^i = -n \sin(\alpha_i') \tag{2.17}$$

$$k_z'^f = n \sin\left(\alpha_f'\right) \tag{2.18}$$

Here, $\alpha_{i,f}'$ is the incident or emergent angle within the medium. α_i' can be expressed in terms of α_i as follows:

$$k_z'^i = -n \sin(\alpha_i') = -\sqrt{n^2 - n^2\cos^2(\alpha_i')} \tag{2.19}$$

For angles measured from the plane of the sample, Snell's law is given by:

$$n_1 \cos(\theta_1) = n_2 \cos(\theta_2) \tag{2.20}$$

For the vacuum-tungsten interface this gives:

$$\cos(\alpha_i) = n \cos(\alpha_i') \tag{2.21}$$

Substituting 2.21 into 2.19:

$$k_z'^i = -\sqrt{n^2 - \cos^2(\alpha_i)} \tag{2.22}$$

Then, substituting 2.15 and 2.22 into 2.14:

$$T(\alpha_i) = \frac{2\sin(\alpha_i)}{\sin(\alpha_i) + \sqrt{n^2 - \cos^2(\alpha_i)}} \tag{2.23}$$

A similar expression can readily be found for $T(\alpha_f)$. These Fresnel transmission coefficients are most significant at low angles. $T(\alpha_f)$ is responsible for strong scattering in the so-called Yoneda peak at an angle $\alpha_f = \sqrt{2\delta}$.

2.2.5 *Form Factor and Volume:* F(q′) *and* V

The form factor, $F(\boldsymbol{q}')$, comes about as a consequence of scattering due to the shape of individual particles, and is strongly influenced by the particle size and shape. The

form factor can be calculated by integrating over the volume of the particle, then dividing by the volume of the particle[3]:

$$F(\boldsymbol{q}) = \frac{\iiint \Delta\rho_e(\boldsymbol{p}(x,y,z))e^{i\boldsymbol{q}\cdot\boldsymbol{p}(x,y,z)}dx\,dy\,dz}{V_{particle}} \tag{2.24}$$

Where $\boldsymbol{p}(x,y,z)$ is any point within the volume of the scattering particle, and $\Delta\rho_e(\boldsymbol{p}(x,y,z))$ is the difference between the electron density of the particle and that of the surrounding matrix at point $\boldsymbol{p}$. As Eq. 2.11 requires the product of the form factor and volume, one could just as well multiply Eq. 2.24 by the volume of the particle to eliminate the denominator. For particles with a constant electron density, the $\Delta\rho_e(\boldsymbol{p}(x,y,z))$ term may also be omitted.

In general, form factors can only be solved analytically if there are special symmetrical relationships which one can take advantage of. By way of example, I will demonstrate the process by solving the form factor of a cube of constant electron density with side length 2R, centred at the origin with its edges running parallel to the x, y, and z-axes:

$$F_{Cube}V_{Cube} = \iiint_{-\infty}^{\infty} e^{i\boldsymbol{q}\cdot\boldsymbol{p}(x,y,z)}dx\,dy\,dz \tag{2.25}$$

$$F_{Cube}V_{Cube} = \int_{-R}^{R} e^{ixq_x}dx \int_{-R}^{R} e^{iyq_y}dy \int_{-R}^{R} e^{izq_z}dz \tag{2.26}$$

Each of the integrals is of the same form, so solving for $\int_{-R}^{R} e^{ixq_x}dx$:

$$F_{x,Cube} = \int_{-R}^{R} e^{ixq_x}dx \tag{2.27}$$

$$F_{x,Cube} = \frac{1}{iq_x}e^{iRq_x} - \frac{1}{iq_x}e^{-iRq_x} \tag{2.28}$$

$$F_{x,Cube} = \frac{2\sin(q_xR)}{q_x} \tag{2.29}$$

[3]Strictly speaking the form factor is defined without reference to the electron density; i.e.

$$F(\boldsymbol{q}) = \frac{\iiint e^{i\boldsymbol{q}\cdot\boldsymbol{p}(x,y,z)}dx\,dy\,dz}{V_{particle}}$$

This is more a matter of convention than physics. In practice, if a particle's electron density is non-uniform, Eq. 2.24 can be substituted for the form factor.

The full form factor is thus:

$$F_{Cube}V_{Cube} = 8\frac{\sin(q_xR)}{q_x}\frac{\sin(q_yR)}{q_y}\frac{\sin(q_zR)}{q_z} \tag{2.30}$$

Alternatively, this could be expressed purely in terms of the form factor by removing the volume of the cube; $V_{Cube} = 8R^3$:

$$F_{Cube} = \frac{\sin(q_xR)}{q_xR}\frac{\sin(q_yR)}{q_yR}\frac{\sin(q_zR)}{q_zR} \tag{2.31}$$

If these cubes were randomly orientated within the material, one could then integrate this expression over all possible orientations of the cube.

For He nano-bubbles in W a spherical model is more appropriate. For perfect spheres, the form factor is given by [23]:

$$F_{Sphere}(\boldsymbol{q}') = 3\frac{\sin(|\boldsymbol{q}'|R) - |\boldsymbol{q}'|R\cos(|\boldsymbol{q}'|R)}{(|\boldsymbol{q}'|R)^3} \tag{2.32}$$

$$|\boldsymbol{q}'| = \sqrt{q_x'^2 + q_y'^2 + q_z'^2} \tag{2.33}$$

$$V_{Sphere} = \frac{4}{3}\pi R^3 \tag{2.34}$$

In practice, it is known that He nano-bubbles are not perfectly spherical [22]. However, even if the nano-bubbles are ellipsoidal a spherical model would provide a very good approximation if these ellipsoids were randomly orientated. W exposed to He plasma should be isotropic in the x–y plane. However, any concentration gradient with depth, and even the presence of the surface itself, introduces anisotropy along the z-direction. To account for this, and any preferred orientation this may lead to, the spherical form factor above can be generalised to that of a spheroid with its axis of rotational symmetry aligned along the z-axis, as shown as Fig. 2.8. For a spheroid with a height/width ratio ϵ, an effective radius R_ϕ can be calculated for any value of $\boldsymbol{q}'$ by:

$$R_\phi = R_{xy}\sqrt{\sin^2(\phi) + \epsilon^2\cos^2(\phi)} \tag{2.35}$$

Where R_{xy} is the radius of the spheroid in the x-y plane, and ϕ is the angle the scattering vector $\boldsymbol{q}'$ makes with the z-axis. Noting that $\sin^2(\phi) = \frac{q_x^2 + q_y^2}{|\boldsymbol{q}'|^2}$ and $\cos^2(\phi) = \frac{q_z^2}{|\boldsymbol{q}'|^2}$, the product $|\boldsymbol{q}'|R_\phi$ can be simplified to:

$$|\boldsymbol{q}'|R_\phi = R_{xy}\sqrt{q_x^2 + q_y^2 + \epsilon^2 q_z^2} \tag{2.36}$$

The form factor for such a spheroid is then:

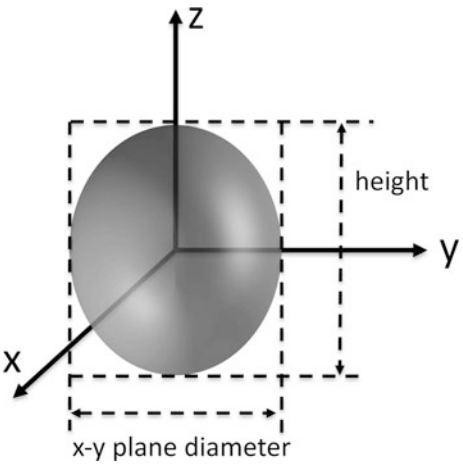

Fig. 2.8 Illustration of spheroids used in the spheroidal model. For these spheroids, μ is the average x–y plane diameter, while ϵ is the ratio of the height to the x-y plane diameter

$$F_{Spheroid}(\boldsymbol{q}') = 3\frac{\sin\left(|\boldsymbol{q}'|R_\phi\right) - |\boldsymbol{q}'|R_\phi\cos\left(|\boldsymbol{q}'|R_\phi\right)}{\left(|\boldsymbol{q}'|R_\phi\right)^3} \tag{2.37}$$

$$V_{Spheroid} = \frac{4}{3}\pi\epsilon R^3 \tag{2.38}$$

For more complex shapes, numerical integration is also an option.

2.2.6 *Structure Factor:* S(q′)

The structure factor, $S(\boldsymbol{q}')$, is used to account for correlations between scattering particle positions within the material. In principle, one could calculate a single form factor for an entire material by integrating over the electron density for every point within the sample. This is obviously impractical. Instead, if one knows how particles are distributed within a material, this all-encompassing scattering factor can be approximated by performing a convolution between the electron density function of an individual particle (let's call it $\Delta\rho_e(\boldsymbol{p})$), and the probability density function of the particles ($P(\boldsymbol{p})$), provided that all particles are identical. The overall scattering factor is then calculated by (see Eq. 2.24):

$$Scattering = \iiint_{-\infty}^{\infty} \Delta\rho_e(\boldsymbol{p}) * P(\boldsymbol{p})e^{i\boldsymbol{q}\cdot\boldsymbol{p}}dx\,dy\,dz \tag{2.39}$$

Note that * represents the convolution operator. The astute reader may notice that this equation is analogous to the Fourier transform equation ($\boldsymbol{q}$ and $\boldsymbol{p}$ used for clarity):

$$\mathcal{F}(\boldsymbol{q}) = \int_{-\infty}^{\infty} f(\boldsymbol{p}) e^{i\boldsymbol{q}.\boldsymbol{p}} d\boldsymbol{p} \tag{2.40}$$

Conveniently, the Fourier transform of a convolution is equal to the product of the Fourier transforms of each individual function, allowing 2.39 to be simplified to:

$$\begin{aligned} Scattering = & \iiint_{-\infty}^{\infty} \Delta\rho_e(\boldsymbol{p}) e^{i\boldsymbol{q}.\boldsymbol{p}} dx\, dy\, dz \\ & \times \iiint_{-\infty}^{\infty} P(\boldsymbol{p}) e^{i\boldsymbol{q}.\boldsymbol{p}} dx\, dy\, dz \end{aligned} \tag{2.41}$$

The first of these integrals is analogous to Eq. 2.24, and is equal to the product of the form factor (adjusted for potentially non-uniform electron density) and the particle volume. The second integral is the structure factor. The important point here is that both the form and structure factors can be determined independently.

Even if a system is disordered, the presence of a high concentration of particles will bring about some short-range ordering as particles cannot occupy the same volume and must be "stacked" within the material somehow. As the concentration of these particles is reduced this effect becomes smaller. For infinitely dilute disordered particles, the structure factor is 1. Where appropriate, this simplifying assumption has been used for the GISAXS modelling discussed in this thesis.

2.2.7 *Attenuation Factor:* $\mathbf{A}(\alpha_i, \alpha_f)$

As nano-bubbles exist beneath the material surface, X-rays must propagate some distance before scattering can occur, and then must travel back out of the material to the surface. During this transit within the material attenuation occurs, reducing the X-ray intensity. Further, the extent to which this occurs depends largely on the incident and scattered X-ray angles. As we are dealing with scattering at small angles, the effect of lateral scattering will be negligible, so attenuation with depth (z-direction) is the primary concern.

For a material of constant composition and density, the attenuation factor will be given by:

$$A(\alpha_i, \alpha_f) = \int_0^{\infty} D(z) e^{-z/z_i} e^{-z/z_f} dz \tag{2.42}$$

There are three separate contributions to the integral. The first, $D(z)$, is the depth distribution function of the particles, while the second and third components correspond to the attenuation experienced by the X-ray as it travels to and from the particle, respectively. z_i and z_f are attenuation coefficients for the incident and

scattered X-rays, and correspond to the distance along the z-direction at which the X-ray is attenuated by a factor of $1/e$. These factors are calculated by [24]:

$$z_{i,f}\left(\alpha_{i,f}\right) = \frac{\lambda\sqrt{2}}{4\pi}\left[\sqrt{\left(\alpha_{i,f}^2 - 2\delta\right)^2 + 4\beta^2} - \alpha_{i,f}^2 + 2\delta\right]^{\frac{-1}{2}} \tag{2.43}$$

If the bubble concentration decreases exponentially with depth, Eq. 2.42 would become:

$$A\left(\alpha_i, \alpha_f\right) = \int_0^\infty e^{-z/z_i} e^{-z/z_f} e^{-z/\tau} dz \tag{2.44}$$

Where τ is the depth at which the bubble concentration is reduced by a factor of $1/\tau$. Equation 2.44 can alternatively be written as:

$$A\left(\alpha_i, \alpha_f\right) = \int_0^\infty e^{-z\left(\frac{1}{z_i}+\frac{1}{z_f}+\frac{1}{\tau}\right)} dz \tag{2.45}$$

Allowing one to define an effective attenuation coefficient, z_{eff}:

$$\frac{1}{z_{eff}} = \frac{1}{z_i} + \frac{1}{z_f} + \frac{1}{\tau} \tag{2.46}$$

Solving Eq. 2.45 then gives:

$$A\left(\alpha_i, \alpha_f\right) = z_{eff} \tag{2.47}$$

2.2.8 Particle Size Distributions

Particles do not necessarily possess the same dimensions, so it is important to be able to account for their finite size distribution. Particle size distributions depend on the mechanisms which drive particle formation and growth, so determining the nature of the distribution is important for nano-bubble modelling.

Two of the most widely used distribution functions used for modelling particle size distributions are the log-normal [25, 26] and Weibull distributions [27, 28]. The normalised log-normal distribution is described by the function:

$$P(x) = \frac{1}{x\sigma\sqrt{2\pi}} e^{-\frac{(\ln x - \ln \mu)^2}{2\sigma^2}} \tag{2.48}$$

In μ and σ are referred to as the *location parameter* and *scale parameter*, respectively. μ is equivalent to the median value, however the scale parameter is

somewhat difficult to visualise (see Fig. 2.9a). Instead, it can be helpful to express the spread of the distribution in terms of the full width at half maximum (FWHM), where:

$$\sigma = \frac{1}{\sqrt{2\ln 2}} \sinh^{-1}\left(\frac{FWHM}{2\mu}\right) \tag{2.49}$$

The normalised Weibull probability density function is given by:

$$P(x) = \frac{k}{\lambda}\left(\frac{x}{\lambda}\right)^{k-1} e^{-(x/\lambda)^k} \tag{2.50}$$

Here, k and λ are the *shape parameter* and the *scale parameter*, respectively. Other statistical properties are summarised in Table 2.1. Given the greater complexity of the Weibull function it can be difficult to visualise a distribution given the shape and scale parameters alone. Instead, where this distribution is used it is better to express the full distribution graphically to aid with interpretation (see Fig. 2.9b).

If particles follow some finite size distribution then the assumption of uniform particle sizes used in the derivation of the structure factor in Sect. 2.2.6 will not hold. The relative simplicity of Eq. 2.11 can be recovered if we assume that in any given volume of the sample the particle sizes are approximately equal, with size variations occurring between locations separated by more than the coherent lengths of the X-ray. This approximation, known as the local monodisperse approximation, allows one to calculate the scattering from different sized particles independently, leading to the overall scattering equation:

$$I \propto |T(\alpha_i)|^2 \left|T\left(\alpha_f\right)\right|^2 \left\langle V^2 |F(\boldsymbol{q}')|^2 \right\rangle |S(\boldsymbol{q}')|^2 A\left(\alpha_i, \alpha_f\right) \tag{2.51}$$

Where $\left\langle V^2 |F(\boldsymbol{q}')|^2 \right\rangle$ is the average volume-weighted form factor contribution to the intensity, given by:

$$\left\langle V^2 |F(\boldsymbol{q}')|^2 \right\rangle = \int_0^\infty P(x) V(x)^2 |F(x, \boldsymbol{q}')|^2 dx \tag{2.52}$$

An alternative approach is the decoupling approximation, which assumes that there are no correlations between the particle sizes and where they are located. This works by introducing diffuse scattering component to account for the disorder of this system, as described by Kotlarchyk and Chen in Ref. [29]. This modifies the intensity function to:

$$I \propto |T(\alpha_i)|^2 \left|T\left(\alpha_f\right)\right|^2 \left(\left\langle V^2 |F(\boldsymbol{q}')|^2 \right\rangle - |\langle V.F(\boldsymbol{q}')\rangle|^2 + |\langle V.F(\boldsymbol{q}')\rangle|^2 |S(\boldsymbol{q}')|^2\right) A\left(\alpha_i, \alpha_f\right) \tag{2.53}$$

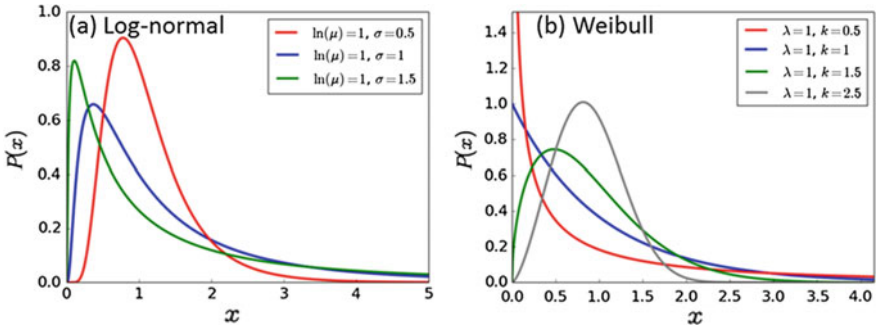

Fig. 2.9 Examples are shown for **a** log-normal and **b** Weibull distribution functions for a range of different parameter values. For the Weibull distribution, $k = 1$ is equivalent to an exponential distribution

Table 2.1 Selection of statistical properties of log-normal and Weibull probability density functions

Property	Log-normal	Weibull
Probability density function	$\frac{1}{x\sigma\sqrt{2\pi}} e^{-\frac{(\ln x - \ln \mu)^2}{2\sigma^2}}$	$\frac{k}{\lambda}\left(\frac{x}{\lambda}\right)^{k-1} e^{-(x/\lambda)^k}$
Mean	$e^{\ln \mu + \sigma^2/2}$	$\lambda.\Gamma\left(1+\frac{1}{k}\right)$
Median	$e^{\ln \mu}$	$\lambda(\ln(2))^{1/k}$
Mode	$e^{\ln \mu - \sigma^2}$	$\begin{cases} \lambda\left(\frac{k-1}{k}\right)^{\frac{1}{k}} & k > 1 \\ 0 & k \leq 1 \end{cases}$
Variance	$\left(e^{\sigma^2} - 1\right) e^{2\ln \mu + \sigma^2}$	$\lambda^2\left[\Gamma\left(1+\frac{2}{k}\right) - \left(\Gamma\left(1+\frac{1}{k}\right)\right)^2\right]$

Where $|\langle V.F(\boldsymbol{q}')\rangle|^2$ is the average volume-weighted form factor:

$$|\langle V.F(\boldsymbol{q}')\rangle|^2 = \left|\int_0^\infty P(x)V(x)F(x,\boldsymbol{q}')dx\right|^2 \tag{2.54}$$

The monodisperse approximation would be better in cases where particle sizes are strongly correlated with their neighbours, while the decoupling approximation is best where no correlations exist at all. For nano-bubbles in tungsten, neither of these conditions is truly satisfied: nano-bubbles have a tendency to be larger the closer they are to the surface of the material, but at any given depth there is still a broad distribution of bubble sizes (see Sect. 3.2.2).

For $S(\boldsymbol{q}') = 1$, both approximations are identical.

2.3 Pattern Fitting

2.3.1 Data Sampling Methods

The very first step in the fitting process is to decide what parts of the X-ray scattering pattern to fit. Structures with different sizes and shapes will contribute more scattering to different regions of reciprocal space, so it is important that the fitting region is broad enough to cover all structures of interest. Another important consideration is the presence of scattering features which are not described within the model. For instance, in most patterns described in this thesis there is strong scattering along the q_z axis which is likely a consequence of scattering from surface roughness—an effect which has not been incorporated into the model. Further unaccounted scattering is also present at higher q values, which may come from fluorescence from the synchrotron beamline's collimating slits. These regions should be avoided.

The two fitting strategies used in this thesis are 2D area fits, and 1D line fits (Fig. 2.10). For the 2D fits, an area selected which encompasses a wide range of reciprocal space across a range of q_y and q_z values. Low values of q_y are excluded to avoid the bright scattering along the q_z axis. This approach results in a very large number of data points falling within the region of interest, so the data must then be downsampled by uniformly selecting a more manageable number of points from within the region of interest.

1D fits are more common amongst GISAXS users. Here, slices of data are selected lying parallel to either the q_y or q_z axes. The advantage of this approach is that many scattering patterns encountered show distinctly different behaviours along each of these directions. For instance, scattering from multi-layered films stacked on top of each other in the z-direction will result in oscillations along the q_z direction. This approach could also be made more computationally efficient, however the modelling algorithm used in this work has not been optimised for this approach. This is something which should be improved during the software's future development. In this work, several slices along both the q_y and q_z axes are taken and fitted simultaneously. All quantitative fitting was performed with this 1D approach.

Finally, one should decide whether to fit patterns taken from different X-ray incident angles independently or simultaneously. Simultaneous fits have the advantage that differences in intensity between measurements taken at different angles result in part from the depth distribution of the particles, allowing parameters for the depth distribution to also be fitted. Generally, the approach in this thesis is to perform simultaneous fits.

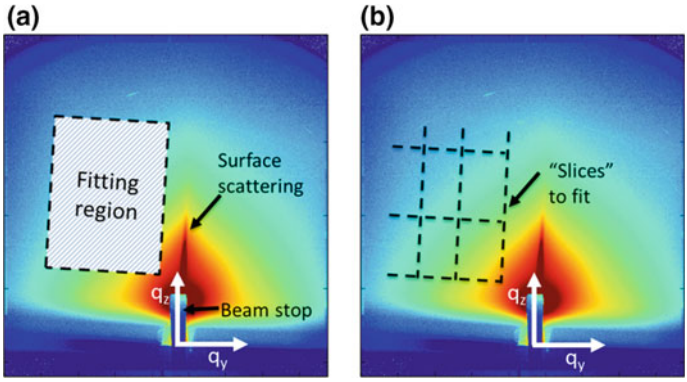

Fig. 2.10 The difference between **a** 2D and **b** 1D fitting strategies is shown. Note that there are a number of contributions in the pattern which do not come from the nano-bubbles themselves and should therefore be avoided in the fitting process. Toward the centre of the pattern lies a strong central peak resulting from surface scattering. A beam stop is also visible, and was used to prevent damaging the detector with the very high intensities of the direct and reflected X-ray beams. These particular patterns are also slightly rotated due to a misalignment of the sample. This can be corrected for during fitting

2.3.2 *Optimisation and Goodness-of-Fit*

Fitting was performed by minimising the χ^2 value of the fit using the Nelder-Mead method for parameter optimisation [30, 31] using the algorithm contained within the "scipy" Python package. For data where errors have a Gaussian distribution the parameter values which produce minimum χ^2 value coincides with the maximum of the likelihood function for a given model [32]. This is generally not true for non-Gaussian noise. Strictly speaking, systems where errors result from counting statistics follow a Student's t-distribution, however, for a sufficiently large number of counts a Gaussian distribution is an excellent approximation. The difference between Gaussian distributions and Student t-distributions is negligible for the relatively large number of counts (>100 per pixel) for the CCD data typically obtained during the work described in this thesis.

The χ^2 value for a given iteration of the fit is given by:

$$\chi^2 = \sum_{n=1}^{N} \left(\frac{y_n - f\left(x_n; \vec{\theta}\right)}{\sigma_n} \right)^2 \tag{2.55}$$

Where N is the total number of data values y_n at position x_n being fitted, $f\left(x_n; \vec{\theta}\right)$ the model to be fitted, $\vec{\theta}$ the fitting parameters for the iteration, and σ_n the errors at position x_n. For counting noise, the errors are equal to the square root of the number of counts, allowing Eq. 2.55 to be re-written as:

$$\chi^2 = \sum_{n=1}^{N} \frac{\left(y_n - f\left(x_n; \vec{\theta}\right)\right)^2}{y_n} \tag{2.56}$$

While comparisons of χ^2 scores can be used to determine the relative quality of fits for parameter optimisation of a given model, they cannot be used directly for comparisons between different models. Defining some objective metric by which different fits can be compared would be very useful. One common approach to solve this problem is to use the *reduced* χ^2, which is the χ^2 score divided by the number of degrees of freedom of the fit. However, in non-linear models such as the scattering model described here estimating the number of degrees of freedom is prohibitively difficult. Thus, this approach is not applicable here (see [32] for a more detailed discussion of this problem).

An alternative method of determining the relative quality of two different models is to calculate the *normalised residual* of each point being fitted and constructing a histogram by dividing the x-axis into a series of bins and counting how many times the normalised residual falls into each bin (see [33] for an example of this approach). The normalised residual is calculated by:

$$Norm\,Residual = \frac{y_n - f\left(x_n; \vec{\theta}\right)}{\sigma_n} \tag{2.57}$$

For an "ideal" fit, the histogram will follow a Gaussian distribution with a mean value of 0 and a variance of 1. The normalised residual will not be uniformly 0 for an ideal fit as the data contains statistical noise which cannot be fitted. A variance greater than 1 indicates that the model does not completely describe the data, while a variance less than 1 indicates overfitting. This approach also allows the goodness-of-fit to be quantified in terms of a p-score using a Kolmogorov-Smirnov test [34, 35]. In this thesis this residual histogram approach to expressing the goodness-of-fit has been used for qualitative model comparisons, so this additional quantification step has not been performed.

2.3.3 Error Estimation

Error estimation is not trivial. In the literature errors are frequently quoted as a single numerical value which represents one standard deviation in the scatter of the measurements. This approach is valid where errors in the fitting parameters follow a Gaussian distribution, however this is not generally the case. The GISAXS model described in this chapter contains many parameters which must be simultaneously fitted. The simple fact that more than one parameter is being fitted means that the simple 1D Gaussian distribution which is typically assumed when quoting errors is not valid. In principle one could map out the χ^2 values across a wide region of the

n-dimensional parameter space to determine the relative likelihood of a range of fitting parameter combinations, but communicating this sort of information is very difficult—and rarely done in practice.

A common approach to error estimation is to compute the variance-covariance matrix for the values of the fitting parameters after convergence [36]. The variance-covariance matrix is equal to the inverse of the Hessian matrix of the χ^2. The elements of the Hessian matrix are given by [37]:

$$H_{ij} = \frac{\partial^2 \chi^2\left(\vec{\theta}\right)}{\partial\theta_i \partial\theta_j} \tag{2.58}$$

where $\vec{\theta}$ are the optimal parameters determined by minimising χ^2 in the fitting procedure, $\chi^2\left(\vec{\theta}\right)$ is χ^2 (Eq. 2.56) calculated where the model has parameters $\vec{\theta}$, and θ_i and θ_j are the *i*th and *j*th parameters of $\vec{\theta}$. The variance-covariance matrix, V, is then:

$$V = H^{-1} \tag{2.59}$$

The variances of each parameter θ_i are given by the matrix element V_{ii}. Similarly, the covariance of θ_i and θ_j are given by V_{ij}. The standard error, σ, is given by the square root of the variance. In cases where the reduced χ^2 value is significantly greater than 1, this may underestimate the standard error. For linear models the reduced χ^2 value, χ^2_{red}, is given by:

$$\chi^2_{red} = \frac{\chi^2}{n-p} \tag{2.60}$$

Where n is the number of data points, and p is the number of fitting parameters, and $n-p$ is the number of degrees of freedom for the fit. The standard error can then be corrected by multiplying the standard error by $\sqrt{\chi^2_{red}}$ [36]. χ^2_{red} cannot be computed for non-linear models as the number of degrees of freedom is not well defined in those cases [32].

The variance-covariance matrix can be converted into a correlation matrix to better help visualise interdependencies between the different fitting parameters. This is done by constructing a diagonal matrix, D, from V as follows:

$$D_{ij} = \begin{cases} \sqrt{V_{ii}} & i = j \\ 0 & i \neq j \end{cases} \tag{2.61}$$

then performing the matrix operations:

$$C = D^{-1}.V.D^{-1} \tag{2.62}$$

Here, C is the correlation matrix. Values within the matrix vary between −1 and 1, with negative values implying a negative correlation (i.e. one parameter decreases as the other increases), and positive values indicating a positive correlation (i.e. both parameters increase or decrease together).

The drawback of a statistical approach such as this is that it relies on many assumptions, such as the linearity of the model. The GISAXS model described in this chapter is non-linear and therefore precludes the use of any approach that requires an estimation of χ^2_{red}. The "bootstrap" method is an alternative approach that is applicable to models of any complexity, and is widely used in fields such as astronomy [32], the social sciences, and medicine [38].

For the bootstrap method, optimal parameter values are calculated by fitting a model repeatedly to a synthetic dataset generated by randomly selecting points from the experimental data with replacement. The standard error is then given by the standard deviation of the optimised parameter values. This approach naturally captures many sources of error that can be otherwise difficult to pin-down, including the sensitivity of the fit to changes in individual parameters, correlations between parameters, and random errors that come about due to the intrinsic randomness of the data itself. For more detail on this method, the interested reader is referred to the review by Efron and Tibshirani [38].

For the work in this thesis, error estimates were generated by dividing larger data sets into n equally sized smaller data sets by assigning one nth of the total data points to each set. Each set was then fit individually and the spread of the results used to calculate the standard deviations of the parameters used in the fitting process. The variance-covariance matrix approach was also used as a sanity check for the method. For uncorrelated parameters the agreement between the two approaches was very good. However, the variance-covariance matrix approach tended to significantly underestimate errors for highly correlated parameters.[4]

2.3.4 Other GISAXS Software

In this work, the GISAXS model and fitting algorithm was composed by the author in the Python programming language. Before developing this model the software packages IsGISAXS [39], FitGISAXS [40], and BornAgain [41] were trialled. The IsGISAXS and FitGISAXS software were not well-suited to this project as, to the

[4]It is worth noting that systematic errors can be significant if the GISAXS model chosen does not precisely match the material system under investigation. These errors can be difficult to quantify and will not be captured by a covariance matrix approach. Empirical error estimates (e.g. comparing variability in measurements between measurements taken via different techniques) provide a more robust means of estimating uncertainties, but are not always practical.

best of the author's knowledge, they did not support important features required in this work such as arbitrary particle size distribution functions or the ability to fit measurements taken at different angles simultaneously. BornAgain is a Python package which offers great flexibility, however, at the time most of the data fitting was performed the documentation for the software was very limited. The situation has improved immensely in the past few years—BornAgain now has extensive documentation online covering most aspects of the software, including detailed tutorials and sample code for pattern simulation and fitting.

The author would recommend readers interested in performing their own GISAXS data fitting use the BornAgain package, as it offers the most extensive documentation and greatest flexibility.

2.4 Concluding Remarks

2.4.1 Future Work

The GISAXS model outlined in this chapter and the underpinning software is still under development, and many new features will be implemented in the future. One of the simpler adjustments would be to incorporate more form factors and structure factors into the model. Form factors for many commonly encountered shapes are readily available in the literature. An extensive list with full mathematical descriptions can be found in the documentation of the IsGISAXS software [39], allowing straightforward transplantation into the software used in this thesis. Incorporating structure factors into the model is also straightforward. However, structure factors are more difficult to verify via TEM than particle sizes and shapes as, especially if particles are only weakly ordered. This is because many particle positions would need to be precisely identified in three dimensions, while a TEM micrograph is only a two dimensional image.

Another potential improvement would be to model effects from surface roughness. Surface roughness can affect scattering in a number of ways. First and foremost, the variability of the surface height itself will produce scattering. But there is another more subtle effect: an uneven surface means that not all X-rays will be incident at the same angle. This could have a significant effect on efforts at modelling nano-bubble depth distributions. Stoev and Sakarai [42] note that surface roughness decreases reflection from the material surface, and can influence X-ray transmission through material interfaces. This will be most pronounced for low incident angles and at low q_z, where the transmission factor is most significant.

The presence of particles such as nano-bubbles beneath the W surface will effectively reduce the density of the near-surface region of the material, reducing the refractive index in this area. If the concentration of these particles is high enough, it could affect the refractive index of these materials enough to have a measurable effect on scattering. If bubble densities vary with a function of depth,

the refractive index may change continuously between the surface and the bulk. Corrections for this effect are available in Lazzari et al. [43].

Each of these additional factors will increase the computational complexity of the model, thereby increasing the time required for analysis. An important priority in future will be to improve the efficiency of the model such that it can be made as fast as possible. If single fits take several hours it makes it difficult to test different model systems. This increases the time and effort required for analysis, making it more difficult to analyse large data sets.[5]

2.4.2 Summary

GISAXS is a powerful non-destructive technique which has the potential to provide the fusion materials research community with an unprecedented level of precision for measurements of nano-structure ordering, and size and depth distributions. The technique is highly complementary to TEM as it provides information about entire nano-structure populations, rather than individual structures as is the case for TEM.

In this chapter the GISAXS model developed by the author and used throughout this thesis was described in sufficient detail that anyone with a reasonable level of programming knowledge should be able to reproduce it. The underlying physics behind this model was also outlined, along with a brief overview of data fitting and the mathematical considerations one should be mindful of when comparing different physical models of the same system.

References

1. S. Kajita, N. Yoshida, R. Yoshihara, N. Ohno, M. Yamagiwa, TEM observation of the growth process of helium nanobubbles on tungsten: nanostructure formation mechanism. J. Nucl. Mater. **418**, 152–158 (2011). https://doi.org/10.1016/j.jnucmat.2011.06.026
2. M. Miyamoto, D. Nishijima, M.J.J. Baldwin, R.P.P. Doerner, Y. Ueda, K. Yasunaga, N. Yoshida, K. Ono, Microscopic damage of tungsten exposed to deuterium-helium mixture plasma in PISCES and its impacts on retention property. J. Nucl. Mater. **415**, S657–S660 (2011). https://doi.org/10.1016/j.jnucmat.2011.01.008
3. D.B. Williams, C.B. Carter, *Transmission Electron Microscopy: A Textbook for Materials Science* (Springer, Berlin, Germany, 2009)

[5]Since the original submission of this thesis the author has developed a Monte-Carlo extension of the GISAXS fitting code which allows size and shape distributions to be calculated without making a priori assumptions about the distribution functions these properties should follow. A more detailed discussion of this approach, and the sort of information that can be derived from it, are available in Ref. [44].

4. N. Ohno, Y. Hirahata, M. Yamagiwa, S. Kajita, M. Takagi, N. Yoshida, R. Yoshihara, T. Tokunaga, M. Tokitani, Influence of crystal orientation on damages of tungsten exposed to helium plasma. J. Nucl. Mater. **438**, S879–S882 (2013). https://doi.org/10.1016/j.jnucmat.2013.01.190
5. M. Miyamoto, S. Mikami, H. Nagashima, N. Iijima, D. Nishijima, R.P. Doerner, N. Yoshida, H. Watanabe, Y. Ueda, A. Sagara, Systematic investigation of the formation behavior of helium bubbles in tungsten. J. Nucl. Mater. **463**, 333–336 (2015). https://doi.org/10.1016/j.jnucmat.2014.10.098
6. R. Langridge, D.A. Marvin, W.E. Seeds, H.R. Wilson, C.W. Hooper, M.H.F. Wilkins, L.D. Hamilton, The molecular configuration of deoxyribonucleic acid. J. Mol. Biol. **2**, 38–IN12 (1960). https://doi.org/10.1016/s0022-2836(60)80005-8
7. P. Müller-Buschbaum, Grazing incidence small-angle X-ray scattering: an advanced scattering technique for the investigation of nanostructured polymer films. Anal. Bioanal. Chem. **376**, 3–10 (2003)
8. P. Busch, D. Posselt, D.-M. Smilgies, M. Rauscher, C.M. Papadakis, Inner structure of thin films of lamellar poly(styrene-b-butadiene) diblock copolymers as revealed by grazing-incidence small-angle scattering. Macromolecules **40**, 630–640 (2007). https://doi.org/10.1021/ma061695c
9. S.V. Roth, G. Santoro, J.F.H. Risch, S. Yu, M. Schwartzkopf, T. Boese, R. Döhrmann, P. Zhang, B. Besner, P. Bremer, D. Rukser, M.A. Rübhausen, N.J. Terrill, P.A. Staniec, Y. Yao, E. Metwalli, P. Müller-Buschbaum, Patterned diblock co-polymer thin films as templates for advanced anisotropic metal nanostructures. ACS Appl. Mater. Interfaces **7**, 12470–12477 (2015). https://doi.org/10.1021/am507727f
10. S.V. Roth, T. Autenrieth, G. Grübel, C. Riekel, M. Burghammer, R. Hengstler, L. Schulz, P. Müller-Buschbaum, In situ observation of nanoparticle ordering at the air-water-substrate boundary in colloidal solutions using X-ray nanobeams. Appl. Phys. Lett. **91**, 91915 (2007). https://doi.org/10.1063/1.2776850
11. M. Schwartzkopf, G. Santoro, C.J. Brett, A. Rothkirch, O. Polonskyi, A. Hinz, E. Metwalli, Y. Yao, T. Strunskus, F. Faupel, P. Müller-Buschbaum, S.V. Roth, Real-time monitoring of morphology and optical properties during sputter deposition for tailoring metal-polymer interfaces. ACS Appl. Mater. Interfaces **7**, 13547–13556 (2015). https://doi.org/10.1021/acsami.5b02901
12. G. Renaud, R. Lazzari, C. Revenant, A. Barbier, M. Noblet, O. Ulrich, F. Leroy, J. Jupille, Y. Borensztein, C.R. Henry, J.-P. Deville, F. Scheurer, J. Mane-Mane, O. Fruchart, Real-time monitoring of growing nanoparticles. Science **300**, 1416–1419 (2003). https://doi.org/10.1126/science.1082146
13. G.H. Vineyard, Grazing-incidence diffraction and the distorted-wave approximation for the study of surfaces. Phys. Rev. B. **26**, 4146–4159 (1982). https://doi.org/10.1103/PhysRevB.26.4146
14. D. Attwood, *Soft X-rays and Extreme Ultraviolet Radiation* (Cambridge University Press, Cambridge, 1999)
15. F. van der Veen, F. Pfeiffer, Coherent X-ray scattering. J. Phys. Condens. Matter **16**, 5003–5030 (2004). https://doi.org/10.1088/0953-8984/16/28/020
16. A. Thompson, D. Attwood, E. Gullikson, M. Howells, K.-J. Kim, J. Kirz, J. Kortright, I. Lindau, Y. Liu, P. Pianetta, A. Robinson, J. Scotfield, J. Underwood, G. Williams, H. Winick, *X-ray Data Booklet*, 3rd edn. (Lawrence Berkeley National Laboratory, Berkeley, 2009). http://xdb.lbl.gov/xdb-new.pdf
17. M. Willner, M. Bech, J. Herzen, I. Zanette, D. Hahn, J. Kenntner, J. Mohr, A. Rack, T. Weitkamp, F. Pfeiffer, Quantitative X-ray phase-contrast computed tomography at 82 keV. Opt. Express **21**, 4155–4166 (2013). https://doi.org/10.1364/OE.21.004155
18. National Institute of Standards and Technology, X-ray form factor, attenuation and scattering tables (2001), http://physics.nist.gov/PhysRefData/FFast/html/form.html
19. Lawrence Berkeley National Laboratory, X-ray Properties of the Elements (2005), http://henke.lbl.gov/optical_constants/pert_form.html

20. M. Ruiz-Yaniz, I. Zanette, A. Rack, T. Weitkamp, P. Meyer, J. Mohr, F. Pfeiffer, X-ray-refractive-index measurements at photon energies above 100 keV with a grating interferometer. Phys. Rev. A **91**, 33803 (2015). https://doi.org/10.1103/PhysRevA.91.033803
21. D. Babonneau, S. Peripolli, M.-F. Beaufort, J.-F. Barbot, J.-P. Simon, GISAXS study of cavities and 113 defects induced by neon and helium implantation in silicon. J. Appl. Crystallogr. **40**, s350–s354 (2007). https://doi.org/10.1107/S0021889806043755
22. M. Thompson, R. Sakamoto, E. Bernard, N. Kirby, P. Kluth, D. Riley, C. Corr, GISAXS modelling of helium-induced nano-bubble formation in tungsten and comparison with TEM. J. Nucl. Mater. **473**, 6–12 (2016). https://doi.org/10.1016/j.jnucmat.2016.01.038
23. J.S. Pedersen, Analysis of small-angle scattering data from colloids and polymer solutions: modeling and least-squares fitting. Adv. Colloid Interface Sci. **70**, 171–210 (1997). https://doi.org/10.1016/S0001-8686(97)00312-6
24. L.G. Parratt, Surface studies of solids by total reflection of X-rays. Phys. Rev. **95**, 359–369 (1954). https://doi.org/10.1103/PhysRev.95.359
25. D. Park, S. Kim, M. An, J. Hwang, Real-time measurement of submicron aerosol particles having a log-normal size distribution by simultaneously using unipolar diffusion charger and unipolar field charger. J. Aerosol Sci. **38**, 1240–1245 (2007). https://doi.org/10.1016/j.jaerosci.2007.09.002
26. K. Juraić, D. Gracin, B. Šantić, D. Meljanac, N. Zorić, A. Gajović, P. Dubček, S. Bernstorff, M. Čeh, GISAXS and GIWAXS analysis of amorphous–nanocrystalline silicon thin films. Nucl. Instrum. Methods Phys. Res. Sect. B Beam Interact. Mater. Atoms. **268**, 259–262 (2010). https://doi.org/10.1016/j.nimb.2009.09.046
27. Z. Fang, B.R. Patterson, M.E. Turner, Modeling particle size distributions by the Weibull distribution function. Mater. Charact. **31**, 177–182 (1993). https://doi.org/10.1016/1044-5803(93)90058-4
28. Y.S. Cheong, G.K. Reynolds, A.D. Salman, M.J. Hounslow, Modelling fragment size distribution using two-parameter Weibull equation. Int. J. Miner. Process. **74**, S227–S237 (2004). https://doi.org/10.1016/j.minpro.2004.07.012
29. M. Kotlarchyk, S.-H. Chen, J.S. Huang, M.W. Kim, Structure of three-component microemulsions in the critical region determined by small-angle neutron scattering. Phys. Rev. A **29**, 2054–2069 (1984). http://link.aps.org/doi/10.1103/PhysRevA.29.2054
30. J.A. Nelder, R. Mead, A simplex method for function minimization. Comput. J. **7**, 308–313 (1965). https://doi.org/10.1093/comjnl/7.4.308
31. F. Gao, L. Han, Implementing the Nelder-Mead simplex algorithm with adaptive parameters. Comput. Optim. Appl. **51**, 259–277 (2012). https://doi.org/10.1007/s10589-010-9329-3
32. R. Andre, T. Schulze-Hartung, P. Melchior, R. Andrae, T. Schulze-Hartung, P. Melchior, Dos and don'ts of reduced chi-squared (2010). http://arxiv.org/abs/1012.3754. Accessed 20 Jan 2017
33. J. Ma, H. Zhao, P. Schuck, A histogram approach to the quality of fit in sedimentation velocity analyses. Anal. Biochem. **483**, 1–3 (2015). https://doi.org/10.1016/j.ab.2015.04.029
34. A.N. Kolmogorov, *Foundations of Probability*, (Berlin, 1933). citeulike-article-id:1055464
35. N. Smirnov, Table for estimating the goodness of fit of empirical distributions. Ann. Math. Stat. **19**, 279–281 (1948), http://www.jstor.org/stable/2236278
36. B.H. Toby, S.J.L. Billinge, Determination of standard uncertainties in fits to pair distribution functions. Acta Crystallogr. Sect. A **60**, 315–317 (2004). https://doi.org/10.1107/S0108767304011754
37. J. Pumplin, D.R. Stump, W.K. Tung, Multivariate fitting and the error matrix in global analysis of data. Phys. Rev. D **65**, 14011 (2001). https://doi.org/10.1103/PhysRevD.65.014011
38. B. Efron, R. Tibshirani, The bootstrap method for assessing statistical accuracy. Behaviormetrika **12**, 1–35 (1985). https://doi.org/10.2333/bhmk.12.17_1
39. R. Lazzari, IsGISAXS: a program for grazing-incidence small-angle X-ray scattering analysis of supported islands. J. Appl. Crystallogr. **35**, 406–421 (2002). https://doi.org/10.1107/S0021889802006088

40. D. Babonneau, FitGISAXS: software package for modelling and analysis of GISAXS data using IGOR Pro. J. Appl. Crystallogr. **43**, 929–936 (2010). https://doi.org/10.1107/S0021889810020352
41. J. Burle, C. Durniak, J.M. Fisher, M. Ganeva, G. Pospelov, W. Van Herck, J. Wuttke, BornAgain—Software for simulating and fitting X-ray and neutron small-angle scattering at grazing incidence (2016), http://www.bornagainproject.org
42. K. Stoev, K. Sakurai, Recent theoretical models in grazing incidence X-ray reflectometry. Rigaku J. **14**, 22–37 (1997)
43. R. Lazzari, F. Leroy, G. Renaud, Grazing-incidence small-angle X-ray scattering from dense packing of islands on surfaces: development of distorted wave Born approximation and correlation between particle sizes and spacing. Phys. Rev. B **76**, 125411 (2007). http://link.aps.org/doi/10.1103/PhysRevB.76.125411
44. M. Thompson, D. Drummond, J. Sullivan, R. Elliman, P. Kluth, N. Kirby, D. Riley, C.S. Corr, Effect of W self-implantation and He plasma exposure on early-stage defect and bubble formation in tungsten. Nucl. Fusion **58**, 66010 (2018). https://doi.org/10.1088/1741-4326/aab96c

Chapter 3
Validation of GISAXS Model with TEM Data

3.1 Experimental Overview

Validation of GISAXS through comparisons with more widely used techniques such as TEM is important for many reasons. First and foremost, it serves as a test of the model and the assumptions which underpin it. Another aspect is that it helps build the profile of the technique within the wider fusion-materials community, by providing a clear demonstration of what it can do, and how it compares to already established techniques.

In this section, a study is described where both GISAXS and TEM were performed on the same sample to measure He-induced nano-bubble diameter distributions in W, demonstrating close agreement between the two techniques. For TEM, nano-bubbles must be counted manually,[1] so the number used to calculate the distribution is limited by instrument availability and the man-hours one is willing to commit to the task. The process of creating the samples, and the statistical analysis used for the TEM aspect of the study are described, followed by the GISAXS measurement conditions and some of the specific details of the model which was fitted for this sample. For comparison, a number of different nano-bubble size distribution models were tested.

This study highlights the strength of GISAXS in being able to quickly determine the properties of the full size distribution of particles, taking advantage of the fact that millions of structures are being probed simultaneously. TEM, on the other hand, excels as a tool to identify the properties of individual particles. In the author's opinion, the two techniques form an excellent complement, and both should have a place in the repertoire of scientists interested in studying these structures.

[1]Automated image recognition has come a long way in recent years, and could be a viable alternative to manual measurement of features imaged via TEM for some applications.

M. Thompson, *Helium Nano-bubble Formation in Tungsten*, Springer Theses,
https://doi.org/10.1007/978-3-319-96011-1_3

3.2 Experimental Procedure

3.2.1 Sample Preparation and Plasma Exposure

Specimens were made from a sheet of powder metallurgical pure W (>99.95%) with a thickness of 0.1 mm. Specimens were cut by press die into 3 mm diameter disks, before being electrically polished in a 10% NaOH solution. Specimens were then heat treated under vacuum at ~2300 K (above the recrystallization temperature) for 15 min in order to enlarge the grain size and remove stresses and defects, thereby optimising the surface conditions for TEM.

Helium plasma exposure was performed in the Large Helical Device (LHD) located in Gifu, Japan. The specimens were set on a high temperature sample holder and heated to 1073 K, then inserted into the LHD vacuum vessel at the first wall position in which the main incident particles are charge exchange particles. The samples were exposed to 130 LHD discharges with He gas puffing. A typical discharge duration was six seconds, repeating every three minutes. The total plasma exposure time was therefore approximately 780 s. Since LHD is mainly operated with hydrogen gas for other experiments, there is hydrogen degassing from the plasma facing components during the helium discharges. The helium plasma of LHD, therefore, includes about 10% hydrogen. The helium implantation and vacancy production profiles into tungsten are estimated by combination of the 3-D neutral Transport code EIRENE and TRIM calculations [1]. Incident fluence is estimated at 10^{23} He/m^2 with a flux of 10^{20} He/m^2/s and a broad ion energy distribution. It is estimated that ion energies as high as 2 keV were present, although low energy particles below 500 eV, which cannot induce displacement damage in tungsten, were dominant.

After the helium plasma exposure experiments, cross-sectional thin samples (about 40 nm in thickness) were fabricated by using focused ion beam (FIB) processing for TEM measurements.

3.2.2 TEM Counting and Statistical Calculations for Exponentially Distributed Data

Diameter and depth distributions of He nano-bubbles in tungsten were determined with TEM by carefully counting and measuring the diameter and depth of each bubble across several cross-sectional TEM micrographs. No attempt was made to account for differences that may occur along grain boundary regions or within crystalline grains of different orientations. Thus, one cannot say if the bubbles in this work are representative of the entire sample. Automated software image analysis was precluded by the uneven contrast throughout the image. A typical

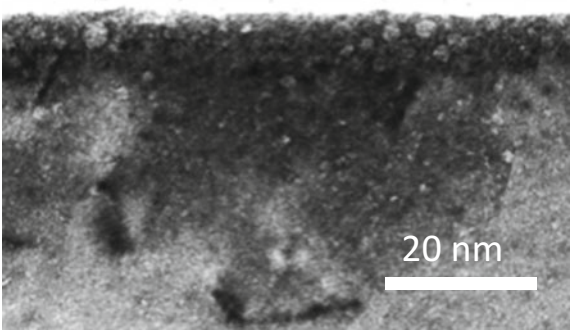

Fig. 3.1 Cross sectional TEM micrograph of helium nano-bubble formation in tungsten exposed to helium plasma in LHD [7]. Here, it is clear that bubbles are both larger and more densely packed closer to the surface than they are deeper in the bulk. Bubbles were counted by slightly defocussing the image (not shown), enhancing the contrast between the bubbles and surrounding material

example of the bubble structures which formed is shown in Fig. 3.1. Here, bubbles appear to be both larger and more closely packed near the surface than they are deeper in the material. During counting, the TEM was defocussed slightly to enhance the contrast between the bubbles and the surrounding matrix. In all, 420 bubbles were manually counted and measured.

Bubble diameters were found to follow an approximately exponential distribution, which was modelled using the equation:

$$P(d) = \frac{1}{\mu} e^{\frac{-d}{\mu}} \tag{3.1}$$

where $P(d)$ is the probability density of a bubble of diameter d, and μ is the mean diameter. Note that μ is the only value which needs to be computed in order to reproduce the entire size distribution. Bubbles smaller than 0.5 nm could not be reliably measured due to the resolution limits of the TEM, so μ was calculated by taking the average of all bubbles with diameters >0.5 nm (there were 300 bubbles in this reduced set). Of course, by eliminating the smaller bubbles one is not calculating the mean of the entire distribution, but instead:

$$\mu' = \int_a^\infty \frac{d}{\mu} e^{\frac{-(d-a)}{\mu}} dd \tag{3.2}$$

where $a = 0.5$. Substituting d for $u = d - a$:

$$\mu' = \int_0^\infty \frac{(u+a)}{\mu} e^{\frac{-u}{\mu}} du \tag{3.3}$$

$$\mu' = \int_0^\infty \frac{u}{\mu} e^{\frac{-u}{\mu}} du + \int_0^\infty \frac{a}{\mu} e^{\frac{-u}{\mu}} du \tag{3.4}$$

$$\mu' = \mu + a \tag{3.5}$$

The mean of the entire distribution is therefore $\mu = \mu' - 0.5$. From the TEM bubble diameter data, μ was found to be 0.68 nm. If the bubbles which were counted were a perfectly random sample of all bubbles within the material we can estimate the standard error (*SE*) of this figure via the equation:

$$SE = \frac{\mu}{\sqrt{N}} \tag{3.6}$$

Here N is the number of bubbles sampled. This gives us an error estimate of $\mu = 0.68 \pm 0.04$ nm.

The depth distribution of the bubbles was calculated via a similar process, using the probability density function:

$$P(z) = \frac{1}{\tau} e^{\frac{-z}{\tau}} \tag{3.7}$$

where z is the depth, and τ the mean volume-weighted bubble depth. The bubble volume, rather than number, was used as this was a much better match for the TEM data. After adding a weight to each point proportional to volume, τ was calculated to have a value of 8.4 ± 0.5 nm. Nano-bubbles closer than 5 nm from the surface were excluded from analysis, reducing the sample size to 336 bubbles. For these shallow depths, helium can be directly implanted into the sample, so bubble growth rates are expected to differ significantly from deeper within the sample where helium is supplied solely via diffusion from above. This difference is readily apparent in Fig. 3.1, as a distinct layer of closely-packed bubbles can be seen just beneath the surface.

3.2.3 *Fitting More Complex Diameter Distributions*

In addition to the exponential distribution, the log-normal (Eq. 2.48) and Weibull (Eq. 2.50) probability density distributions have also been trialled in this work. The log-normal distribution was selected as it is commonly encountered in studies of void formation (e.g. [2]), while the Weibull distribution was selected as it is a two parameter distribution which is equivalent to the exponential distribution when its shape parameter $k = 1$. In effect the Weibull distribution can be seen as a generalisation of the simpler exponential distribution.

Ideally, one should use the statistical properties of the distribution functions to determine the function coefficients from the raw data directly. However, this is not

always possible. In the present case the diameter distribution data is truncated at the value of 0.5 nm, so converting the mean or standard deviation into a probability density function coefficient is not straightforward. Instead, distribution functions have been fitted to a histogram of the TEM bubble data.

To eliminate the need to fit a scaling parameter for these distributions the distribution functions were normalised to the total number of bubbles counted with diameters greater than 0.5 nm. For a dataset where N bubbles have been counted, the scaling factor S required to give this number over the interval $[a, \infty)$ is given by:

$$S = \frac{N}{1 - CDF(a)} \tag{3.8}$$

where CDF is the cumulative distribution function of the probability density function. For the log-normal distribution, the cumulative distribution function is:

$$CDF(x) = \frac{1}{2} + \frac{1}{2}\text{erf}\left(\frac{\ln(x) - \ln(\mu)}{\sqrt{2}\sigma}\right) \tag{3.9}$$

where erf is the error function. Coefficients are defined in Sect. 2.2.8. For the Weibull distribution the cumulative distribution function is:

$$CDF(x) = 1 - e^{-\frac{x^k}{\lambda}} \tag{3.10}$$

Again, coefficients are defined with the original probability density functions in Sect. 2.2.8. To avoid zero values in the nano-bubble diameter histogram the cumulative distribution functions were fitted directly using a χ^2 fitting algorithm. This also led to a much more stable fit for the Weibull distribution relative to approaches based on fitting the probability density function, likely due to the relative simplicity of the cumulative distribution function.

To estimate errors in the fitted coefficents the jackknife method was used [3]. In this approach, the fit is repeated by excluding a single data point each time. The variance of the parameters being fitted is then calculated by:

$$var = \frac{N-1}{N}\sum_{i=1}^{N}(x_i - \overline{x})^2 \tag{3.11}$$

Here x_i are the fitted parameter values of the each of the fitting runs where a data point has been excluded, and $\overline{x}$ is the value for a fit where all data points have been included. Errors are quoted as a single standard deviation, which is of course the square root of the variance.

The calculated parameter values are $\mu = 2.48 \pm 0.14$ nm and $\sigma = 0.9 \pm 0.2$ for the log-normal distribution, and $k = 0.8 \pm 0.1$ and $\lambda = 0.44 \pm 0.14$ nm for the Weibull distribution. For comparison, the median of the exponential distribution in

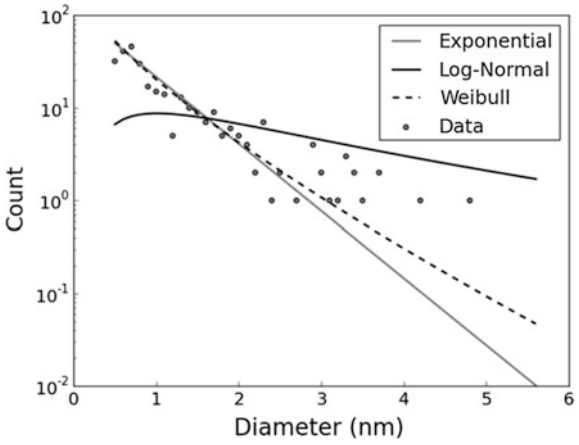

Fig. 3.2 Comparison of fits of different distribution functions to the experimental TEM data. The exponential and Weibull distribution functions are visibly much better fits than the log-normal distribution function

Sect. 3.2.2 was $\mu = 0.68 \pm 0.04$ nm. Figure 3.2 shows a comparison between the different distribution functions used to fit the TEM data. Here, the log-normal distribution is clearly a poor fit for the data, whilst the exponential and Weibull distributions each provide an excellent approximation to the experimentally observed distribution. The Weibull distribution appears to produce a somewhat closer fit than is possible with the exponential distribution, however, this improvement has no statistical significance given the very low count rates for bubbles larger than 3 nm (i.e. mostly 0 or 1 per 0.1 nm bin).

3.2.4 GISAXS Measurement and Modelling

GISAXS measurements were taken at the SAXS/WAXS beamline of the Australian Synchrotron using 10 keV X-rays (1.24 Å) and a sample-detector distance of 964 mm. Measurements were taken at 11 angles from 0° to 1° in 0.1° steps with a Dectris-Pilatus 1 M area detector. To account for gaps between detector modules, three separate 5 s measurements were taken at each angle, where the detector was diagonally displaced between each measurement. X-ray scattering patterns were obtained for both the plasma exposed sample and an undamaged reference.

Scattering patterns were fitted with both spherical (Eq. 2.32) and spheroidal (Eq. 2.37) particle models, with exponential (Eq. 3.1), log-normal (Eq. 2.48), and Weibull diameter distributions (Eq. 2.50). The depth distribution of nano-bubbles was also fitted, assuming an exponential depth distribution (Eq. 3.7). For simplicity, possible changes in bubble sizes with depth were neglected. For both the spherical and spheroidal models the average radius μ and depth τ were fitted, while in the spheroidal model the aspect ratio ϵ (i.e. height/width) was also fitted.

3.3 Comparison Between GISAXS and TEM Results

3.3.1 *Exponentially Distributed Diameters*

Example scattering patterns for both the undamaged reference and plasma-exposed sample are shown in Fig. 3.3a and b, respectively. In the undamaged sample an intense streak can be seen along the q_z axis, with intensity dropping rapidly at higher q_y. This is likely the consequence of sample surface roughness. After plasma exposure the pattern changes dramatically, with a diffuse elliptical feature clearly emerging. This additional feature is produced by X-ray scattering from nano-bubbles which have formed in the system.

The GISAXS pattern for the helium-exposed sample was fitted using the model described in Chap. 2 for both spherical and spheroidal nano-bubbles. The spheroidal nano-bubble model assumed that nano-bubbles were orientated such that their axis of rotational symmetry was parallel with the z-axis. Anisotropy between the z and x-y axes is reasonable, as the sample surface lies in the x-y plane. Nano-bubble diameters were first fitted using exponential size distributions, as described in Eq. 3.1. Nano-bubble depths were also fitted to an exponential distribution.

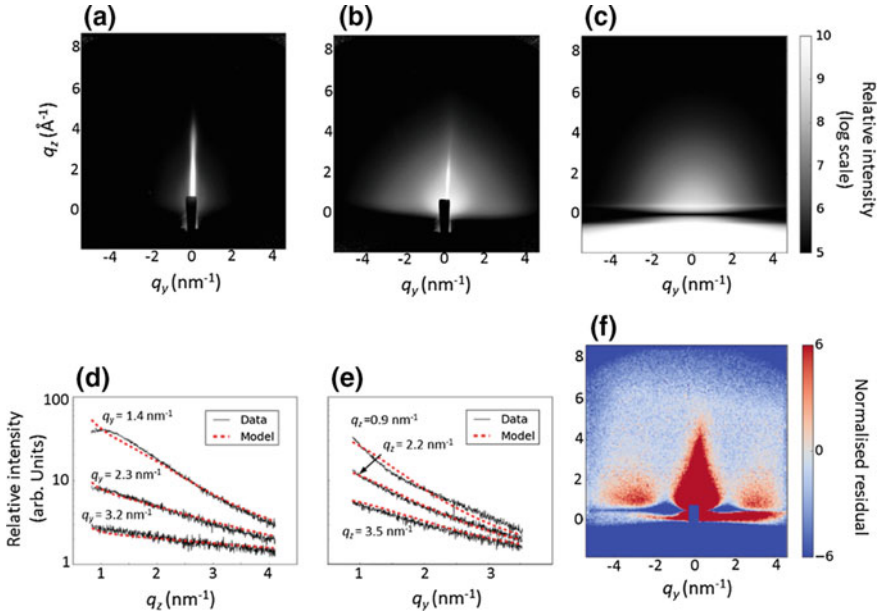

Fig. 3.3 Experimental and simulated GISAXS patterns are shown for **a** an undamaged reference sample, **b** the sample exposed to helium plasma in LHD, and **c** the simulated GISAXS model for spheroidal nano-bubbles. Examples of the **d** perpendicular and **e** parallel reciprocal space cuts used for fitting are shown for the measurement shown in (**b**), which was taken at an incident angle of 0.8° (**f**) shows an example map of the normalised residual [7]. Used with permission

The mean nano-bubble diameter μ and depth τ, as well as a constant background[2] (to account for air scattering and scattering from beamline optics) and scaling factor for Eq. 2.11 were optimised during the fit using the X-ray scattering model and fitting algorithm described in Chap. 2. For the spheroidal fit, the nano-bubble aspect ratio ϵ was also fitted. Fitting was performed by taking "cuts" of reciprocal space along directions both parallel and perpendicular to the sample surface (see Fig. 3.3d and e). All patterns taken at angles $\geq 0.5^\circ$ were fitted simultaneously. For error estimation, this large data set was divided into 10 smaller sets by assigning one tenth of the total data points to each set. Each set was then fitted independently and the spread of the results used to calculate the standard errors of the parameters used in the fitting process.

For the spherical nano-bubbles, an average diameter $\mu = 0.526 \pm 0.001$ nm and depth $\tau = 39.8 \pm 0.7$ nm were calculated, while for the spheroidal fit $\mu = 0.596 \pm 0.001$ nm, $\tau = 9.1 \pm 0.4$ nm, and the aspect ratio $\epsilon = 0.719 \pm 0.001$. The spheroids would have the same volume as perfect spheres with an average diameter $\mu = 0.54$ nm. Note that the errors quoted are the standard errors of the mean for the 10 independent fits (see [5]). The high degree of precision evident from these error ranges is the result of the large number of data points fitted and high X-ray counts, and is a clear demonstration of the stability of the fitting algorithm. It does not imply that the nano-bubble model used is this accurate.

To determine the relative quality of the spherical and spheroidal fits, the normalised residuals were calculated for each point in the patterns in the region bound by $q_y \approx 1.4\,\text{nm}^{-1}$, $q_z \approx 0.9\,\text{nm}^{-1}$ and $q_y \approx 3.5\,\text{nm}^{-1}$, $q_z \approx 4.0\,\text{nm}^{-1}$ and compiled into histograms as shown in Fig. 3.4 (see Ma et al. [6] for a more detailed discussion of this approach). For a fit where residuals are entirely due to Gaussian noise (such as X-ray counting noise, or "shot noise") these residuals should be normally distributed with a mean value of 0 and a standard deviation of 1. Standard deviations above 1 indicate that the model does not fully capture the data, while values less than 1 are statistically unreasonable, indicating overfitting. Here, the spheroidal model approaches much more closely to this ideal case with a roughly Gaussian form, a mean of −0.8 and standard deviation of 4.3. For comparison, the mean of the spherical model has a mean of 7 and standard deviation of 5.2. The spheroidal model is therefore a much better approximation of the true nano-bubble properties. This conclusion is supported by the TEM micrograph in Fig. 3.1, where the cross-sections of many of the larger nano-bubbles are evidently elliptical.

The mean nano-bubble diameter found from the GISAXS analysis of $\mu = 0.596 \pm 0.001$ nm for the spheroidal nano-bubble model is comparable to the value of $\mu = 0.68 \pm 0.04$ nm found from TEM analysis (Fig. 3.5a). The discrepancy that

[2]In principle, it should be possible to subtract the background by taking a reference pattern and subtracting it from the pattern of interest. Indeed, this was the approach taken in [4]. In practice, the background is approximately constant over most of the pattern, and the fitted background value tended to converge on similar values for all fits with similar measurement optics. This was useful as an added sanity check on the outcome of the fit—a background that deviated significantly from what was expected was a sure indication that the fitting process failed.

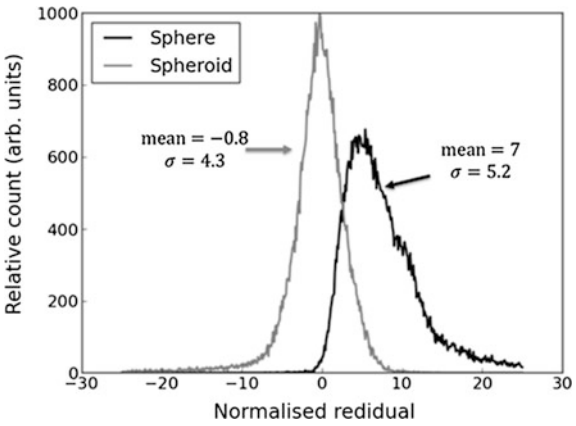

Fig. 3.4 Histograms of the normalised residuals for the spherical and spheroidal models [7]. For an ideal fit where all errors are the result of shot noise in the X-ray detector the normalised residual histograms should have a Gaussian profile with a mean of 0 and a standard deviation of 1. Used with permission

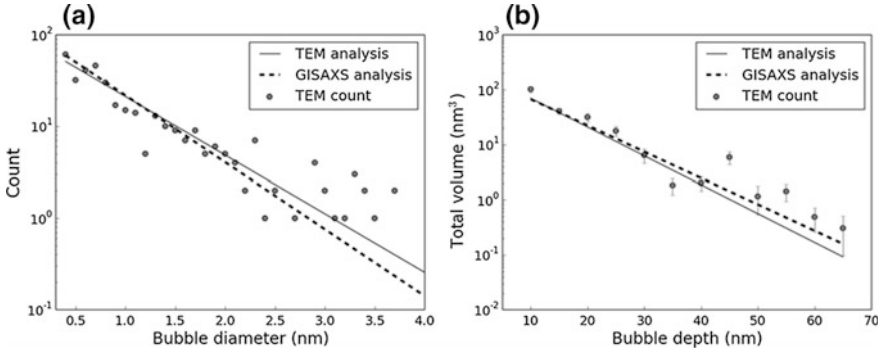

Fig. 3.5 Comparisons between **a** diameter and **b** depth distributions of nano-bubbles measured via TEM and GISAXS, assuming spheroidal bubbles [7]. Note that in (**b**) the total nano-bubble volume within each bin has been plotted. For TEM, mean bubble diameters and depths were calculated as of $\mu = 0.68 \pm 0.04$ nm and $\tau = 8.4 \pm 0.5$ nm, respectively. For GISAXS, the mean diameters and depths are $\mu = 0.596 \pm 0.001$ nm and $\tau = 9.1 \pm 0.4$ nm, respectively, assuming spheroidal bubbles

does exist can easily be explained by the statistical error from the TEM analysis. Furthermore, as TEM measurements of bubble sizes were taken by first defocussing the images to increase contrast between bubbles and the surrounding matrix, there may be a systematic tendency to overestimate bubble sizes with this approach.

The GISAXS estimate of the average particle depth τ varies greatly between spherical ($\tau = 39.8 \pm 0.7$ nm) and spheroidal ($\tau = 9.1 \pm 0.4$ nm) models. The spheroidal model appears to be in excellent agreement with the value

$\tau = 8.4 \pm 0.5$ nm measured from TEM data (Fig. 3.5b). The large discrepancy between the depth distributions calculated by the GISAXS spherical and spheroidal models indicate that estimating bubble depth distributions is very sensitive to the particle model used. Simplifying assumptions, such as modelling spheroids with a constant aspect ratio and orientation, or assuming diameter distributions are unchanged with depth, are therefore likely to affect the accuracy of these depth distribution estimates.

3.3.2 *Log-Normal and Weibull Distributions*

Log-normal and Weibull diameter distributions were also fitted using Eqs. 2.48 and 2.50 respectivel, assuming spheroidal nano-bubbles. For the log-normal diameter distribution model the median diameter was found to be $\mu = 0.8 \pm 0.2$ nm, the scale parameter $\sigma = 0.55 \pm 0.02$, the mean depth (exponentially distributed) $\tau = 8 \pm 1$ nm, and the aspect ratio $\epsilon = 0.73 \pm 0.01$. Here, it is readily apparent that the uncertainties in these measurements are much greater than those for the exponentially distributed fits.

The calculated parameters for the Weibull diameter distribution are $k = 1.43 \pm 0.05$ (dimensionless), $\lambda = 1.07 \pm 0.05$ nm, $\tau = 7.6 \pm 0.6$ nm, and $\epsilon = 0.72 \pm 0.01$.

Figure 3.6a shows a comparison between each of the different diameter distribution fits trialled. The exponential and log-normal fits are both good approximations of the TEM data, while the Weibull distribution has clearly failed to converge on the correct parameter values. This is most likely the consequence of the fitting process becoming trapped in local minima for the Weibull distribution.

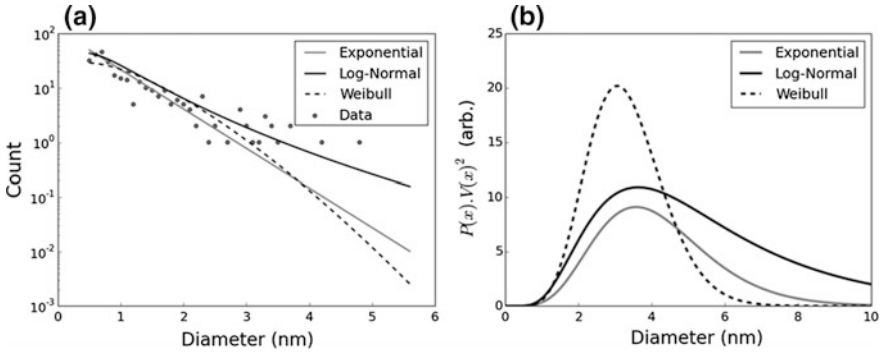

Fig. 3.6 **a** Comparison of diameter distribution fits assuming exponential, log-normal, and Weibull nan-bubble diameter distributions. Both the exponential and log-normal distributions show good agreement, while the Weibull fit is poor. Note that as the y-axis is plotted on a logarithmic scale zero values for the TEM data are not represented on this graph. **b** Distributions were multiplied by the volume squared to show the relative contributions from bubbles of each size

This apparent instability within the fit has serious implications for the use of Weibull distributions in GISAXS fitting for other patterns. It is worth noting that the actual intensity a nano-bubble contributes to the final scattering pattern is proportional to the volume squared, meaning larger bubbles contribute a disproportionally large amount to the overall pattern. Figure 3.6b shows the same distributions from (a) multiplied by the volume of the bubble squared. Here, the exponential and log-normal distributions show similar profiles, except for a much heavier tail in the case of the log-normal distribution.

It is interesting to note that both the log-normal and Weibull distribution fits show very different parameter values to those calculated by fitting the distribution functions to the TEM data. This may indicate that the use of cumulative distribution functions is more robust for Weibull distributions, but a poor approach for log-normally distributed data.

For both of these models the estimates of the average (exponentially distributed) nano-bubble depth was found to be close to the value calculated from TEM data of 8.4 ± 0.5. This indicates that the choice of diameter distribution model has little impact on depth distribution estimates.

3.3.3 Concluding Remarks

This study has provided an excellent demonstration of the power of GISAXS to measure the diameter distributions and shapes of He-induced nano-bubbles in W. It has also served as a test of the GISAXS model described in Chap. 2, and proven the accuracy of this model. Prior to the introduction of GISAXS, developing a quantitative understanding of He nano-bubble sizes has been challenging, leading most investigators to focus on largely qualitative properties of these bubbles. GISAXS thus has the potential to greatly enhance our present understanding of nano-structure formation in tungsten, and can serve as a much more detailed test of computer models of He behaviour in W.

In this work exponential, log-normal, and Weibull nano-bubble diameter distributions were all trialled assuming spheroidal nano-bubbles, and used to fit both the TEM data and GISAXS patterns. The exponential distribution was found to be the most s and provided excellent agreement with the TEM data. Both Weibull and log-normal nano-bubble distributions are also plausible, however more work will be required to improve the fit stability for these functions. This lack of stability may indicate an over-parametrisation. The log-normal and Weibull distributions are both defined by 2 parameters, while only a single parameter is necessary for an exponential distribution. If only a single parameter is necessary, the second parameter may be "getting in the way" of the optimisation process, rather than making a meaningful contribution to the fit.

Spherical and spheroidal particle models were also trialled assuming exponentially distributed nano-bubble sizes. The spheroidal model produced a much better fit, indicating that there is some tendency for nano-bubbles to be compressed in the direction normal to the sample surface. This seems plausible from TEM data, as many bubbles are clearly non-spherical. Nano-bubble depth distributions were also estimated, with the spheroidal model providing excellent agreement with the TEM data.

GISAXS is also an excellent complement to TEM. While TEM is ideal for studying the shapes and properties of individual particles, statistical limitations and the man-hours required for sample preparation and bubble counting makes deriving more generalised information about nano-bubble sizes time-consuming and tedious. GISAXS, on the other hand, cannot reveal information about individual structures at all, but excels at studying distributions of large numbers of particles simultaneously. Such a measurement can be performed in several minutes, and, after the initial time commitment required to develop the model and fitting code, analysis can be performed in a matter of hours. As most of the work is being done by a computer, it is trivial to set up a routine that would allow many patterns to be fitted overnight or over a weekend with little human intervention.[3] The main drawback is that the technique requires beam-time at a synchrotron facility, which makes the technique somewhat less accessible.

TEM bubble counting could potentially be sped-up with the careful application of image analysis software. However, the sample preparation required for TEM studies is extensive, as samples must be thinned to a few 10 s of nm so that an electron beam can pass through them without multiple scattering. This thinning process can introduce artefacts, further confounding analysis. In a sense, this work does as much to validate the use of TEM for studying helium nano-bubbles as it does for GISAXS—it is the mutual agreement of these two radically different techniques that demonstrates their mutual effectiveness.

In the following chapters I will provide further demonstrations of the GISAXS technique. It has been used to study the effects of He fluence, sample surface temperature, and the effects of mixed H/He and pure H plasma. Thus, we will move beyond a mere technical demonstration and towards the use of GISAXS to address real scientific problems which hitherto have been prohibitively difficult to study in a quantitative sense.

[3]It is important to emphasise that computers are dumb, mindless machines and should never be trusted to do anything by themselves. One should always be careful to verify that the fits are reasonable, and that the fitting process is working as intended.

References

1. E. Bernard, R. Sakamoto, N. Yoshida, H. Yamada, Temperature impact on W surface exposed to He plasma in LHD and its consequences for the material properties. J. Nucl. Mater. **463**, 316–319 (2015). https://doi.org/10.1016/j.jnucmat.2014.11.041
2. D. Babonneau, S. Peripolli, M.-F. Beaufort, J.-F. Barbot, J.-P. Simon, GISAXS study of cavities and 113 defects induced by neon and helium implantation in silicon. J. Appl. Crystallogr. **40**, s350–s354 (2007). https://doi.org/10.1107/S0021889806043755
3. B. Efron, C. Stein, The jackknife estimate of variance, 586–596 (1981). https://doi.org/10.1214/aos/1176345462
4. M. Thompson, P. Kluth, R.P.P. Doerner, N. Kirby, C. Corr, Probing helium nano-bubble formation in tungsten with grazing incidence small angle x-ray scattering. Nucl. Fusion **55**, 42001 (2015). https://doi.org/10.1088/0029-5515/55/4/042001
5. B.E. Dowd, W.H. Greene, E.C. Norton, Computation of standard errors. Health Serv. Res. **49**, 731–750 (2014). https://doi.org/10.1111/1475-6773.12122
6. J. Ma, H. Zhao, P. Schuck, A histogram approach to the quality of fit in sedimentation velocity analyses. Anal. Biochem. **483**, 1–3 (2015). https://doi.org/10.1016/j.ab.2015.04.029
7. M. Thompson, R. Sakamoto, E. Bernard, N. Kirby, P. Kluth, D. Riley, C. Corr, GISAXS modelling of helium-induced nano-bubble formation in tungsten and comparison with TEM. J. Nucl. Mater. **473**, 6–12 (2016). https://doi.org/10.1016/j.jnucmat.2016.01.038

Chapter 4
Effect of He Fluence on Nano-bubble Growth

4.1 He Fluence and W Performance

He loading and subsequent nano-structure formation is a serious concern for the development of plasma facing materials. In a large device such as ITER, plasma facing surfaces will be exposed to very high plasma fluences over the life of the machine, so understanding the long-term effects of this particle exposure on material performance is essential. He is of particular concern as it can be stably retained in W up to temperatures >1000 K [1], making it very difficult to remove once incorporated. Further, He is insoluble, instead precipitating out in the form of nano-bubbles.

If He is implanted into W, nano-bubbles will form. This is unavoidable. Less clear is whether we can expect nano-bubbles to continue to form as the total He fluence increases, or whether the nano-bubble concentrations/sizes saturate at some point. Due to the difficulties in systematically measuring He nano-bubble sizes and concentrations using traditional techniques such as TEM, few studies have focussed on quantitatively measuring He nano-bubble growth. In the detailed TEM study by Miyamoto et al. [2] both dimeter and concentration saturation occurred in plasma-exposed samples below 773 K at a fluence of 5×10^{23} He/m^2, offering some hope to the long-term stability of W under He plasma.

He is known to reduce the thermal conductivity of W. For instance, Cui et al. found that the thermal conductivity in the He damaged region of W exposed to He plasma at 773 K to a fluence of 10^{26} He/m^2 was reduced by more than 80% compared with undamaged W [3]. If the He damaged layer continues to grow with successive He exposure, this could lead to a significantly higher surface temperature during plasma exposure.

In order to develop a better understanding of this phenomenon the fusion community will need access to advanced techniques beyond TEM. In this chapter, a study is discussed which investigates the role of He fluence on nano-bubble growth using GISAXS, providing unprecedented precision for nano-bubble diameter

M. Thompson, *Helium Nano-bubble Formation in Tungsten*, Springer Theses,
https://doi.org/10.1007/978-3-319-96011-1_4

measurements. This work was performed on two separate linear plasma devices: the Australian National University's MAGnetised Plasma Interaction Experiment (MAGPIE), and the University of California, San Diego's PISCES-A device.

4.2 Experimental Overview

4.2.1 Sample Preparation

In this chapter, two separate fluence experiments are described: one with the MAGPIE linear plasma device, and one with the PISCES-A device. These experiments utilised different samples, prepared by different institutions.

For the MAGPIE experiments, $10 \times 10 \times 2$ mm samples were prepared by the Australian Nuclear Science and Technology Organisation. All samples were cut from a single large polycrystalline block of 99.97% purity W which had been sourced from PLANSEE. The samples were prepared such that they were as similar as possible to the ITER divertor specifications. The upper surface was polished using chemo-mechanical processes to produce a mirror finish. PISCES-A samples were also produced from high purity W and polished to a mirror finish, the main difference being that they were cut into 5 mm diameter circular buttons.

4.2.2 MAGPIE—The MAGnetised Plasma Interaction Experiment

MAGPIE is a linear plasma device located in the Plasma Research Laboratory of the Australian National University, shown in Fig. 4.1. The plasma is generated in the source chamber by a radio-frequency (RF) antenna, where ionisation occurs predominantly by collisions from excited free electrons. The plasma then diffuses towards the target chamber. Both the source and target chamber are surrounded by water-cooled solenoids, which have separate power supplies to allow the magnetic fields in the source and target chambers to be varied independently. The solenoids in the target chamber are much more tightly spaced, allowing much stronger magnetic fields in this region of up to 0.19 T. This magnetic configuration produces a magnetic pinch within the plasma, increasing the plasma density in the target region, thereby allowing higher plasma fluxes to be incident on the target. A more detailed description of the MAGPIE device can be found in [4].

Four samples were exposed to pure He plasma in MAGPIE at He fluences: $2.7 \times 10^{24}\,\mathrm{He/m^2}$, $5.4 \times 10^{24}\,\mathrm{He/m^2}$, $1.1 \times 10^{25}\,\mathrm{He/m^2}$ and $2.2 \times 10^{25}\,\mathrm{He/m^2}$. Prior to exposure, MAGPIE was evacuated to a base pressure below 2×10^{-5} Torr. Plasma exposure was performed with pulsed 1 kW RF input power at a duty cycle of 50% to prevent the chamber from overheating. The background gas pressure was

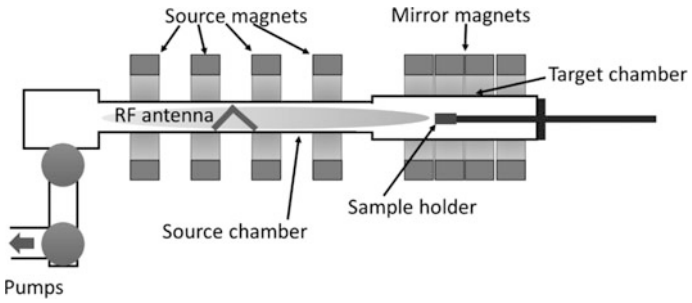

Fig. 4.1 Schematic diagram of the MAGPIE linear plasma device, highlighting the key components. Plasma is generated by a radio-frequency antenna in the source region and diffuses from there towards the target chamber. The magnetic field in the target chamber is much higher than that in the source region increasing the flux at the sample position

maintained at 10 mTorr. Electron and ion densities in the plasma in front of the sample were measured to be $5.5 \times 10^{16}/\mathrm{m}^2$ and the sheath potential −37 V via Langmuir probe. The electron temperature was 11 eV. For radio-frequency plasma the ion temperature is expected to be significantly lower than this. Consequently, most energy of the impinging ions will be contributed by acceleration across the plasma sheath, so the He ion energy on impact with the sample surface will be somewhat higher than 37 eV.

Sample temperatures were not measured during exposure. To estimate the sample temperature, a further sample was exposed to similar plasma conditions and its temperature measured from the back surface via a pyrometer, giving an approximate sample temperature of 473 K for all samples. As samples were relatively thin (2 mm) the front surface temperature should be similar. A fifth sample was used as a reference for GISAXS measurements.

4.2.3 PISCES-A

The PISCES-A device is another linear divertor simulator which was designed to simulate boundary plasma phenomenon, but also includes materials testing capabilities (see Fig. 4.2). The plasma is generated by a reflex arc discharge from a LaB_6 disk cathode to a cooled cylindrical anode [5]. This plasma then drifts down an evacuated chamber towards a water-cooled molybdenum target [6], which can accommodate samples for plasma-material studies. Sample temperature is measured with a spring-loaded thermocouple which is pressed against the back of the sample.

For the PISCES-A experiments samples were exposed to four different He plasma fluences: $1.2 \times 10^{23}\,\mathrm{He}/\mathrm{m}^2$, $1.6 \times 10^{24}\,\mathrm{He}/\mathrm{m}^2$, $1.2 \times 10^{25}\,\mathrm{He}/\mathrm{m}^2$ and $6.8 \times 10^{25}\,\mathrm{He}/\mathrm{m}^2$. Surface temperatures were maintained between 623 and 673 K.

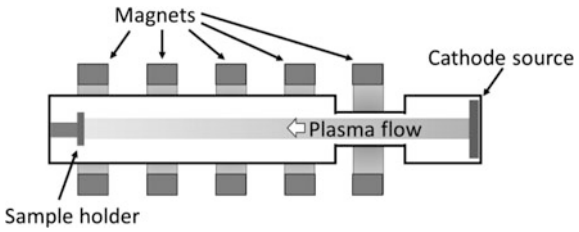

Fig. 4.2 Schematic of the PISCES-A linear plasma device. The plasma is generated at the cathode and moves down the main chamber towards the target

As the samples for the PISCES-A experiments were prepared separately an additional sample was prepared as a reference for GISAXS measurements.

4.2.4 Methods for Measuring Nano-structure Growth

Nano-bubble growth was measured via GISAXS at the Australian Synchrotron, using the methods outlined in Sect. 3.2.4. Transmission electron microscopy was also performed for the 2.2×10^{25} He/m^2 fluence MAGPIE sample at Australian Nuclear Science and Technology Organisation using a JEOL 2200FS TEM operating at 200 keV. W specimens were prepared for TEM by first depositing a protective Pt layer on the sampe surface before cutting out a thin foil with a focussed ion beam (FIB). Bubbles were identified by imaging the foil under high resolution bright field conditions, varying the focus from under-focus to over-focus.

4.3 Results

4.3.1 Influence of Fluence on He Nano-bubble Diameters

Examples of GISAXS patterns are shown in Fig. 4.3 for samples exposed to He plasma in MAGPIE and PISCES-A. For the MAGPIE reference sample (Fig. 4.3a) X-rays are scattered predominantly within an intense streak along the q_z axis, which is likely to be a consequence of surface roughness. The PISCES-A reference sample was similar, and is not shown.

After He exposure (Fig. 4.3b–f) the scattering pattern changes considerably, with significant scattering away from the q_z axis in all samples. For MAGPIE samples, nano-bubble formation lead to the emergence of a semi-elliptical contribution superimposed over the top of the central streak. The nano-bubble size distributions were calculated by fitting the data with the spheroidal GISAXS model described in Chap. 2, assuming exponential bubble size distributions. The results of this analysis are summarised in Fig. 4.4 and Table 4.1. Note that the two highest fluence PISCES-A samples have been excluded from Fig. 4.4 as nano-bubble fitting was confounded by the presence of additional, non-spheroidal features. 0.52–0.57 nm

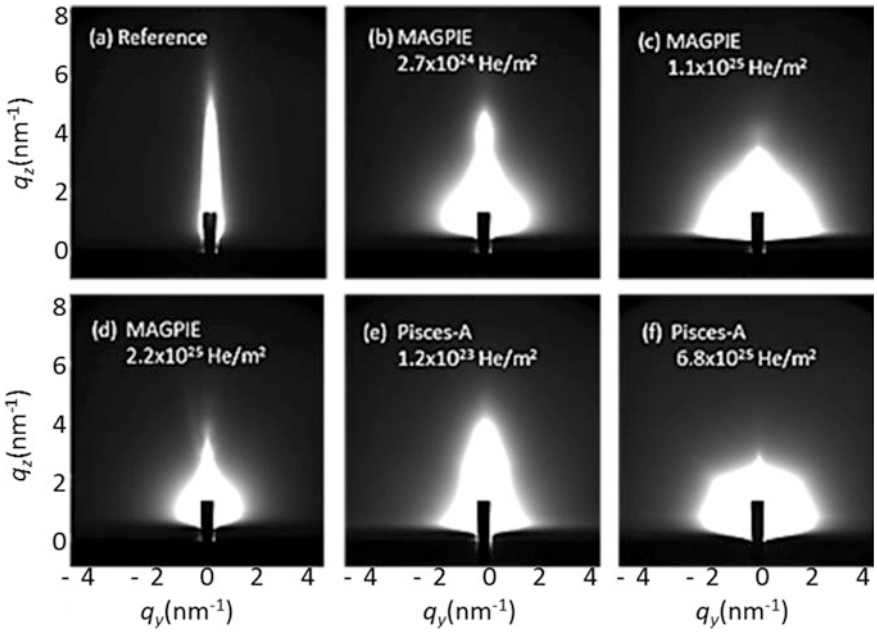

Fig. 4.3 GISAXS patterns taken at an angle of incidence of 0.5° are shown for: **a** an unexposed reference sample, **b** a MAGPIE helium fluence of $2.7 \times 10^{24}\mathrm{He/m^2}$, **c** MAGPIE fluence of $1.1 \times 10^{25}\mathrm{He/m^2}$, **d** MAGPIE fluence of $2.2 \times 10^{25}\mathrm{He/m^2}$, **e** PISCES-A fluence of $1.2 \times 10^{23}\mathrm{He/m^2}$, and **f** PISCES-A fluence $6.8 \times 10^{25}\mathrm{He/m^2}$. Axes show the reciprocal space co-ordinates for each pattern

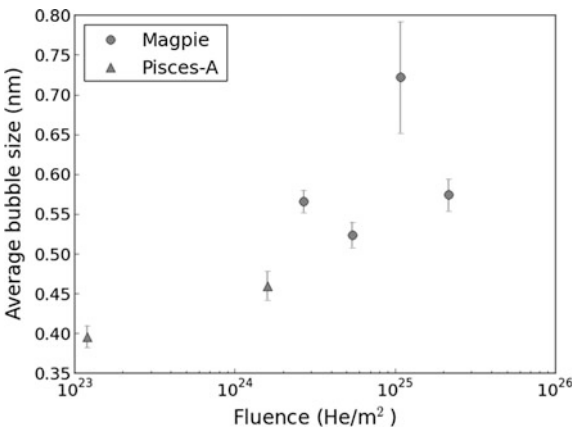

Fig. 4.4 Average nano-bubble diameters (μ) are shown for samples exposed to He plasma in MAGPIE and PISCES-A. The higher fluence $\left(\geq 1.2 \times 10^{25}\mathrm{He/m^2}\right)$ samples have been excluded as the nano-bubble measurements were confounded by additional contributions to the scattering patterns

diameter bubbles formed in samples exposed to MAGPIE plasmas at fluences of $2.7 \times 10^{24}\,\mathrm{He/m^2}$, $5.4 \times 10^{24}\,\mathrm{He/m^2}$ and $2.2 \times 10^{25}\,\mathrm{He/m^2}$, while larger ($0.72 \pm 0.07$ nm) bubbles formed at the intermediate fluence of $1.1 \times 10^{25}\,\mathrm{He/m^2}$.

Table 4.1 Effect of plasma fluence on nano-bubble formation

Device	He fluence ($\times 10^{20}/m^2$)	Surface temperature (K)	Mean diameter (x–y plane, nm)	Aspect ratio (z/y)
MAGPIE	2.7×10^{24}	473	0.57 ± 0.01	0.74 ± 0.01
MAGPIE	5.4×10^{24}	473	0.52 ± 0.02	0.70 ± 0.01
MAGPIE	1.1×10^{25}	473	0.72 ± 0.07	0.78 ± 0.01
MAGPIE	2.2×10^{25}	473	0.57 ± 0.02	0.74 ± 0.01
PISCES-A	1.2×10^{23}	623–673	0.40 ± 0.01	0.68 ± 0.01
PISCES-A	1.6×10^{24}	623–673	0.46 ± 0.02	0.77 ± 0.01
PISCES-A	1.2×10^{25}	623–673	Unidentified features	
PISCES-A	6.8×10^{25}	623–673	Unidentified features	

The origin of this discrepancy is unclear, but it seems improbable that larger bubbles should form at a fluence of $1.1 \times 10^{25}\,He/m^2$ than $2.2 \times 10^{25}\,He/m^2$. As sample temperatures were estimated by comparison with plasma exposures under nominally similar plasmas rather than during the actual exposure of the samples being reported here, it is possible that the $1.1 \times 10^{25}\,He/m^2$ sample was exposed to a higher temperature than the others. This could have occurred if the thermal contact for this sample with the heat sink was poor, for instance. In all samples, the height to width ratios of the spheroids were similar, ranging from 0.7 to 0.8.

Figure 4.5 shows a TEM micrograph of the $2.2 \times 10^{25}\,He/m^2$ fluence MAGPIE sample highlighting the key features which had been observed. Notably, there appears to be a distinct disordered region within the first 5–10 nm from the sample surface, which is most likely the result of He retention within this region. Nano-bubble formation was confirmed by looking at changes in image contrast while under-focussing and over-focussing the TEM objective lens, as shown in Fig. 4.6. The bubble shown appears to be approximately 1 nm across. As few bubbles were sampled, information about depth distributions cannot be deduced from this TEM study.

At a fluence of $1.2 \times 10^{23}\,He/m^2$ in PISCES-A an average nano-bubble size of 0.40 ± 0.01 nm was determined, increasing to 0.46 ± 0.02 nm at a fluence of $1.6 \times 10^{24}\,He/m^2$. This result is indicative of nano-bubble growth with increasing fluence. At fluences above $1.2 \times 10^{25}\,He/m^2$ the PISCES-A sample scattering patterns show dramatically different features, with the intensity plot taking on an almost polygonal form (see Fig. 4.3f for an example). These more complicated patterns indicate the presence of non-spheroidal features within the samples. If this feature were the consequence of some change in the nano-bubble shape, such as faceted faces, the polygonal shape observed would imply that these features must be highly orientated as randomly orientated particles of any shape will produce a spherically symmetrical pattern. As the samples were polycrystalline W such a high degree of ordering seems implausible. Alternatively, the growth of surface features could also account for this new feature, with ordering naturally occurring due to the

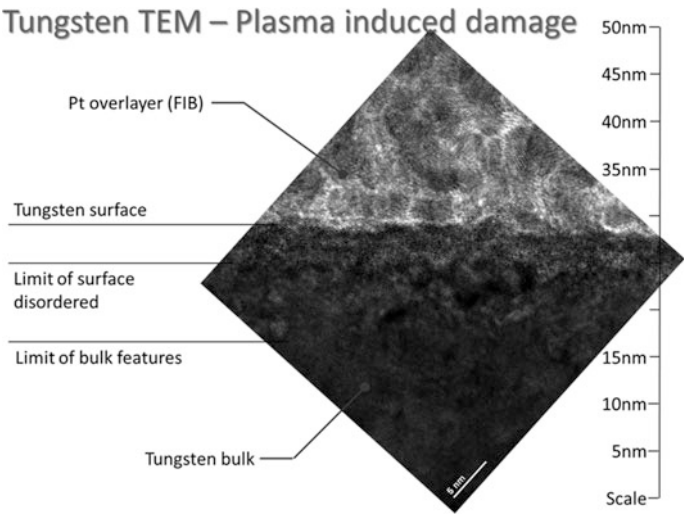

Fig. 4.5 TEM micrograph showing key features of the $2.2 \times 10^{25}\,\mathrm{He/m^2}$ fluence MAGPIE sample. Of particular interest is the mottled region between the Pt overlayer and the W bulk, which is likely a region of disordered W resulting from He retention and nano-structure formation in this area

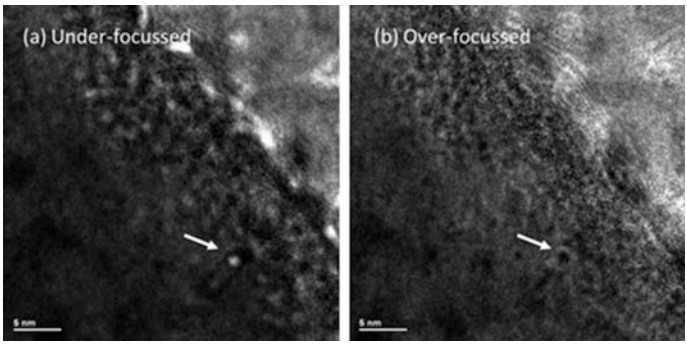

Fig. 4.6 **a** Under-focussed and **b** over-focussed TEM micrographs showing the presence of a $\sim$1 nm bubble within the $2.2 \times 10^{25}\mathrm{He/m^2}$ fluence MAGPIE sample. The nano-bubble appears as a bright spot in the under-focussed image, and a bright ring about a dark spot in the over-focussed image

anisotropy of such growth. A possible candidate would be the pyramidal nano-structures observed by Parish et al. [7].

One final possibility is that this may be the consequence of ordering between bubbles. This effect has been observed before in many body-centred-cubic metals in

a TEM study by Johnson and Mazey [8]. In their work, 1.5–2 nm bubbles were found to self-organise in W at 775 K, with a repeating distance of ~6.2 nm. This explanation is particularly compelling as electron diffraction revealed an analogous hexagonal pattern for the direct beam. It will be possible to investigate this in future by incorporating better support for structure factors in the X-ray scattering model.

4.3.2 *Effect of Fluence on Nano-bubble Depths*

Nano-bubble depth distributions were also estimated, assuming that nano-bubble depths are exponentially distributed. These results are summarised in Fig. 4.7. Here, dramatic differences in the fit can be seen between the nano-bubble depths for both MAGPIE and PISCES-A samples, with average depths in MAGPIE ranging between ~1–15, and ~1–2 nm for their PISCES-A counterparts. The differences between PISCES-A and MAGPIE may be more a consequence of the differences in fluence than a difference between the two devices. 1–2 nm is the approximate depth low energy (tens of eV) He ions penetrate beneath the sample surface, referred to hereafter as the "implantation zone". This result could indicate that, at low fluences, He nano-bubbles precipitate mostly within the implantation zone.

Toward higher fluences there appears to be a trend towards increasing average nano-bubble depth with increasing fluence. This could mean that once nano-bubbles are no longer able to increase in size additional He is accommodated by diffusing deeper into the material, with the depth He penetrates into the sample increasing with increasing fluence.

However, the calculated errors for these fits were quite large (>20% for all measurements), indicating poor convergence. Determining depth distributions with GISAXS is much more difficult than bubble size distributions as it relies heavily on comparing subtle differences in pattern intensities, especially at low q_z values.

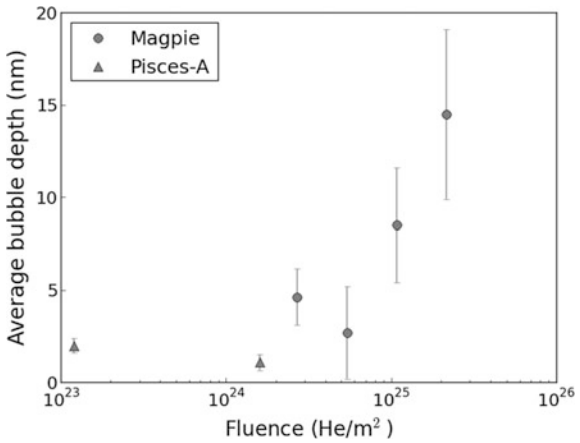

Fig. 4.7 Average depth values (τ) calculated from GISAXS pattern fitting. Results for samples exposed to He plasma in PISCES-A are much lower than those for MAGPIE exposed samples. This could be a consequence of the lower plasma fluence for those samples, or alternatively, some difference in the implantation depth between the two experiments

Further, the model which was fitted to the data assumed that the bubble concentration reduced exponentially with distance from the sample surface—it is very likely that nano-bubble distributions differ substantially between the implantation zone, where He is supplied directly from the plasma, and deeper parts of the sample where He must first diffuse downward.

One confounding factor in the depth modelling is the presence of a diffuse background in the scatteringg patterns. This background is readily apparent in patterns after adjusting brightness/contrast, and appears as a rectangular-shaped plateau of $\sim$100–300 counts per pixel (this feature can be easily distinguished in Fig. 3.3f). This contribution is believed to result from fluorescence from the collimating slits in the SAXS/WAXS beamline on account of the fact that it is energy-sensitive: it appears for 10 keV X-rays, but disappears at 16 keV. These diffuse fluorescence X-rays then either pass directly through the Kapton window of the detector chamber or reflect from the sample surface and contribute to the pattern. As the incidence angle of the X-rays is increased (i.e. by rotating the sample) the sample obstructs these X-rays more, reducing the background contribution. Thus, for larger samples the background contribution changes with angle. This effect has frustrated efforts to measure structure depth distributions. It should be possible to avoid this by careful GISAXS experimental design, such as careful energy selection to minimise unwanted scattering, or by subtracting the background from experimental data rather than through a fitting process.

4.4 Summary

Nano-bubble formation in W samples exposed to He plasma in the MAGPIE and PISCES-A linear plasma devices across a range of plasma fluences from 1.2×10^{23} He/m^2 to 6.8×10^{25} He/m^2 was investigated to determine the effect of total He fluence on nano-bubble growth.

Nano-bubble growth between fluences of 1.2×10^{23} He/m^2 and 1.6×10^{24} He/m^2 was evident, with nano-bubble diameters increasing by $\sim$15% from 0.40 ± 0.01 to 0.46 ± 0.02 nm for exposure temperatures between 623 and 673 K. This represents an approximately 50% increase in average nano-bubble volume. Measurements for higher fluence samples were confounded by the presence of additional contributions to the GISAXS scattering patterns. The nature of these additional contributions presently is not known, though it could be a consequence of surface modification or nano-bubble ordering.

For the MAGPIE experiments a fluence range from 2.7×10^{24} He/m^2 to 2.2×10^{25} He/m^2 was investigated for a W temperature of approximately 473 K. Most samples showed nano-bubble diameters between 0.52 and 0.57 nm, indicating that nano-bubble diameter increases saturate with increasing fluence at some fluence lower than 2.7×10^{24} He/m^2 for this experimental setup.

Measurements of depth distributions of nano-bubbles was also attempted. Average nano-bubble depths tended to increase at higher fluences, however, errors for these measurements were very large so further investigation will be necessary to clarify this behaviour.

References

1. K. Tokunaga, R.P. Doerner, R. Seraydarian, N. Noda, Y. Kubota, N. Yoshida, T. Sogabe, T. Kato, B. Schedler, Surface morphology and helium retention on tungsten exposed to low energy and high flux helium plasma. J. Nucl. Mater. **313**, 92–96 (2003). https://doi.org/10.1016/S0022-3115(02)01362-4
2. M. Miyamoto, S. Mikami, H. Nagashima, N. Iijima, D. Nishijima, R.P. Doerner, N. Yoshida, H. Watanabe, Y. Ueda, A. Sagara, Systematic investigation of the formation behavior of helium bubbles in tungsten. J. Nucl. Mater. **463**, 333–336 (2015). https://doi.org/10.1016/j.jnucmat.2014.10.098
3. S. Cui, M. Simmonds, W. Qin, F. Ren, G.R. Tynan, R.P. Doerner, R. Chen, Thermal conductivity reduction of tungsten plasma facing material due to helium plasma irradiation in PISCES using the improved 3-omega method. J. Nucl. Mater. (2017). https://doi.org/10.1016/j.jnucmat.2017.01.023
4. B.D. Blackwell, J.F. Caneses, C.M. Samuell, J. Wach, J. Howard, C. Corr, Design and characterization of the Magnetized Plasma Interaction Experiment (MAGPIE): a new source for plasma–material interaction studies. Plasma Sources Sci. Technol. **21**, 55033 (2012). https://doi.org/10.1088/0963-0252/21/5/055033
5. D.U.B. Aussems, D. Nishijima, C. Brandt, R.P. Doerner, N.J.L. Cardozo, Spectroscopic characterization and imaging of laser- and unipolar arc-induced plasmas. J. Appl. Phys. **116**, 63301 (2014). https://doi.org/10.1063/1.4892675
6. E.M. Hollmann, K.R. Umstadter, R.P. Doerner, J. Munoz, D. Nishijima, A.Y. Pigarov, Measurement of parallel transport of B + and Al2 + impurities in a linear He + plasma. J. Nucl. Mater. **415**, S425–S429 (2011). https://doi.org/10.1016/j.jnucmat.2010.10.067
7. C.M. Parish, H. Hijazi, H.M. Meyer, F.W. Meyer, Effect of tungsten crystallographic orientation on He-ion-induced surface morphology changes. Acta Mater. **62**, 173–181 (2014). https://doi.org/10.1016/j.actamat.2013.09.045
8. P.B. Johnson, D.J. Mazey, Gas-bubble superlattice formation in bcc metals. J. Nucl. Mater. **218**, 273–288 (1995). https://doi.org/10.1016/0022-3115(94)00674-1

Chapter 5
Effect of Sample Temperature and Transient Heat Loading on Nano-bubble Growth

5.1 Temperature and Nano-bubbles

Temperature plays a critical role in the formation of He nano-bubbles in W. Generally, the higher the temperature the larger the bubbles which form [1], though there is evidence that nano-bubble sizes may not vary below a certain temperature [2]. This may be the consequence of different mechanisms driving bubble growth at different temperatures: at low temperatures growth occurs predominantly from vacancy/He diffusion, while at higher temperatures bubbles are mobile allowing growth via mergers. This latter mechanism is of particular interest to the fusion materials community as this means of growth has been found to lead to significant surface modification which could have an adverse impact on W performance [1]. In extreme cases, progressive surface roughening can lead to highly inhomogeneous heating, with small localised parts of the material reaching temperatures high enough to drive W melting and droplet emission into the plasma [3, 4].

Presently, it is not clear precisely where the dividing line between diffusion-driven and merger-driven bubble growth occurs. Miyamoto et al. [2] study into this phenomenon indicates that the crossover temperature may depend to some extent on the nature of the sample itself, with a lower merger threshold temperature observed under in situ TEM than that for a bulk sample exposed to He plasma. On the other hand, El-Atwani et al. [5] observed no bubble coalescence during in situ TEM even for temperatures up to 1223 K. Instead, they found that bubble growth was more sensitive to vacancy availability, with larger bubbles forming where vacancies were abundant. This was achieved by using He implantation energies above the threshold required for Frenkel pair formation in W. Taken together, these studies indicate a complex relationship between incident He ion energy (vacancy availability) and temperature (vacancy and nano-bubble mobility) on nano-bubble formation.

In a device such as ITER, transient thermal loading from Edge Localised Modes (ELMs) and other plasma instabilities will lead to short-duration temperature

M. Thompson, *Helium Nano-bubble Formation in Tungsten*, Springer Theses,
https://doi.org/10.1007/978-3-319-96011-1_5

spikes. Consequently, it is not enough to simply understand the behaviour of He nano-structures under steady-state temperature and plasma conditions—one must also investigate how these short-term temperature spikes influence nano-structure formation as well.

In this chapter, the results of a series of experiments utilising GISAXS to measure He nano-bubble formation are reported. To investigate steady-state temperature effects, separate experiments were conducted on both the NAGDIS-II [6] and PISCES-A [7] linear plasma devices. The influence of transient thermal loading was then studied by exposing W samples pre-loaded with He plasma in PISCES-A to an ELMy He discharge in the DIII-D tokamak [8]. A further study was attempted where samples exposed to He plasma in MAGPIE were then subsequently annealed at 1073 K, however, surface oxidation destroyed the nano-structures which were to be studied.

5.2 Experimental Procedure

5.2.1 NAGDIS-II

The NAGDIS-II device is a linear plasma divertor simulator where the plasma is generated by a DC discharge between a LaB_6 cathode and a copper anode [6]. As the ionised fraction in the discharge is low ($\sim$1%), high plasma intensities in the exposure chamber were maintained by operating the cathode at high neutral pressures. Neutral gas is then pumped out of the exposure chamber via a strong differential pumping system producing a plasma with an ionised fraction greater than 10%.

Three samples were prepared for He plasma exposure in NAGDIS-II by first cutting then polishing $10 \times 10 \times 2$ mm polycrystalline W samples. A fourth sample was also prepared, but was not exposed to plasma. After polishing, samples had a visibly convex surface, and visible scratches from the polishing process.

Samples were exposed to similar plasma fluences (5.3×10^{25} He/m^2, 4.4×10^{25} He/m^2, 4.2×10^{25} He/m^2) at surface temperatures of 843–903 K, 943 K, and 1023 K, respectively. Sample temperature was controlled by changing the plasma flux, where the plasma fluxes for each sample were 1.5×10^{22} He/m^2/s, 2.4×10^{22} He/m^2/s, and 4.7×10^{22} He/m^2/s, respectively. Nano-bubble growth was measured via GISAXS at the Australian Synchrotron across incident angles from 0.5° to 1.0° in 0.1° steps. Fitting was performed with the methods outlined in Sect. 3.2.4, where several patterns taken at different incident angles were fitted simultaneously for each sample.

5.2.2 PISCES-A + DIII-D

To investigate the role of transient heat loading on He nano-bubble formation, W samples were exposed to an ELMy plasma within the DIII-D tokamak. The DIII-D device is a versatile divertor tokamak operated by General Atomics, and is an upgrade of the earlier Doublet III tokamak [9] (Fig. 5.1). DIII-D is so-named for its "D" shaped plasma, and was developed as a versatile device which can achieve high-performance plasma despite its modest size [10]. The tokamak operates in a pulsed mode, with plasma pulses up to 10 s long. DIII-D is equipped with the Divertor Materials Evaluation System (DiMES), which facilitates studies of material performance under tokamak plasma, including high energy transient events such as ELMs [11].

For this experimental series, 12 W "buttons" were prepared, with 1 being reserved as an undamaged reference sample. To determine the effects of He pre-loading prior to transient heating 6 samples were pre-exposed to pure He plasma in PISCES-A to a fluence of $1 \times 10^{26} \mathrm{He}/\mathrm{m}^2$, 3 with a sample surface temperature of 773 K, and 3 with a surface temperature 973 K. 5 virgin samples and 2 of each of the 773 and 973 K samples were then exposed to a single 3 s He discharge in DIII-D, which included approximately 150 ELM events. ELMs typically lasted 2–3 ms, with

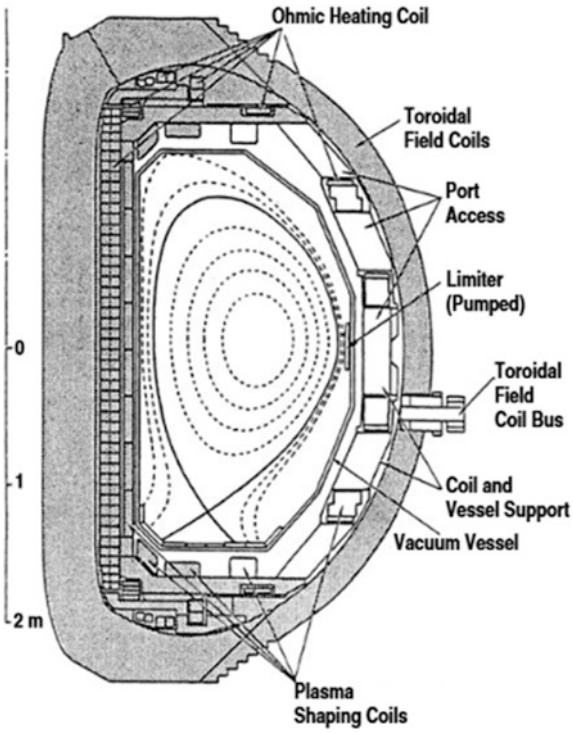

Fig. 5.1 Cross-section of the DIII-D tokamak, showing key components of the device. In the centre, a typical divertor plasma configuration is shown. Image from [10]. Used with permission

a typical energy density of approximately 60 kJ/m^2. During ELMs plasma densities and temperatures reached 2×10^{19} ions/m^3 and 250 eV, respectively, compared with 1×10^{19} ions/m^3 and 50 eV during periods between ELMs.

The work described here was part of a broader collaboration, and features only a subset of that work. An overview of the collaboration's wider methodology and results can be found in reference [12]. Please note that the GISAXS fitting method has been revised since [12] went to press, so results here may differ somewhat from that earlier publication. GISAXS measurements were performed using a similar process to those for NAGDIS-II samples. Nano-bubble size distributions were found to be fundamentally different for samples which had been exposed to ELMs in DIII-D, requiring two different nano-bubble diameter distributions to be fitted simultaneously. This is discussed in Sect. 5.3.2.

5.3 Results

5.3.1 Effect of Temperature on Bubble Growth

Figure 5.2 shows the effect of temperature on nano-bubble diameters for samples exposed to He plasma in NAGDIS-II and PISCES-A. Samples exposed to NAGDIS-II show a significant increase in nano-bubble sizes as temperatures increase from $\sim$873 to 943 K, but no further increase beyond this. Interestingly, the nano-bubble diameters observed at $\sim$873 K are comparable to those found for W exposed to He plasma in MAGPIE at the much lower temperature of 473 K (i.e. $\mu \approx 0.5$nm).

The similarity between the nano-bubble sizes at 943 and 1123 K indicates that nano-bubble growth at high temperatures ($> \sim$900 K) is either fluence limited, time

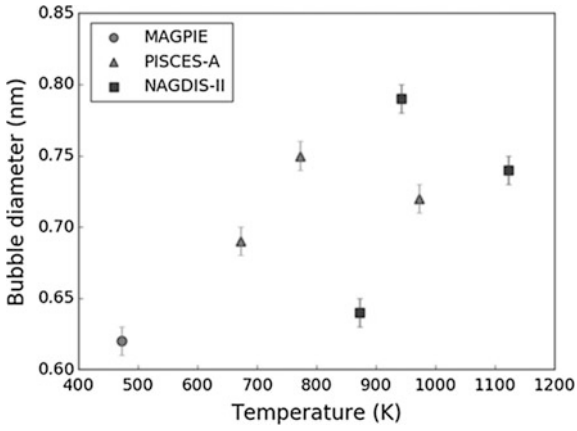

Fig. 5.2 Mean nano-bubble sizes for plasma exposures across a range of sample temperatures are shown for both NAGDIS-II and PISCES-A [13]. He fluence in NAGDIS-II PISCES-A samples were approximately 5×10^{25} He/m^2 and 1×10^{26} He/m^2, respectively. For comparison, the mean bubble size for samples exposed to plasma in MAGPIE to a fluence of 2.2×10^{25} He/m^2 is also shown. Image used with permission

limited, or both. Fluence limited growth has been demonstrated in situ TEM work for relatively low He ion fluences ($<10^{21}$ He/m^2) [2], however this study does not show how temperature affects this process beyond the coalescence threshold temperature. Exposure time could also be a factor. As heating in NAGDIS-II was achieved by varying the plasma flux, the higher temperature sample was only exposed to plasma for half the time of the lower temperature sample, meaning less time was available for nano-bubble formation. A more systematic study will be required in order to obtain more definitive answers.

He is also known to produce surface pitting in W, as shown in the SEM micrographs in Fig. 5.3. Here, surface pits several 10 s of nm across are readily apparent at 943 and 1123 K, but are not visible on the surface of the ~843–903 K sample. The minimum temperature for surface pitting appears to be the same as that for nano-bubble agglomeration, suggesting that the two phenomena are closely related. Other work into the effect of nano-bubble growth in copper exposed to He ion irradiation suggests that a small population of very large nano-bubbles form during post-irradiation annealing [14], which are likely to migrate to the surface as a consequence of the temperature gradient (and consequent vacancy concentration gradient) between the bulk and the surface [15].

The difference in scale between the nano-bubbles measured by GISAXS and the surface pits supports the coalescence-driven growth mechanism modelled in [14], where large nano-bubbles constitute only a small minority of all bubbles. Quantitative comparisons between this work and precedent models (such as [1]) is difficult as models of He nano-bubble coalescence typically only model the behaviour of randomly distributed nano-bubbles during annealing. This is in stark contrast to the experimental case where nano-bubbles are in a continuous dynamic process of nucleation, migration and coalescence, which one would expect should feature a larger population of smaller nano-bubbles which have recently nucleated.

The PISCES-A exposed samples show a similar qualitative behaviour with increasing nano-bubble size as one moves above the threshold for growth via coalescence (Fig. 5.2), demonstrating similar behaviour for these samples. One notable difference, however, is that the nano-bubbles which formed under PISCES-A plasma exposure were much larger below 900 K than those from

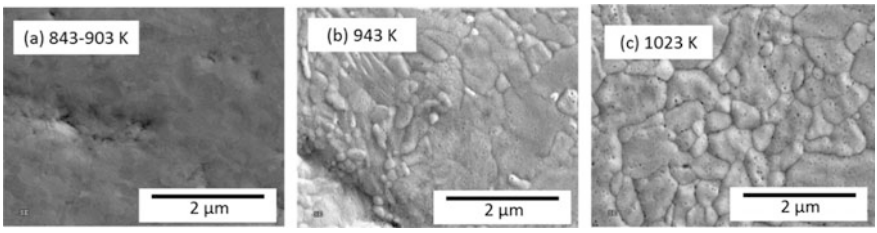

Fig. 5.3 SEM micrographs for W samples exposed to He plasma in NAGDIS-II across a range of temperatures [13]. Surface pitting is readily apparent at temperatures above 943 K (**b–c**), but is not observed for the 843–903 K sample (**a**). Image used with permission

NAGDIS-II. There are many factors which could have contributed to these differences, including differences in the W material prior to plasma exposure, plasma fluence, plasma flux and total exposure time, and the fraction of He which is retained in each experiment. Furthermore, due to the large errors for the 973 K PISCES-A sample, once cannot say definitively whether these bubbles were any larger than the 943 K NAGDIS-II samples. Understanding these differences will be essential in order to develop a clear understanding of which factors are most important for nano-bubble formation and growth, and importantly, why. This is a question which will be pursued in future work.

5.3.2 *Effect of Transient Thermal Loads*

Scattering patterns for samples which had been exposed to ELMy discharges in DIII-D were difficult to fit using a single nano-bubble distribution function alone, indicating that there are distinct qualitative differences in nano-bubble, as shown in Fig. 5.4.

For this reason, a more complex nano-bubble size distribution model was used which consisted of a superposition of an exponential distribution, and a log-normal distribution, given by:

$$P(x) = \frac{r}{\mu_1} e^{-\frac{x}{\mu_1}} + \frac{1-r}{x\sigma\sqrt{2\pi}} e^{-\frac{(\ln x - \ln \mu_2)^2}{2\sigma^2}} \tag{5.1}$$

Here, μ_1 is the median of the exponential component of the distribution, μ_2 is the median of the log-normal component of the distribution, σ is the scaling parameter of the log-normal component, and r is the fraction of exponentially distributed

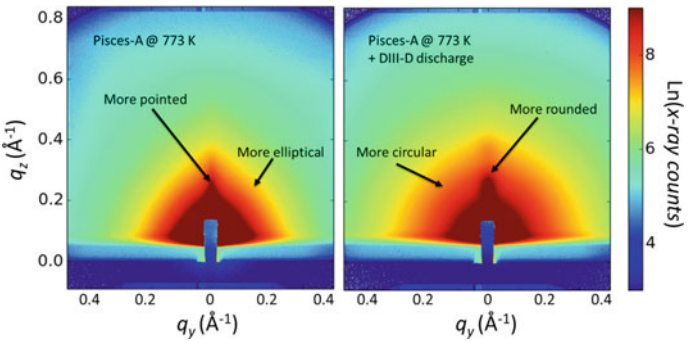

Fig. 5.4 Colour maps of the scattering patterns highlighting qualitative differences between samples exposed to PISCES-A alone and the combination of PISCES-A and DIII-D are shown. In general, DIII-D exposed samples show more circular nano-bubble formation, and the central streak appears more rounded than PISCES-A exposure alone

nano-bubbles. Aspect ratios for the height in the z-direction and cross-sectional diameter in the x-y plane were also fitted for each, and are denoted ϵ_1 and ϵ_2 for the exponentially and log-normally distributed components, respectively.

The addition of the log-normal contribution in Eq. 5.1 significantly increases the complexity of the fit. For a simple exponential fit, there are 5 parameters which must be optimised. For the combination of exponential and log-normal components, this increases to 9. This raises a number of challenges. For instance, the fitting algorithm is more likely to become trapped in a false minimum. Computational time also increases substantially, making troubleshooting the fit prohibitively time-consuming. Instead, fitting was performed for a single pattern taken at 1.0° for each sample. This angle was chosen as the contribution from background scattering drops with increasing incidence angle. As patterns from only a single angle was being fitted, fitting depth distributions was not attempted.

Table 5.1 shows the fitted parameters for the combined exponential and log-normal distribution functions. The fitting parameters of the exponential and log-normal distributions are likely to be highly correlated, so one should be careful about comparing the distribution parameters quantitatively. A more robust approach is to compare the nano-bubble distributions graphically, as is shown in Fig. 5.5. Scattering intensity for GISAXS scales with the volume of the particle. Consequently, while small (<0.5 nm) bubbles appear to be more numerous than larger bubbles, their contribution to the scattering and fit optimisation is negligible.

Table 5.1 Fitted values for samples exposed to He plasma in ELMy discharges in DIII-D. Measurements were taken from two separate visits to the Australian Synchrotron, using different GISAXS camera lengths of 964 mm and 1056 mm, respectively. The 1056 mm camera length samples are indicated by an "*". Please see Eq. 5.1 for a description of the parameters

Sample	r (fraction)	μ_1 (nm)	ϵ_1 (ratio)	μ_2 (nm)	*FWHM* (nm)	ϵ_2 (ratio)
773 K PISCES-A	1	0.73	0.79	–	–	–
773 K PISCES-A + DIII-D (1)	0.32	0.54	0.74	0.17	0.67	1.16
773 K PISCES-A + DIII-D (2) *	0.41	0.85	0.77	0.12	0.74	1.02
973 K PISCES-A *	1	0.83	0.84	–	–	–
973 K PISCES-A +DIII-D (1)	0.44	0.63	0.90	0.67	0.68	0.96
973 K PISCES-A + DIII-D (2) *	0.48	0.95	0.86	0.86	0.85	0.94
DIII-D only (1)	0.58	0.69	0.74	0.85	0.98	1.00
DIII-D only (2)	0.66	0.60	0.71	0.91	0.56	1.11
DIII-D only (3)	0.48	0.57	0.77	0.68	0.74	1.03
DIII-D only (4)	0.37	0.63	0.75	0.86	0.79	0.96
DIII-D only (5) *	0.42	1.06	0.80	0.91	0.63	0.71

One should therefore be cautious about trying to extrapolate these distributions to below 0.5 nm as very little scattering is coming from these particles, so one cannot say that they are actually being measured.

For most of the DIII-D exposed samples shown in Fig. 5.5 a significant peak in the distribution function emerges at ~ 1 nm, with roughly similar tails as one moves toward higher nano-bubble diameters. This clustering of nano-bubble sizes about ~ 1 nm is evidence of a significant change in the nature of nano-bubble formation. Plasma loading differs significantly during transient events such as ELMs compared with the steady plasma fluxes which can be achieved in linear plasma devices. During the ELM, a large amount of He is implanted into the walls while the W surface is heated rapidly. The combination of the large amount of injected He and rapid quenching following the ELM would then result in rapid He precipitation into nano-bubbles. Due to the rapid, transient nature of this effect, it seems reasonable that nano-bubbles should be small and relatively uniform in size, unlike those which are able to form more slowly via diffusion, trapping and agglomeration. Further to this, the height/width ratios of the log-normally distributed nano-bubbles (ϵ_2) are very close to 1 for most of these measurements. This indicates that the anisotropy introduced by the sample surface is less relevant for this mechanism of bubble production.

Interestingly, the samples exposed to He plasma in PISCES-A at 773 K prior to a DIII-D discharge show very different behaviour to other samples. The log-normal component of the distribution produced a sharp peak below 0.1 nm, and no ~ 1 nm peak is present. Due to the weak scattering expected below ~ 0.5 nm this region of the probability density function can be safely dismissed as an erroneous extrapolation of the fitted parameters. Above 0.5 nm the distribution appears to decay more slowly than the exponential fits used for PISCES-A exposures alone, with much heavier tails extending to higher diameters. One possible explanation is that the He nano-bubble density was already saturated prior to exposure to DIII-D. Thus, after

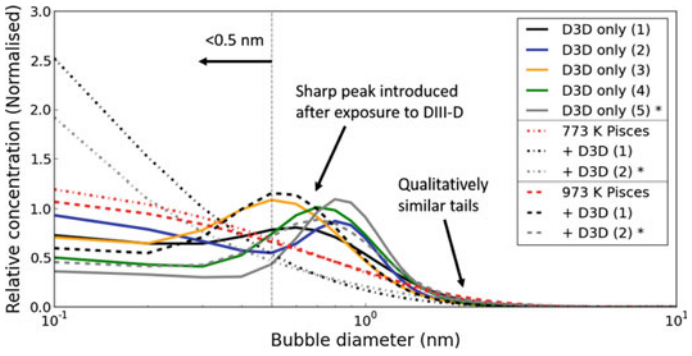

Fig. 5.5 Nano-bubble diameter distributions for nano-bubbles exposed to an ELMy discharge in DIII-D. Most samples exposed to DIII-D feature a strong peak between 0.5 and 1.5 nm, likely the consequence of rapid nano-bubble formation during ELM events. This feature is not observed in samples pre-exposed to He plasma in PISCES-A at 773 K

the rapid influx of He and sharp temperature spike of the ELMs the surplus would have nowhere to go except within existing nano-bubbles.

This behaviour is not observed for samples pre-exposed to PISCES-A at 973 K, which behave in a similar manner to samples without pre-exposure. However, nano-bubble growth is known to be very different at 973 K, with a lower density of larger nano-bubbles forming under these conditions. Consequently, nano-bubble densities may not be saturated after exposure in PISCES-A, allowing new nano-bubbles to precipitate during DIII-D ELMs.

5.4 Summary

The effects of temperature and transient heat and particle fluxes have on He nano-bubble formation in W were studied using NAGDIS-II, PISCES-A, and DIII-D. For W exposed to He plasma in NAGDIS-II at 873 K nano-bubble size distributions exponentially distributed with $\mu \approx 0.5$ nm, similar to those found for the MAGPIE plasma device at the much lower temperature of 473 K. Above $\sim$900 K nano-bubbles followed an approximately exponential distribution with $\mu > 0.65$ nm demonstrating a significant increase in nano-bubble sizes at higher temperatures. Results from PISCES-A show a similar trend, though nano-bubble diameters measured were somewhat larger than was the case for NAGDIS-II.

During transient heat and particle fluxes, such as those produced during ELMs, nano-bubble formation is likely to occur via very different mechanisms than is the case for steady plasma fluxes. GISAXS fitting required a more complex distribution function consisting of a superposition of exponential and log-normal probability density functions. In most W samples exposed to an ELMy He plasma in the DIII-D tokamak a distinct peak for nano-bubble diameters around $\sim$1 nm was observed, indicating the formation of a sub-population of relatively uniformly sized nano-bubbles. This is most likely a consequence of the short-lived high He concentrations and temperature spikes which follow ELM events, with the tight clustering of nano-bubble sizes being a product of their rapid formation.

Samples which had been pre-exposed to He plasma in PISCES-A at 773 K did not have an enhanced population of nano-bubbles around $\sim$1 nm. This may be attributed to the fact that the nano-bubble concentration after exposure in PISCES-A is expected to be saturated, which may inhibit the formation of new bubbles during ELMs. Instead, nano-bubbles would need to grow via other mechanisms, which could explain the heavy-tailed distribution observed in this case.

This work is the first experimental demonstration of the significant differences in nano-bubble formation behaviour which can be expected during transient events. This is a topic which is highly relevant for the ITER project, as work on linear devices will need to be extrapolated to the much more complex tokamak environment. This result is an excellent demonstration of the power of GISAXS to probe material changes which are almost inaccessible by other techniques.

References

1. S. Sharafat, A. Takahashi, Q. Hu, N.M. Ghoniem, A description of bubble growth and gas release of helium implanted tungsten. J. Nucl. Mater. **386–388**, 900–903 (2009)
2. M. Miyamoto, S. Mikami, H. Nagashima, N. Iijima, D. Nishijima, R.P. Doerner, N. Yoshida, H. Watanabe, Y. Ueda, A. Sagara, Systematic investigation of the formation behavior of helium bubbles in tungsten. J. Nucl. Mater. **463**, 333–336 (2015). https://doi.org/10.1016/j.jnucmat.2014.10.098
3. S. Bardin, T.W. Morgan, X. Glad, R.A. Pitts, G. De Temmerman, Evolution of transiently melt damaged tungsten under ITER-relevant divertor plasma heat loading. J. Nucl. Mater. **463**, 193–197 (2015). https://doi.org/10.1016/j.jnucmat.2014.10.046
4. G. Sergienko, B. Bazylev, T. Hirai, A. Huber, A. Kreter, P. Mertens, A. Nedospasov, V. Philipps, A. Pospieszczyk, M. Rubel, U. Samm, B. Schweer, P. Sundelin, M. Tokar, E. Wessel, Experience with bulk tungsten test-limiters under high heat loads: melting and melt layer propagation. Phys. Scr. T. **128**, 81–86 (2007). https://doi.org/10.1088/0031-8949/2007/T128/016
5. O. El-Atwani, K. Hattar, J.A. Hinks, G. Greaves, S.S. Harilal, A. Hassanein, Helium bubble formation in ultrafine and nanocrystalline tungsten under different extreme conditions. J. Nucl. Mater. **458**, 216–223 (2015). https://doi.org/10.1016/j.jnucmat.2014.12.095
6. N. Ohno, D. Nishijima, S. Takamura, Y. Uesugi, M. Motoyama, N. Hattori, H. Arakawa, N. Ezumi, S. Krasheninnikov, A. Pigarov, U. Wenzel, Static and dynamic behaviour of plasma detachment in the divertor simulator experiment NAGDIS-II. Nucl. Fusion **41**, 1055–1065 (2001). https://doi.org/10.1088/0029-5515/41/8/309
7. D.U.B. Aussems, D. Nishijima, C. Brandt, R.P. Doerner, N.J.L. Cardozo, Spectroscopic characterization and imaging of laser- and unipolar arc-induced plasmas. J. Appl. Phys. **116**, 63301 (2014). https://doi.org/10.1063/1.4892675
8. J.L. Luxon, A brief introduction to the DIII-D tokamak. Fusion Sci. Technol. **48**, 828–833 (2005)
9. M.W. Maisel, T. Ohkawa, K.H. Burrell, R.L. Freeman, F.J. Helton, T.H. Jensen, R.J. La Haye, D.O. Overskei, R. Prater, J.M. Rawls, T. Tamano, The fusion power research programme at GA Technologies Inc. Nucl. Fusion **25**, 1113–1125 (1985). https://doi.org/10.1088/0029-5515/25/9/022
10. J.L. Luxon, A design retrospective of the DIII-D tokamak. Nucl. Fusion **42**, 614–633 (2002). https://doi.org/10.1088/0029-5515/42/5/313
11. C.P.C. Wong, D.L. Rudakov, J.P. Allain, R.J. Bastasz, N.H. Brooks, J.N. Brooks, R. P. Doerner, T.E. Evans, A. Hassanein, W. Jacob, K. Krieger, A. Litnovsky, A.G. McLean, V. Philipps, A.Y. Pigarov, W.R. Wampler, J.G. Watkins, W.P. West, J. Whaley, P. Wienhold, Divertor and midplane materials evaluation system in DIII-D. J. Nucl. Mater. **363–365**, 276–281 (2007). https://doi.org/10.1016/j.jnucmat.2007.01.121
12. R.P. Doerner, D.L. Rudakov, C.P. Chrobak, A.R. Briesemeister, C. Corr, G. De Temmerman, P. Kluth, C.J. Lasnier, A.G. McLean, D.C. Pace, R.A. Pitts, O. Schmitz, M. Thompson, V. Winters, Investigation of He–W interactions using DiMES on DIII-D. Phys. Scr. **T167**, 14054 (2016). https://doi.org/10.1088/0031-8949/T167/1/014054
13. M. Thompson, R. Doerner, N. Ohno, N. Kirby, P. Kluth, D. Riley, C. Corr, Measuring temperature effects on nano-bubble growth in tungsten with grazing incidence small angle X-ray scattering. Nucl. Mater. Energy. (2017). https://doi.org/10.1016/j.nme.2016.11.025
14. J. Evans, R. Escobar Galindo, A. van Veen, A description of bubble growth and gas release during thermal annealing of helium implanted copper. Nucl. Instrum. Meth. Phys. Res. Sect. B Beam Interact. Mater. Atom **217**, 276–280 (2004). https://doi.org/10.1016/j.nimb.2003.10.013
15. J.H. Evans, A. van Veen, Gas release processes for high concentrations of helium bubbles in metals. J. Nucl. Mater. **233–237**, 1179–1183 (1996). https://doi.org/10.1016/S0022-3115(96)00119-5

Chapter 6
Investigating Synergistic Effects on W Performance with Magnum-PSI

6.1 Synergy

Linear plasma devices are useful in fusion material studies as they allow experimenters a much greater degree of control over the plasma conditions and sample heating than is possible in a large scale fusion experiment such as ITER, allowing one to perform controlled experiments to determine how different factors influence material performance. Many factors are known to influence material performance, including sample surface temperature [1–4], hydrogen [5–12], helium [13–26], plasma impurities [27–32], material morphology [33, 34] and composition [35], radiation damage [4, 36–43], sputtering [44], and thermal shocks [45, 46]. In large fusion devices experimental campaigns typically run for months at a time, and involve hundreds or thousands of discharges where successive discharges can vary significantly from each other. This makes identifying the role of individual factors very challenging using data from these machines alone.

Linear devices fill the gap by permitting systematic studies of individual factors, and have done much to advance the current understanding of tungsten behaviour under plasma exposure. However, the ultimate goal of fusion materials research is to understand how candidate armour materials will behave in a full-scale fusion device, such as ITER or a future DEMO reactor. And this understanding must be complete enough to be able to predict the material performance over the full life of the device. It is not enough to study the relevant factors which lead to tungsten degradation individually: understanding the synergies between these factors is essential.

Perhaps the most widely studied synergy in tungsten is the simultaneous effects of hydrogen and helium on microstructure formation and hydrogen retention. As ITER is a licenced nuclear facility, it will need to abide by strict limits on the accumulation of in-vessel radioactive materials. The tritium limit for the entire reactor is 1 kg [47]. Should this be exceeded, the reactor will no longer be able to operate. Thus, minimisation of H retention is essential.

M. Thompson, *Helium Nano-bubble Formation in Tungsten*, Springer Theses,
https://doi.org/10.1007/978-3-319-96011-1_6

For W exposed to pure H plasma at lower temperatures (473 ~ 723 K) H has a tendency to cluster around grain boundaries which ultimately leads to the formation of surface blisters [48]. However, even the addition of a 0.1% He into the plasma has been found to significantly reduce the occurrence of these blisters. In a similar study, Miyamoto et al. [49] also found that H retention is reduced in these mixed plasmas, attributing this reduction in retention and blister formation to the formation of He nano-bubbles which are believed to act as a diffusion barrier. Blisters formation was also found to be sensitive to the crystalline orientation of the crystal grains in which they form. On the other hand, Lee et al. [50] found that He retention is not affected by the presence of H.

This phenomenon becomes much more complicated once temperature is factored into it, as the behaviour of both H and He vary independently at different temperatures. In He pre-irradiated samples, Nishijima et al. [51] found that the temperature of He pre-exposure had a dramatic effect on subsequent D retention after pure D plasma exposure at 550 K. For high temperature (1600 K) pre-exposure, where much larger nano-structures form, D retention was significantly enhanced, while lower temperature (700 K) pre-exposure reduced D retention by a factor of 5.

Complex synergistic effects have also been observed for studies probing the combined effects of radiation damage, H plasma, and temperature. For instance, Wampler and Doerner [52] found that radiation damage has little effect on H retention at 314 K, but significantly enhanced retention from 473 to 773 K. Plasma flux also has a significant effect on H retention [3, 34]. For lower H fluxes, H retention is expected to decrease substantially above ~700 K. However, for H fluxes above 10^{23}D/m^3 retention was stable up to 860 K.

6.2 Experimental Methods

6.2.1 Sample Preparation

Polycrystalline tungsten samples (10 mm × 10 mm × 2 mm) were cut from a single large block of 99.97% purity tungsten, sourced from PLANSEE, and polished to a mirror finish.

To simulate the effects of collision cascades and transmutation from neutron irradiation that will occur during operation, ten samples were irradiated with 2 meV W^{2+} ions to a fluence of 10^{19} ions/m^2 at the 1.7 MV tandem ion accelerator at the Australian National University. To account for chemical changes which are expected under neutron irradiation a further ten samples were irradiated with 2 meV Re^{2+} ions to a fluence of 10^{19} ions/m^2. Irradiations were performed at room temperature by rastering the beam across the sample surface. Both of these implantations produced damage profiles with peak damage levels of approximately 5.2 displacements per atom (dpa) at a depth of 80 nm calculated using the Kinchin-Pease method with SRIM [53]. A further ten samples were left undamaged for comparison.

6.2.2 Plasma Exposure in Magnum-PSI

After ion irradiation, samples were taken to the linear plasma device Magnum-PSI at the Dutch Institute For Fundamental Energy Research (DIFFER) [54], where they were exposed to plasmas under a wide range of conditions. The plasma fluxes available in Magnum-PSI (10^{23}–10^{24} ions/m^2/s) are comparable to the steady-state plasma fluxes expected in ITER's divertor during burning plasma operation. Truly producing an ITER-like environment is difficult, however, as ITER will operate for several years, resulting in plasma fluences that are not viable to reproduce experimentally. Further, plasma instabilities are the norm in tokamaks, so periodic episodes of very high heat and particle fluxes are expected in ITER. No attempt has been made to reproduce those here. While reproducing a true ITER-like environment is difficult, experiments of this nature provide valuable insights into the mechanisms that drive nano-structural development, H and He retention, which are essential for modelling efforts to qualify the engineering tolerances of the reactor lining materials.

The samples were maintained at floating potential and were exposed to each permutation of surface temperature variation (<700 K and >1000 K), plasma feed gas composition (100% H, 5% He/95% H, 20% He/80% H, 50% He/50% H, 100% He), and ion irradiation treatment (W irradiated, Re irradiated, and non-irradiated) to produce a broad range of conditions in order to determine the key mechanisms which drive He retention, as outlined in Fig. 6.1. Samples were exposed to a fluence of $2 \times 10^{25}\mathrm{ions/m^2}$. An additional low fluence sample set ($1 \times 10^{24}\mathrm{ions/m^2}$) was also generated to gauge the effect of plasma fluence. Flow rates were used to determine feed gas composition. Preliminary quadrupole mass spectroscopy measurements have been performed, revealing actual ionic ratios much lower than those of the feed gas for the mixed plasmas. Ionic helium concentrations are 2% He, 8% He, and 23% He for the 5% He, 20% He and 50% He feed gas ratios, respectively. Throughout this chapter the ionic ratios are reported.

2D temperature maps of the sample surface were measured using a FLIR A645 sc infra-red camera, and checked against a near-centre point measurement with an FMPI SpectroPyrometer to ensure consistency. Due to the plasma profile, sample surface temperatures were not uniform during plasma exposure, tending to be hotter in the centre and cooler towards the edges of the sample. This discrepancy was most significant for higher sample temperatures, where the difference could be up to 200–300 K. For consistency, all temperature measurements reported here refer to the value taken at the sample centre. Electron temperatures and densities were measured via Thomson scattering $\sim$25 mm in front of the target by performing 30 measurements over a 3 s period to minimise random errors [55]. The range of values for electron temperature and electron density are shown in Fig. 6.2. Exposure times for each sample were varied to ensure consistent fluence.

Due to the way Magnum-PSI is presently configured, plasma exposure occurred by firing a series of short plasma pulses at the target samples, followed by a pause of up to 30 min to allow the magnets to cool down to acceptable temperatures

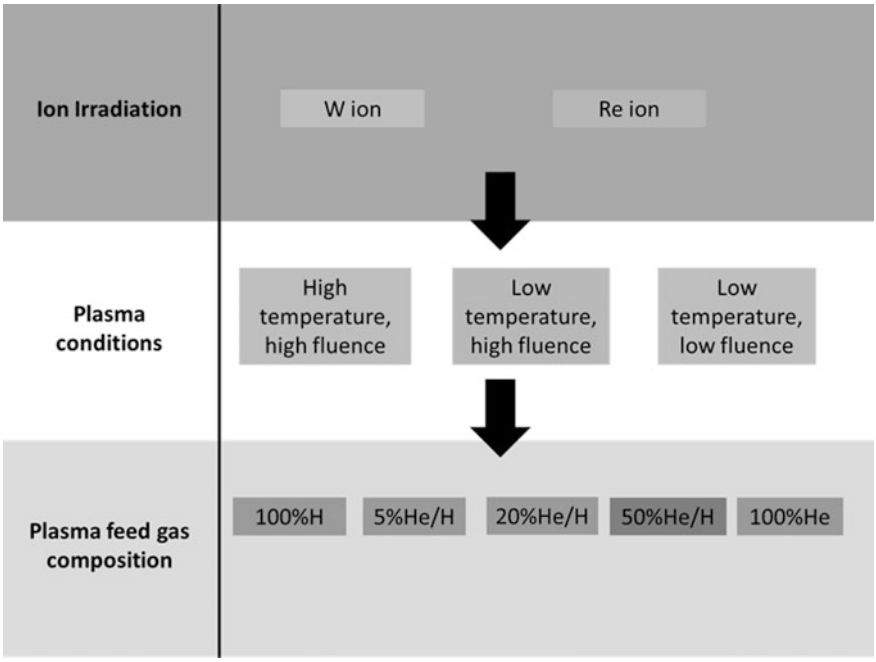

Fig. 6.1 Schematic of the sample preparation method for the Magnum-PSI experiment. Samples were created for each permutation of ion-irradiation treatment (orange), plasma condition (white), and plasma feed gas composition (blue)

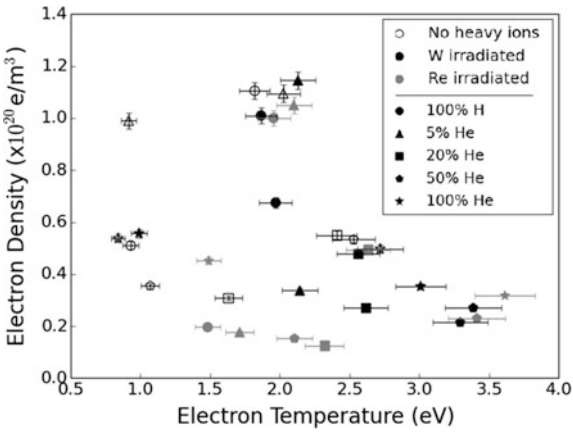

Fig. 6.2 The electron densities (n_e) and electron temperatures (T_e) of each plasma shot are shown [56]. Open shapes refer to samples which had not been pre-irradiated with heavy ions, solid black shapes 2 meV W ion pre-irradiated, and solid red shapes 2 meV Re ion irradiated. Measurements were taken via Thomson scattering for the beam centre $\sim$25 mm in front of the target. Image used with permission

before the next pulse. The samples were actively cooled, so while temperatures could become quite high during a plasma pulse, they promptly fell to room temperature once the pulse stopped. H/He diffusion between plasma pulses is therefore not considered to be significant.

Changing the plasma composition had a dramatic effect on other properties of the plasma, such as the flux and sample heating. Compromise between these parameters was therefore essential, so plasmas were chosen to minimise differences between temperature and total fluences, as these are believed to be the most significant factors. However, it is worth being mindful of the fact that other properties such as the electron temperature and density, flux, pulse length, and total exposure time varied from sample to sample. Indeed, despite efforts to maintain consistency, even the temperature varied considerably between samples. Note, however, that all plasma parameters were reasonably consistent between shots fired at the same sample; differences occur primarily between different samples.

6.2.3 ERDA Measurements

C-ion elastic recoil detection analysis (ERDA) was performed on each of the samples on the STAR accelerator at the Australian Nuclear Science and Technology Organisation. ERDA measurements were performed on two different occasions, with different ion conditions. In the first round of measurements, 10 meV C-ion beam was used on 4 sets of samples to measure the retention of both H and He within the first 100 nm of the surface, using a 6 μm Kapton foil in front of the detector to block unwanted backscattered C ions. C ions were used so that both H and He could be measured simultaneously, as only target atoms lighter than the incident beam can be backscattered.

In the second measurement round, an 8.7 meV C^{4+} beam of ions was incident at an angle of 75°, and a silicon surface barrier detector was located at a scattering angle of 30°, with a 9 μm Mylar stopping foil. In both measurement rounds the He and H signals occurred in distinct regions of the spectrum, enabling straightforward analysis. The adjustment in conditions in the second round was made to increase the He count rate, which was very low for the first measurement round. The full helium peak could also clearly be resolved, indicating that the maximum depth of the analysis exceeded the maximum depth at which helium was retained. Helium retention is expected to occur mostly within the first 100 nm or so from the sample surface [57]. Cross sections for quantification were obtained via the methods outlined in [58]. Data analysis was performed using the SIMNRA software [59].

Defining the He profile deeper into the material is very difficult as the count rate is low for the concentrations expected in all measurements. For this reason, the focus has been on determining the total He retention rather than where this He is located. Extracting information on H retention is more difficult. As the H component of the plasma was ^{1}H, the H which originated from the plasma could not be easily distinguished from H contamination from surface condensation or other sources. A reference sample was thus taken to measure the baseline H signal, and the sharp surface peak has been largely disregarded.

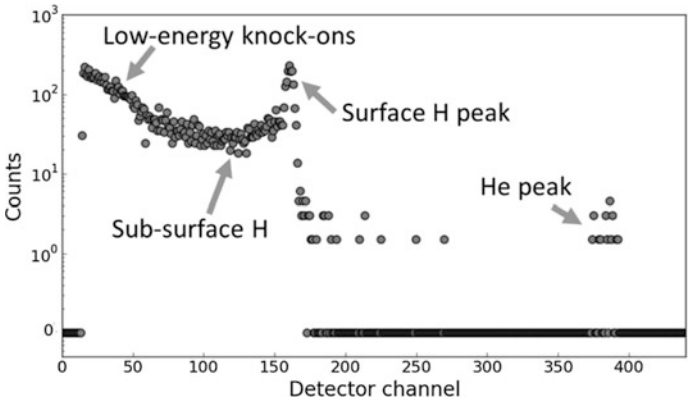

Fig. 6.3 Results from a typical ERDA measurement are shown. Several distinct features are present (from left): a low-energy peak resulting from knocked-on H atoms from the Kapton film shielding the detector, a "plateau" caused by sub-surface H atoms, a sharp peak resulting from surface adsorption of H, and a small high-energy peak from retained He. Only the sub-surface H and He peak are of interest to analysis

Another artefact in the data is also present in the form of an ever increasing peak towards low energies, which is likely to originate from high-energy C ions being backscattered from the W lattice, and impacting with H within the Kapton foil, leading to low-energy knock-ions. Fitting was focussed on a narrow and relatively flat region between the surface peak and low-energy background, where H counts should originate predominantly from sub-surface H retention. H retention from the reference sample in this region was $\sim$0.2 at.% (compared with >1 at.% for most other samples), indicating that the background signal in this region is significantly smaller than other potential sources of error. Data from a typical ERDA measurement is shown in Fig. 6.3, highlighting the main features in the data.

6.3 Results

6.3.1 He Retention

Figure 6.4 shows the ERDA He retention measurements for each sample, for both high (>1000 K) and low (<700 K) sample surface temperatures. He retention is found to be greater at higher surface temperatures and the He retention increases with increasing He content. However, it does not increase linearly. At lower surface temperatures, the He retention remains fairly constant for the conditions studied here.

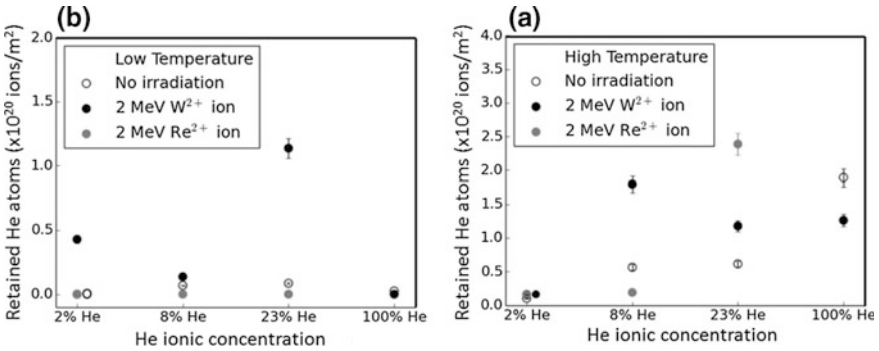

Fig. 6.4 He retention in tungsten measured by ERDA at various H/He plasma ratios for temperatures **a** >1000 K and **b** <700 K

The variation in electron temperature enables the total ion energy, E_i, to be calculated from the sheath potential, Φ_s, by [60]:

$$E_i = \Phi_s \times e + 2k_B T_i \tag{6.1}$$

$$\Phi_s = -0.5 k_B T_e \ln\left(\frac{2\pi m_e}{m_i}\frac{(1+T_i/T_e)}{(1-\delta)^2}\right) \tag{6.2}$$

where e is the elementary charge, m_e is the electron mass, m_i is the ion mass, k_B is Boltzmann's constant, T_e is the electron temperature, T_i is the ion temperature, and δ is the secondary electron yield due to ion or electron collisions with the surface. In Magnum-PSI electrons and ions are in thermal equilibrium in the source and are expected to remain so upon reaching the target, so T_e and T_i are assumed to be equal. To calculate the ion energies, δ was assumed to be negligible, and m_i to be the weighted average of the hydrogen and helium atomic masses for a given plasma composition.

Figure 6.5 displays the He retention dependence on the ion impact energy, as calculated from Eq. (6.2). Here, a clear minimum ion implantation energy appears to be required in order to enable He ion retention. He retention was approximated as a piecewise linear function of the form:

$$f(E) = \begin{cases} 0, & E < E_T \\ m(E - E_{\mathrm{He}}), & E \geq E_T \end{cases} \tag{6.3}$$

Here, E is the He ion energy, E_T is the minimum threshold energy required for He retention, and m is a linear gradient used to approximate He retention for He ion energies beyond the threshold energy. E_T was calculated by fitting both E_T and m to the data using a least-squares fitting algorithm, giving an estimated He retention threshold energy of 9.0 ± 1.4 eV. Errors were estimated by applying the jackknife

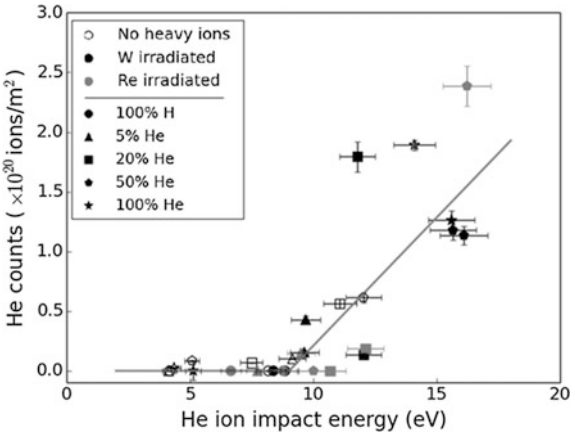

Fig. 6.5 The effect of He ion impact energy on He retention is shown, revealing a minimum impact energy of 9.0 ± 1.4 eV in order for retention to occur [56]. Above this value, He retention increases sharply. This effect is not strongly influenced by ion irradiation treatment or sample temperature. A solid line has been drawn to guide the eye. Image used with permission

method, as described in [61]. Further uncertainty is introduced by the fact that the H in the plasma is likely composed of some mix of H^+, H_2^+, and H_3^+, rather than the pure H^+ assumed for this work. If H_2^+ were the dominant species, for instance, the He threshold energy would be closer to 9.4 ± 0.7 eV.

This minimum energy is unaffected by pre-irradiation with both W and Re, which both show similar behaviour to the samples which were not pre-irradiated with heavy ions. Furthermore, this minimum energy appears unaffected by sample surface temperature and plasma H/He ratios. This result expands significantly on the findings of Nishijima et al. [13], who observed pitting and bubble formation in tungsten at 1600 K at and above 5 eV, but not at lower He ion energies. During their experiments, Nishijima et al. noted fluctuations in the plasma potential could vary by ± 4 eV over the course of a plasma exposure, meaning at a nominal ion energy of 5 eV He ion energies could have reached energies as high as 9 eV. This places both the present work and that of Nishijima et al. well within the range of uncertainty for both experiments. The present work also demonstrates that the effect is much more fundamental than a change in surface behaviour and is caused directly by the inability of He to be retained at low ion impact energies.

Molecular dynamics simulations by Borovikov et al. [62] predicted similar behaviour, with total He reflection occurring at impact energies up to 10 eV and increasing retention with energy above 20 eV (no data were presented between 10 and 20 eV). The present study is in excellent qualitative agreement with Borovikov et al., reproducing two of the key findings: zero retention below some minimum ion impact energy, and increasing retention with increasing ion energy beyond this threshold. This trend is observed regardless of the ion implantation treatment or plasma composition for each sample.

6.3.2 He Nano-bubble Formation

The presence of an energy threshold has important implications for the formation of helium-induced nano-bubbles in tungsten. GISAXS was performed to determine the nature of any potential nano-bubble formation. A GISAXS model was then fitted to the data, where nano-bubbles are assumed to be spheroidal in shape, and have an exponential diameter distribution. Both the mean bubble diameter in the x-y plane and their full height along the z-axis were fitted. The spheroids were orientated such that their axis of rotational symmetry was aligned with the z-axis. Here, the sample surface is in the x-y plane, while the z-direction is normal to the sample surface.

A summary of the results of the GISAXS analysis are presented in Table 6.1, while examples of the corresponding GISAXS patterns used for this analysis are presented in Fig. 6.6. Helium nano-bubble formation was observed in all samples where the helium retention measured by ERDA exceeded 5×10^{19}He atoms/m^2 and was absent for all samples with lower retention values. For samples which were not pre-irradiated, the mean nano-bubble size were similar, ranging from 0.76 to 0.82 nm.

Bubbles were observed to grow more spherical with increasing helium concentration, but there was no such correlation with their diameters. This result suggests that as retention increases, additional He retention occurs through an increased concentration of bubbles, or an increased pressure within each bubble, rather than by an increase in bubble size.

Nano-bubbles which formed in ion-irradiated tungsten with similar levels of He retention resulted in the formation of somewhat smaller bubbles, though the differences were comparable to approximately twice the error range of the measurements. For this sample, the IR camera's temperature measurement was saturated, indicating a much higher surface temperature above 1600 K. This result of smaller bubbles forming at higher temperatures contradicts previous direct observation and modelling, which indicated larger bubble growth at higher temperatures [17, 63].

Table 6.1 Nano-bubble diameter distributions measured by GISAXS

Plasma He fraction (%)	Ion treatment	Retained He atoms (x10^{20}/m^2)	Surface temperature (K)	He ion energy (eV)	Mean diameter (x-y plane, nm)	Aspect ratio (z/y)
0	–	–	1000–1300	8.2±0.5	–	–
2	–	0.10±0.01	1000–1300	9.2±0.6	–	–
8	–	0.56±0.04	1000–1300	11.4±0.7	0.76±0.01	0.77±0.01
23	–	0.61±0.04	1000–1300	12.5±0.8	0.82±0.08	0.81±0.01
100	–	1.9±0.1	1100–1400	14.1±0.8	0.76±0.04	0.89±0.01
100	2 meV W	1.3±0.1	>1600	15.6±0.9	0.68±0.05	0.90±0.01
100	–	0.025±0.001	423–473	4.4±0.4	–	–

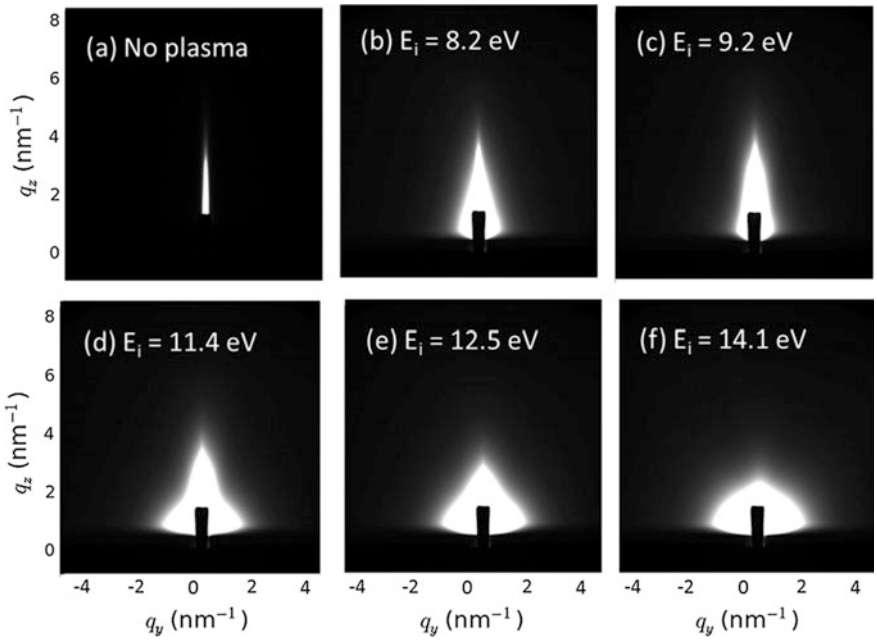

Fig. 6.6 Grazing-incidence small angle X-ray scattering (GISAXS) patterns of samples exposed to mixed H/He plasma GISAXS patterns are shown for non-irradiated samples with surface temperatures above 1000 K for **a** undamaged tungsten, **b** 100% H, **c** 5% He, **d** 20% He, **e** 50% He, and **f** 100% He [56]. When E_i exceeds the threshold energy of 9.0 ± 1.4 eV a circular component emerges in the pattern which corresponds to the formation of He nano-bubbles. Axes show the reciprocal space coordinates for each measurement. Image used with permission

However, these studies dealt with systems which had not been ion-irradiated before plasma exposure. Thus, this discrepancy may be the result of additional bubble nucleation sites being available in ion-damaged samples as a consequence of additional vacancy sites being created during ion implantation. This could result in helium being distributed between larger numbers of smaller bubbles. Further study will be required to verify whether this difference is a real effect, or the product of measurement uncertainty.

6.3.3 H Retention

Figure 6.7 shows H retention measurements integrated over the first 40 nm for tungsten with both low (<700 K) and high (>1000 K) surface temperatures. At lower temperatures, ion irradiation, shown as the solid shapes, leads to a strong increase in H retention and becomes less significant with increasing He feed gas concentration. At higher temperatures, on the other hand, retention appears not to

be strongly affected by the plasma composition. W and Re ion-irradiated samples also show similar trends, indicating that retention is not strongly influenced by the presence of Re.

Temperature is known to have a significant effect on the retention of H in W, so even small changes in surface temperatures between shots could have important implications for the interpretation of these results. To allow for variations in the sample temperature while varying the plasma composition, Fig. 6.8 shows the same data as Fig. 6.7 with H retention this time plotted against sample temperature. Ion irradiation seems to significantly increase H retention. On the other hand, the presence of He appears to counteract this effect, bringing retention figures closer to their non-irradiated counterparts. H retention in non-irradiated samples, by contrast, shows no dependence on He at either high or low temperatures. This result is consistent with the near-surface D retention measurements taken by Baldwin et al. [27] in mixed D-He plasma. In Baldwin et al. study, D retention could be measured up to 3 μm below the surface. Although near-surface D retention was similar, Baldwin et al. found that the presence of He lead to a dramatic reduction in D retention beyond ∼100 nm, which was attributed to the formation of a layer of He nano-bubbles that act as an effective diffusion barrier. The effect of He on hydrogenic diffusion in tungsten has been measured explicitly by Lee et al. [64].

The effect of He on H retention can be explained by considering the energetics of H or He binding with ion-induced defect structures. He binds much more strongly to vacancies than H does, to the point where He retention in a mixed H/He plasma is almost indistinguishable from He retention in a pure He plasma [65]. In effect, He retention is not reduced by the presence of H (though the effect of H on He-induced nanostructures is an open question). H, on the other hand, is strongly influenced by He due to He preferentially occupying the available trapping sites. For the non-irradiated samples, very little He retention was observed at lower temperatures.

At higher temperatures, H retention appears to level-off at a concentration of around 1%, with very little variation observed between irradiation and plasma

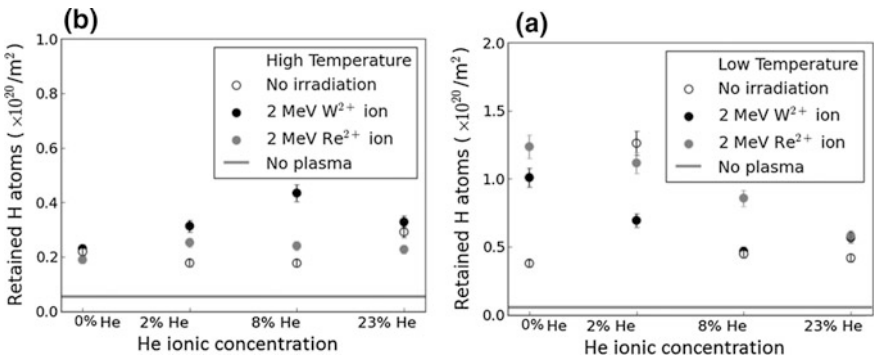

Fig. 6.7 Hydrogen retention plotted against plasma He ionic concentration for sample surface temperatures **a** >1000 K and **b** <700 K

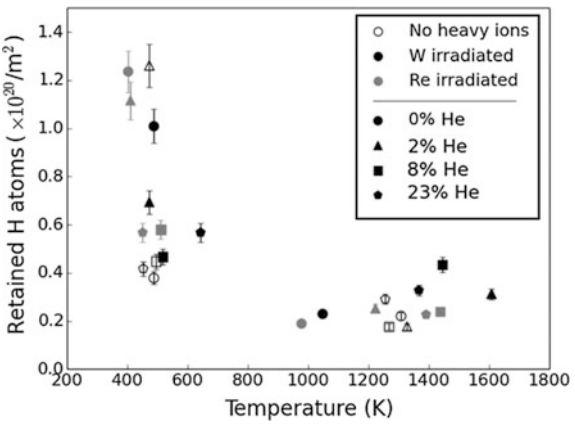

Fig. 6.8 The effects of plasma composition, sample surface temperature, and ion irradiation treatment on H retention are shown simultaneously

conditions. This is consistent with the work of Buzi et al. [3, 34], who found that deuterium retention was relatively insensitive to temperature for high flux plasma ($\sim 10^{24}$ $m^{-2}s^{-1}$). At lower plasma fluxes ($\sim 10^{22}$ $m^{-2}s^{-1}$) retention drops significantly above 800 K. The lack of variation between ion-irradiated and non-irradiated samples is likely to be due to damage annealing above 1000 K.

6.3.4 *H-induced Surface Modification*

To investigate changes to surface morphology, surface imaging was performed on each sample after plasma exposure with a Hitachi 4300SE/N field emission SEM (Fig. 6.9). For the low surface temperature ($\sim$490 K) sample exposed to a pure H plasma without heavy ion irradiation (Fig. 6.9b), extensive blistering was observed on the surface which is consistent with the small blisters observed by Shu [5]. Blister sizes ranged from hundreds of nanometres up to $\sim$1 μm. These form as a result of H-induced local superplasticity where high concentrations of H greatly reduce the formation energy of vacancies [7]. At the temperatures used within the present experiment, diffusion of H into the bulk is limited, so H-induced void and ultimately blister formation occurs near the sample surface, rather than along grain boundaries. Blistering was not observed at higher temperatures, likely due to the higher mobility of H under these conditions [2]. Surface modification from He was not evident from SEM.

With increasing He concentration blister formation appears to decline (Fig. 6.9d). Ueda et al. [48] observed a similar effect, where a plasma concentration with only 0.1% He resulted in a significant reduction in the number of blisters formed, with a total suppression of blisters observed for concentrations higher than 1% He. This phenomenon has been widely reported in the literature [24, 51, 65–67]. For samples pre-exposed to W or Re ion irradiation, no notable surface deformation was observed, even for surface temperatures below 700 K (Fig. 6.9f). Blister

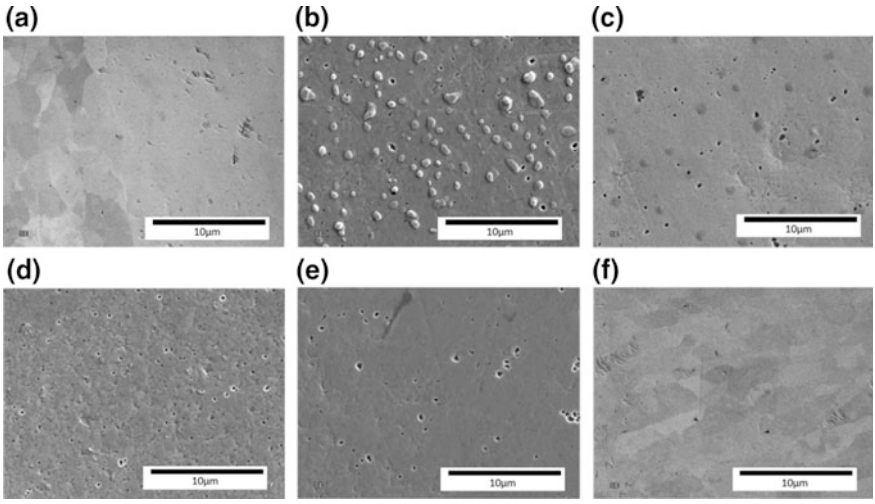

Fig. 6.9 SEM micrographs showing surface morphology changes for **a** virgin W, **b** low temperature H plasma without heavy ion irradiation, **c** low temperature 2% He plasma without heavy ion irradiation, **d** low temperature 23% He plasma without heavy ion irradiation, **e** high temperature H plasma without heavy ion irradiation, and **f** low temperature H plasma with W ion irradiation. Blisters are clearly visible under low temperature exposure in the absence of heavy ion induced damage, but appear to become sparser as He concentration is increased. At higher temperatures, and where pre-irradiation was performed, blisters were not observed. Pitting is observed in all samples, and is the result of sample preparation

suppression has also been observed in similar ion-irradiation studies in the ion-damaged zone [40]. However, cracking was observed below this region along the grain boundaries. For very high plasma flux, H migration may be limited by the rate of inward diffusion from the surface. At lower energies, H first adsorbs on the surface before diffusing inwards [4]. Due to the vacancies in ion-damaged tungsten H becomes trapped and the rate of inward diffusion is limited until all free vacancies are filled. Retention is therefore enhanced. As H atoms are tightly bound they are not free to accumulate together and drive blister formation.

6.4 Conclusions

6.4.1 Summary

Understanding synergies is essential in order to better predict the performance of W based materials in future fusion experiments. Here, a systematic study into the synergistic effects of H/He plasma composition, sample temperature, and radiation damage on H retention, He retention, and microstructural changes in W was described.

The energy of He ions as they impacted on the W surface was found to be the dominant factor influencing He retention, and a clear minimum energy of 9.0 ± 1.4

eV was found to be required for He to be retained assuming all H in the plasma was H^+. For H_2^+ this estimate becomes 9.4 ± 0.7 eV. He retention increased sharply above this energy. This result is in good agreement with earlier modelling work [62], which predicted no He retention below 10 eV. This result also expands significantly on the work of Nishijima et al. [13], who found a minimum He ion energy was required for surface pitting to occur. For high temperature (>1000 K) samples which had not been pre-irradiated with heavy ions, nano-bubbles were observed via GISAXS, which possessed exponential diameter distributions with a mean diameter of $\sim$0.8 nm. Their size was unaffected by both plasma H concentration and He incident ion energy. However, the scattering signal from GISAXS was stronger with greater He retention, indicating an increase in bubble concentration rather than size with increasing He content. Pre-irradiation with heavy ions may reduce nano-bubble sizes, though this will need to be verified by further work.

H retention was strongly influenced by sample temperature, decreasing sharply until $\sim$700 K before plateauing at higher temperatures. This high-temperature plateau may be a consequence of the high plasma flux of Magnum-PSI, as this behaviour is not observed at lower fluxes [3]. Below 700 K, pre-irradiation with heavy ions was found to increase H retention.

6.4.2 *Future Work*

In this study, GISAXS was only performed on a small selection of the samples which were exposed to Magnum-PSI. So, while details such as He retention (measured by ERDA) are known for all samples, details on the He nano-structures are not. Only a single GISAXS measurement was taken for a sample which had been exposed to heavy-ion irradiation, revealing an average bubble diameter which was much smaller than those for non-irradiated samples. This raises an interesting possibility that the presence of ion-induced defects may change the way in which nano-bubbles form, possibly through the introduction of more nucleation sites for nano-bubble growth. However, as only one measurement of ion-irradiated samples was taken, it is not known whether the formation of smaller nano-bubbles is a persistent feature of radiation-damaged materials, or whether some other trend may emerge once a larger parameter space is probed.

Radiation damage could alter the growth dynamics of these bubbles in many ways. Additional vacancy sites could mean more He is trapped in single vacancies or small clusters, leaving less He available for bubble formation. Alternatively, it may simply increase the rate of bubble nucleation, leading to the formation of a larger number of smaller bubbles. Further GISAXS work on ion-damaged materials will be required to determine the nature of any differences in nano-structure formation which occur in radiation-damaged materials.

References

1. J.P. Roszell, J.W. Davis, A.A. Haasz, Temperature dependence of deuterium retention mechanisms in tungsten. J. Nucl. Mater. **429**, 48–54 (2012)
2. R.A. Causey, D.F. Cowgill, R. Doerner, R. Kolasinski, B. Mills, D. Morse, J. Smugeresky, W.R. Wampler, R. Williams, D. Huber, Deuterium retention in tungsten at elevated temperatures. J. Nucl. Mater. **415**, S672–S675 (2011)
3. L. Buzi, G. De Temmerman, B. Unterberg, M. Reinhart, A. Litnovsky, V. Philipps, G. van Oost, S. Möller, Influence of particle flux density and temperature on surface modifications of tungsten and deuterium retention. J. Nucl. Mater. **455**, 316–319 (2014). https://doi.org/10.1016/j.jnucmat.2014.06.059
4. M.H.J. 't Hoen, M. Mayer, A.W. Kleyn, P.A. van Emmichoven, Strongly reduced penetration of atomic deuterium in radiation-damaged tungsten. Phys. Rev. Lett. **111**, 225001 (2013)
5. W.M. Shu, High-dome blisters formed by deuterium-induced local superplasticity. Appl. Phys. Lett. **92**, 211904 (2008)
6. G.M. Wright, A.W. Kleyn, E. Alves, L.C. Alves, N.P. Barradas, G.J. van Rooij, A.J. van Lange, A.E. Shumack, J. Westerhout, R.S. Al, W.A.J. Vijvers, B. de Groot, M.J. van de Pol, H.J. van der Meiden, J. Rapp, N.J. Lopes, Cardozo, Hydrogenic retention in tunsten exposed to ITER divertor relevant plasma flux densities. J. Nucl. Mater. **390–391**, 610–613 (2009)
7. S.C.C. Middleburgh, R.E.E. Voskoboinikov, M.C.C. Guenette, D.P.P. Riley, Hydrogen induced vacancy formation in tungsten. J. Nucl. Mater. **448**, 270–275 (2014). https://doi.org/10.1016/j.jnucmat.2014.02.014
8. Y. Ueda, T. Funabiki, T. Shimada, K. Fukumoto, H. Kurishita, M. Nishikawa, Hydrogen blister formation and cracking behaviour for various tungsten materials. J. Nucl. Mater. **337–339**, 1010–1014 (2005)
9. G.M. Wright, E. Alves, L.C. Alves, N.P. Barradas, P.A. Carvalho, R. Mateus, J. Rapp, Hydrogenic retention of high-Z refractory metals exposed to ITER divertor-relevant plasma conditions. Nucl. Fusion **50**, 55004 (2010)
10. G.M. Wright, M. Mayer, K. Ertl, G. de Saint-Aubin, J. Rapp, Hydrogenic retention in irradiated tungsten exposed to high-flux plasma. Nucl. Fusion **50**, 75006 (2010)
11. M. Yamagiwa, Y. Nakamura, N. Matsunami, N. Ohno, S. Kajita, M. Takagi, M. Tokitani, S. Masuzaki, A. Sagara, K. Nishimura, In situ measurement of hydrogen isotope retention using a high heat flux plasma generator with ion beam analysis. Phys. Scr. **T145**, 14032 (2011)
12. H.Y. Xu, G. De Temmerman, G.-N. Luo, Y.Z. Jia, Y. Yuan, B.Q. Fu, A. Godfrey, W. Liu, Deuterium-induced nanostructure formation on tungsten exposed to high-flux plasma. J. Nucl. Mater. **463**, 308–311 (2015). https://doi.org/10.1016/j.jnucmat.2014.11.039
13. D. Nishijima, M.Y. Ye, N. Ohno, S. Takamura, Formation mechanisms of bubbles and holes on tungsten surface with low-energy and high-flux helium plasma irradiation in NAGDIS-II. J. Nucl. Mater. **329–333**, 1029–1033 (2004). https://doi.org/10.1016/j.jnucmat.2004.04.129
14. G.M. Wright, D. Brunner, M.J. Baldwin, R.P. Doerner, B. Labombard, B. Lipschultz, J.L. Terry, D.G. Whyte, Tungsten nano-tendril growth in the Alcator C-Mod divertor. Nucl. Fusion **52**, 42003 (2012). http://stacks.iop.org/0029-5515/52/i=4/a=042003
15. F. Sefta, K.D. Hammond, N. Juslin, B.D. Wirth, Tungsten surface evolution by helium bubble nucleation, growth and rupture. Nucl. Fusion **53**, 73015 (2013). https://doi.org/10.1088/0029-5515/53/7/073015
16. S. Kajita, N. Yoshida, R. Yoshihara, N. Ohno, M. Yamagiwa, TEM observation of the growth process of helium nanobubbles on tungsten: nanostructure formation mechanism. J. Nucl. Mater. **418**, 152–158 (2011). https://doi.org/10.1016/j.jnucmat.2011.06.026
17. M. Miyamoto, S. Mikami, H. Nagashima, N. Iijima, D. Nishijima, R.P. Doerner, N. Yoshida, H. Watanabe, Y. Ueda, A. Sagara, Systematic investigation of the formation behavior of helium bubbles in tungsten. J. Nucl. Mater. **463**, 333–336 (2015). https://doi.org/10.1016/j.jnucmat.2014.10.098

18. S. Kajita, W. Sakaguchi, N. Ohno, N. Yoshida, T. Saeki, Formation process of tungsten nanostructure by the exposure to helium plasma under fusion relevant plasma conditions. Nucl. Fusion **49**, 95005 (2009). https://doi.org/10.1088/0029-5515/49/9/095005
19. S. Sharafat, A. Takahashi, Q. Hu, N.M. Ghoniem, A description of bubble growth and gas release of helium implanted tungsten. J. Nucl. Mater. **386–388**, 900–903 (2009)
20. S.J. Zenobia, G.L. Kulcinski, Fortungsten and retention of surface pores in helium-implanted nano-grain tungsten for fusion reactor first-wall materials and divertor plates. Phys. Scr. **T138**, 14049 (2009)
21. P.E. Lhuillier, T. Belhabib, P. Desgardin, B. Courtois, T. Sauvage, M.F. Barthe, A.L. Thomann, P. Brault, Y. Tessier, Trapping and release of helium in tungsten. J. Nucl. Mater. **416**, 13–17 (2011)
22. G. De Temmerman, K. Bystrov, R.P. Doerner, L. Marot, G.M. Wright, K.B. Woller, D.G. Whyte, Helium effects on tungsten under fusion-relevant plasma loading conditions. J. Nucl. Mater. (2013)
23. V.S. Subrahmanyam, P.M.G. Nambissan, P. Sen, Helium bubbles in tungsten studied by position annihilation. Solid State Commun. **89**, 523–527 (1994)
24. H. Greuner, H. Maier, M. Balden, B. Boeswirth, C. Linsmeier, Investigation of W components exposed to high thermal and high H/He fluxes. J. Nucl. Mater. **417**, 495–498 (2011)
25. S. Takamura, T. Miyamoto, Y. Tomida, T. Minagawa, N. Ohno, Investigation on the effect of temperature excursion on the helium defects of tungsten surface by using compact plasma device. J. Nucl. Mater. **415**, S100–S103 (2011). https://doi.org/10.1016/j.jnucmat.2010.12.021
26. F. Sefta, N. Juslin, B.D. Wirth, Helium bubble bursting in tungsten. J. Appl. Phys. **114**, 243518 (2013). https://doi.org/10.1063/1.4860315
27. M.J. Baldwin, R.P. Doerner, W.R. Wampler, D. Nishijima, T. Lynch, M. Miyamoto, Effect of He on D retention in W exposed to low-energy, high-fluence (D, He, Ar) mixture plasmas. Nucl. Fusion **51**, 103021 (2011). http://stacks.iop.org/0029-5515/51/i=10/a=103021
28. M.J.J. Baldwin, R.P.P. Doerner, D. Nishijima, K. Tokunaga, Y. Ueda, The effects of high fluence mixed-species (deuterium, helium, beryllium) plasma interactions with tungsten. J. Nucl. Mater. **390–391**, 886–890 (2009). https://doi.org/10.1016/j.jnucmat.2009.01.247
29. T. Shimada, H. Kikuchi, Y. Ueda, A. Sagara, M. Nishikawa, Blister formation in tungsten by hydrogen and carbon mixed ion beam irradiation. J. Nucl. Mater. **313–316**, 204–208 (2003). https://doi.org/10.1016/S0022-3115(02)01447-2
30. G.M. Wright, R.S. Al, E. Alves, L.C. Alves, N.P. Barradas, A.W. Kleyn, N.J. Lopes Cardozo, H.J. van der Meiden, V. Philipps, G.J. van Rooij, A.E. Shumack, W.A.J. Vijvers, J. Westerhout, E. Zoethout, J. Rapp, Carbon film growth and hydrogenic retention of tungsten exposed to carbon-seeded high density deuterium plasmas. J. Nucl. Mater. **396**, 176–180 (2010). https://doi.org/10.1016/j.jnucmat.2009.11.002
31. K. Tokunaga, M.J. Baldwin, R.P. Doerner, D. Nishijima, H. Kurishita, T. Fujiwara, K. Araki, Y. Miyamoto, N. Ohno, Y. Ueda, Nanoscale surface morphology of tungsten materials induced by Be-seeded D-He plasma exposure. J. Nucl. Mater. **417**, 528–532 (2011). https://doi.org/10.1016/j.jnucmat.2011.01.078
32. H.T. Lee, G. De Temmerman, L. Gao, T. Schwarz-Selinger, G. Meisl, T. Höschen, Y. Ueda, Deuterium retention in tungsten exposed to mixed D+N plasma at divertor relevant fluxes in Magnum-PSI. J. Nucl. Mater. **463**, 974–978 (2015). https://doi.org/10.1016/j.jnucmat.2014.11.043
33. M. Yamagiwa, S. Kajita, N. Ohno, M. Takagi, N. Yoshida, R. Yoshihara, W. Sakaguchi, H. Kurishita, Helium bubble formation on tungsten in dependence of fabrication method. J. Nucl. Mater. **417**, 499–503 (2011). https://doi.org/10.1016/j.jnucmat.2011.02.007
34. L. Buzi, G. De Temmerman, B. Unterberg, M. Reinhart, T. Dittmar, D. Matveev, C. Linsmeier, U. Breuer, A. Kreter, G. van Oost, Influence of tungsten microstructure and ion flux on deuterium plasma-induced surface modifications and deuterium retention. J. Nucl. Mater. (2014) Article in Press. http://dx.doi.org/10.1016/j.jnucmat.2014.12.006

35. Y. Zayachuk, M.H.J.t Hoen, I. Uytdenhouwen, G. van Oost, Thermal desorption spectroscopy of W–Ta alloys, exposed to high-flux deuterium plasma. Phys. Scr. **T145**, 14041 (2011). https://doi.org/10.1088/0031-8949/2011/t145/014041
36. T. Tanno, A. Hasegawa, J.C. He, M. Fujiwara, M. Satou, S. Nogami, K. Abe, T. Shishido, Effects of transmutation elements on the microstructural evolution and electrical resistivity of neutron-irradiated tungsten. J. Nucl. Mater. **386–388**, 218–221 (2009). https://doi.org/10.1016/j.jnucmat.2008.12.091
37. H. Watanabe, N. Futagami, S. Naitou, N. Yoshida, Microstructure and thermal desorption of deuterium in heavy-ion-irradiated pure tungsten. J. Nucl. Mater. **455**, 51–55 (2014)
38. D.E.J. Armstrong, X. Yi, E.A. Marquis, S.G. Roberts, Hardening of self ion implanted tungsten and tungsten 5-wt% rhenium. J. Nucl. Mater. **432**, 428–436 (2013)
39. M. Shimada, Y. Hatano, Y. Oya, T. Oda, M. Hara, G. Cao, M. Kobayashi, M. Sokolov, H. Watanabe, B. Tyburska-Puschel, Y. Ueda, P. Calderoni, K. Okuno, Overview of the US-Japan collaborative investigation on hydrogen isotope retention in neutron-irraditated and ion-damaged tungsten. Fusion Eng. Des. **87**, 1166–1170 (2012)
40. B. Tyburska, V.K. Alimov, O.V. Ogorodnikova, K. Schmid, K. Ertl, Deuterium retention in self-damaged tungsten. J. Nucl. Mater. **395**, 150–155 (2009). https://doi.org/10.1016/j.jnucmat.2009.10.046
41. A. Hasegawa, T. Tanno, S. Nogami, M. Satou, Property change mechanism in tungsten under neutron irradiation in various reactors. J. Nucl. Mater. **417**, 491–494 (2011). https://doi.org/10.1016/j.jnucmat.2010.12.114
42. J. Marian, T.L. Hoang, Modeling fast neutron irradiation damage accumulation in tungsten. J. Nucl. Mater. **429**, 293–297 (2012). https://doi.org/10.1016/j.jnucmat.2012.06.019
43. A. Debelle, M.F. Barthe, T. Sauvage, First temperature stage evolution of irradiation-induced defects in tungsten studied by positron annihilation spectroscopy. J. Nucl. Mater. **376**, 216–221 (2008). https://doi.org/10.1016/j.jnucmat.2008.03.002
44. V.S. Voitsenya, M. Balden, A.F. Bardamid, A.I. Belyaeva, V.N. Bondarenko, O.O. Skoryk, A.F. Shtan, S.I. Solodovchenko, V.A. Sterligov, B. Tyburska-Püschel, Effect of sputtering on self-damaged ITER-grade tungsten. J. Nucl. Mater. **453**, 60–65 (2014). https://doi.org/10.1016/j.jnucmat.2014.06.037
45. M. Wirtz, J. Linke, G. Pintsuk, G. De Temmerman, G.M. Wright, Thermal shock behaviour of tungsten after high flux H-plasma loading. J. Nucl. Mater. **443**, 497–501 (2013). https://doi.org/10.1016/j.jnucmat.2013.08.002
46. G. De Temmerman, J.J. Zielinski, S. van Diepen, L. Marot, M. Price, ELM simulation experiments on Pilot-PSI using simultaneous high flux plasma and transient heat/particle source. Nucl. Fusion **51**, 73008 (2011). https://doi.org/10.1088/0029-5515/51/7/073008
47. G. De Temmerman, M.J. Baldwin, D. Anthoine, K. Heinola, A. Jan, I. Jepu, J. Likonen, C. P. Lungu, C. Porosnicu, R.A. Pitts, Efficiency of thermal outgassing for tritium retention measurement and removal in ITER. Nucl. Mater. Energy. (2016). https://doi.org/10.1016/j.nme.2016.10.016
48. Y. Ueda, M. Fukumoto, J. Yoshida, Y. Ohtsuka, R. Akiyoshi, H. Iwakiri, N. Yoshida, Simultaneous irradiation effects of hydrogen and helium ions on tungsten. J. Nucl. Mater. **386–388**, 725–728 (2009)
49. M. Miyamoto, D. Nishijima, Y. Ueda, R.P. Doerner, H. Kurishita, M.J. Baldwin, S. Morito, K. Ono, J. Hanna, Observations of suppressed retention and blistering for tungsten exposed to deuterium–helium mixture plasmas. Nucl. Fusion **49**, 65035 (2009). https://doi.org/10.1088/0029-5515/49/6/065035
50. H.T.T. Lee, A.A.A. Haasz, J.W.W. Davis, R.G.G. Macaulay-Newcombe, D.G.G. Whyte, G. M.M. Wright, Hydrogen and helium trapping in tungsten under simultaneous irradiations. J. Nucl. Mater. **363–365**, 898–903 (2007). https://doi.org/10.1016/j.jnucmat.2007.01.111
51. D. Nishijima, T. Sugimoto, H. Iwakiri, M.Y. Ye, N. Ohno, N. Yoshida, S. Takamura, Characteristic changes of deuterium retention on tungsten surfaces due to low-energy helium plasma pre-exposure. J. Nucl. Mater. **337–339**, 927–931 (2005). https://doi.org/10.1016/j.jnucmat.2004.10.011

52. W.R. Wampler, R.P. Doerner, The influence of displacement damage on deuterium retention in tungsten exposed to plasma. Nucl. Fusion **49**, 115023 (2009). https://doi.org/10.1088/0029-5515/49/11/115023
53. J.F. Ziegler, M.D. Ziegler, J.P. Biersack, SRIM—The stopping and range of ions in matter. Nucl. Instrum. Meth. Phys. Res. Sect. B Beam Interact. Mater. Atoms. **268**, 1818–1823 (2010). doi:http://dx.doi.org/10.1016/j.nimb.2010.02.091
54. J. Rapp, W.R.R. Koppers, H.J.N.J.N. van Eck, G.J.J. van Rooij, W.J.J. Goedheer, B. de Groot, R. Al, M.F. Granswinckel, M.A.A. van den Berg, O. Kruyt, P. Smeets, H.J.J. van der Meiden, W. Vijvers, J. Scholten, M. van de Pol, S. Brons, W. Melissen, T. van der Grift, R. Koch, B. Schweer, U. Samm, V. Philipps, R.A.H.A.H. Engeln, D.C.C. Schram, N.J.J. Lopes Cardozo, A.W.W. Kleyn, M.F. Graswinckel, M.A.A. van den Berg, O. Kruyt, P. Smeets, H.J. J. van der Meiden, W. Vijvers, J. Scholten, M. van de Pol, S. Brons, W. Melissen, T. van der Grift, R. Koch, B. Schweer, U. Samm, V. Philipps, R.A.H.A.H. Engeln, D.C.C. Schram, N.J. J. Lopes Cardozo, A.W.W. Kleyn, Construction of the plasma-wall experiment Magnum-PSI. Fusion Eng. Des. **85**, 1455–1459 (2010). https://doi.org/10.1016/j.fusengdes.2010.04.009
55. G.J. van Rooij, H.J. van der Meiden, M.H.J. 't Hoen, W.R. Koppers, A.E. Shumack, W.A. J. Vijvers, J. Westerhout, G.M. Wright, J. Rapp, Thomson scattering at Pilot-PSI and Magnum-PSI. Plasma Phys. Control. Fusion **51**, 124037 (2009). http://stacks.iop.org/0741-3335/51/i=12/a=124037
56. M. Thompson, A. Deslandes, T.W. Morgan, R.G. Elliman, G. De Temmerman, P. Kluth, D. Riley, C.S. Corr, Observation of a helium ion energy threshold for retention in tungsten exposed to hydrogen/helium mixture plasma. Nucl. Fusion **56**, 104002 (2016). https://doi.org/10.1088/0029-5515/56/10/104002
57. K.O.E. Henriksson, K. Nordlund, A. Krasheninnikov, J. Keinonen, J.K. K. O. E. Henriksson, K. Nordlund, A. Krasheninnikov, The depths of hydrogen and helium bubbles in tungsten: a comparison. Fusion Sci. Technol. **50**, 43–57 (2006). http://jn8sf5hk5v.search.serialssolutions.com/?ctx_ver=Z39.88-2004&ctx_enc=info%253Aofi%252Fenc%253AUTF-8&rfr_id=info:sid/summon.serialssolutions.com&rft_val_fmt=info:ofi/fmt:kev:mtx:journal&rft.genre=article&rft.atitle=The+depths+of+hydrogen+and+helium+bubbles
58. E. Markina, M. Mayer, H.T. Lee, Measurement of He and H depth profiles in tungsten using ERDA with medium heavy ion beams. Nucl. Instruments Methods Phys. Res. B. **269**, 3094–3097 (2011)
59. M. Mayer, SIMNRA, a simulation program for the analysis of NRA, RBS, and ERDA, in ed. by J.L. Duggan, I.L. Morgan, *15th International Conference Application of Accelerators in Research and Industry*, American Institute of Physics Conference Proceedings (1999), p. 541. http://home.rzg.mpg.de/ ~ mam/References.html
60. R.O. Dendy (ed.) *Plasma Physics: An Introductory Course* (Cambridge University Press, 1993)
61. B. Efron, C. Stein, The jackknife estimate of variance, 586–596 (1981). https://doi.org/10.1214/aos/1176345462
62. V. Borovikov, A.F. Voter, X.-Z. Tang, Reflection and implantation of low energy helium with tungsten surfaces. J. Nucl. Mater. **447**, 254–270 (2014). https://doi.org/10.1016/j.jnucmat.2014.01.021
63. X.-C. Li, X. Shu, P. Tao, Y. Yu, G.-J. Niu, Y. Xu, F. Gao, G.-N. Luo, Molecular dynamics simulation of helium cluster diffusion and bubble formation in bulk tungsten. J. Nucl. Mater. **455**, 544–548 (2014). https://doi.org/10.1016/j.jnucmat.2014.08.028
64. H.T. Lee, N. Tanaka, Y. Ohtsuka, Y. Ueda, Ion-driven permeation of deuterium through tungsten under simultaneous helium and deuterium irradiation. J. Nucl. Mater. **415**, S696–S700 (2011)
65. H.T. Lee, A.A. Haasz, J.W. Davis, R.G. Macaulay-Newcombe, Hydrogen and helium trapping in tungsten under single and sequential irradiations. J. Nucl. Mater. **360**, 196–207 (2007). https://doi.org/10.1016/j.jnucmat.2006.09.013

66. M. Miyamoto, D. Nishijima, M.J.J. Baldwin, R.P.P. Doerner, Y. Ueda, K. Yasunaga, N. Yoshida, K. Ono, Microscopic damage of tungsten exposed to deuterium-helium mixture plasma in PISCES and its impacts on retention property. J. Nucl. Mater. **415**, S657–S660 (2011). https://doi.org/10.1016/j.jnucmat.2011.01.008
67. T. Hino, K. Koyama, Y. Yamauchi, Y. Hirohata, Hydrogen retention properties of polycrystalline tungsten and helium irradiated tungsten. Fusion Eng. Des. **39–40**, 227–233 (1998). https://doi.org/10.1016/S0920-3796(98)00157-4

Chapter 7
Conclusion

7.1 Summary of Key Results

7.1.1 Scientific Impact

He plasma exposure is known to lead to the formation of a range of nano-structures in W, such as nano-bubbles, surface pits, and nano-scale "fuzz". However, to date this knowledge is mostly qualitative. This is largely due to the difficulty in measuring sub-surface features such as nano-bubbles with the techniques which have been traditionally used within the field.

The main focus of this thesis has been on filling in some of the gaps in the field by introducing GISAXS as a new method to measure nano-bubble growth. GISAXS is highly complementary to TEM, making it a powerful addition to the repertoire of techniques available to researchers interested in studying plasma-induced nano-scale modification of metals. This work has brought an unprecedented amount of quantitative information about nano-bubble size distributions to the field which, in turn, has provided striking new insights into how nano-bubbles form.

Much of this work has already been published in leading peer-review journals within the field of fusion materials, including "Nuclear Fusion" and the "Journal of Nuclear Materials". This includes many first author studies proof-of-concept study demonstrating the feasibility of GISAXS for nano-bubble formation in W [1], confirmation of the technique's effectiveness via comparison with TEM [2], and a short paper outlining the role of plasma fluence on nano-bubble growth [3]. This work has also been used to support a collaborators' publication, which focussed on nano-bubble formation in the DIII-D tokamak [4]. Recently, the author has also had a further manuscript based on the results presented in Chap. 6 accepted for publication in Nuclear Fusion, and intends to publish further papers relating to the work in Chaps. 4 and 5.

M. Thompson, *Helium Nano-bubble Formation in Tungsten*, Springer Theses,
https://doi.org/10.1007/978-3-319-96011-1_7

The impact of this work is further demonstrated by the large number of collaborators from around the world who have contributed to the work within this thesis. These include external collaborators from Australia, France, Japan, the Netherlands, and the United States. Different stages of this work have been presented at a number of national and international conferences, as well as during invited presentations at institutions in France, Germany, Japan, and the Netherlands.

In this chapter, the main results from this thesis are summarised. Though much has been achieved to date, GISAXS is still very new to the field of fusion materials, and there is much more that can be learned from it. Thus, the latter part of this chapter describes some of the many future opportunities GISAXS may bring to fusion researchers, demonstrating both the great depth and breadth of knowledge it could potentially unlock.

7.1.2 Development and Demonstration of the GISAXS Technique

Chapters 2 and 3 lay the groundwork for the application of GISAXS to the field of fusion materials. In Chap. 2, a detailed GISAXS model is described which has formed the basis of all subsequent GISAXS analysis contained within this thesis. At the time of this writing, the author is the only person with any significant experience working on the use of GISAXS to measure plasma-induced damage in nuclear materials. Given the potential of the technique, and the value of the information it may provide to the ITER project, wider adoption of the technique by the fusion community would go a long way to driving progress within the field. This would be especially important if researchers working at ITER require non-destructive measurements of nano-structure formation in divertor or first-wall tiles.

Chapter 3 compared results from TEM and GISAXS studies looking at the size distribution of nano-bubbles which formed in W exposed to He plasma in the Large Helical Device (LHD). Both TEM and GISAXS results indicated that nano-bubble diameters followed an exponential distribution, with mean values of $\mu = 0.68 \pm 0.04$ nm and $\mu = 0.60 \pm 0.01$ nm, respectively. Nano-bubble depths were also found to be exponentially distributed, with mean depths of $\tau = 8.4 \pm 0.5$ and $\tau = 9.1 \pm 0.4$ for TEM and GISAXS, respectively. This excellent agreement is a clear validation of the GISAXS technique, placing it on a strong foundation for future work.

7.1.3 Effects of Fluence, Temperature, and Transient Heat/Particle Loading on Nano-bubble Formation

Below a temperature of ~900 K, nano-bubble diameters were found to saturate with increasing fluence for samples exposed to He plasma, where nano-bubble diameters were exponentially distributed with $\mu = 0.52 \sim 0.57$ nm for both the MAGPIE and NAGDIS-II linear plasma devices. On the other hand, $\mu > 0.65$ nm nano-bubbles formed in NAGDIS-II above ~900 K. SEM images also reveal the formation of surface pits in samples exposed to He above ~900 K, but not for those with lower exposure temperatures. A similar trend toward larger bubbles for samples above ~900 K was also observed for samples exposed to He plasma in PISCES-A.

Nano-bubble diameter distributions changed significantly in W exposed to an ELMy discharge in the DIII-D tokamak, likely due to the high heat and particle fluxes during ELMs. These could not be fit with simple exponential distributions, instead requiring a superposition of two different probability density functions (one exponential, one log-normal). For most samples, a distinct peak in nano-bubble diameters around ~1 nm emerged, indicating some new mechanism must exist which promotes the formation of relatively small bubbles. This may be a consequence of the rapid precipitation of He during ELMs, driven by the short-lived high He concentrations in the material during an ELM. For W pre-exposed to PISCES-A at 773 K this peak was not observed. For this sample, He nano-bubbles likely reached their saturation density prior to DIII-D exposure, inhibiting the precipitation of smaller bubbles.

7.1.4 Synergistic Effects, He, and H Retention

W samples were exposed to mixed H/He plasma in Magnum-PSI across a range of H/He plasma ratios, sample surface temperatures, with and without heavy-ion pre-irradiation of the W samples. For these experiments, the energy of He ions as they reached the W surface was found to be the dominant factor influencing He retention. A clear minimum energy of 9.0 ± 1.4 eV was found to be required for He to be retained, with He retention increasing sharply above this energy.

GISAXS on samples with high surface temperatures (>1000 K) during He exposure which had not been pre-irradiated with heavy ions found that samples had exponential diameter distributions with a mean diameter of ~0.8 nm. Their size was unaffected by both plasma H concentration and He incident ion energy. Higher levels of retained He did lead to stronger scattering, suggesting higher nano-bubble concentrations.

H retention was strongly influenced by sample temperature, decreasing sharply until ~700 K before levelling-off at higher temperatures. Below 700 K, pre-irradiation with heavy ions was found to increase H retention, but the type of ion (W/Re) did not have a definitive effect.

7.2 Future Opportunities

7.2.1 Using GISAXS to Benchmark Nano-bubble Growth Models

The ability to measure a full nano-bubble size distribution with a single measurement is both one of the greatest strengths and drawbacks of the GISAXS technique. While the advantage of this is self-evident, the "catch" is that determining the nano-bubble diameter distribution function ab nihilo is nothing more than a stab in the dark. In a sense, computational modellers interested in determining the underlying dynamics which drive nano-bubble growth have the opposite problem: they can readily determine what nano-bubble size distributions should occur based on their models, but have little experimental data to verify this work.

From this it should be immediately clear that there is excellent complementarity between the GISAXS and modelling approaches. If modellers were able to determine nano-bubble properties such as diameter distributions (as in [5]), aspect ratios, preferred orientations, depth distributions, and so on, experiments could then be designed based on these models. GISAXS could then be performed on these experimental samples and the results checked for consistency with computational methods. This process of model development and verification would allow modellers to move confidently towards more detailed models at larger scales, where any simplifying assumptions used to enable this transition could be justified on the basis of empirical agreement.

7.2.2 Advanced GISAXS Analysis and Methods

The GISAXS work in this thesis utilises a fairly standard GISAXS setup to measure relatively simple structures (i.e. spheroids). From here a natural next step is to move towards the study of more complex structures.

There are many possible candidates. For instance, the unidentified nano-structures resulting from He plasma exposure in PISCES-A reported in Chap. 4 would make excellent candidates for the next steps in the expansion of GISAXS into the field of fusion materials. Incremental development of the fitting software to solve these problems would greatly enhance the usefulness of the

technique to the field, and the knowledge gained from these problems could easily be applied to other fields where small angle scattering is widely used.

In the author's view, the ideal goal would be to develop GISAXS in order to quantify the properties of nano-fuzz. Given the complexity of these structures this would not be a trivial exercise, so minimising unwanted contributions from surface scattering would be essential here.

One method to simplify this analysis would be to perform an advanced GISAXS technique known as "Anomalous Grazing Incidence Small Angle X-ray Scattering" (hereafter AGISAXS, see [6, 7]). This method allows one to perform a background subtraction on a sample by performing two measurements on the same sample at the same angle at different X-ray energies: one just below the absorption edge of the objects you want to study, and the other just above. Provided that the background signal comes from material where the strength of X-ray scattering does not change substantially between these two energies, the difference in scattering between the two patterns will come almost entirely from the particles of interest.

The problem with this for measuring nano-bubbles or nano-fuzz for fusion is that He does not scatter X-ray appreciably, so it is unrealistic to expect to be able to measure a He contribution, irrespective of how ingenious the setup. However, if part of the sample could be doped with a different metal with a different response to X-rays, and then design an experiment where this other metal is incorporated entirely within the nano-fuzz with nothing remaining in the bulk (by depositing a thin-film which is entirely transformed into fuzz, for instance), then it may be possible to produce an AGISAXS pattern with very little background to contend with, profoundly simplifying analysis.

AGISAXS could also be useful in the context of measuring nano-bubbles. One could create a multi-layered structure where W is co-deposited with some minor dopant. If the choice of dopant is altered between each layer, and the layer thickness is well defined, it would be possible to "tune" the measurement to a given layer by performing AGISAXS about the absorption edge of the dopant of that layer. This would provide information about nano-bubble sizes for a specific depth beneath the surface, and would greatly simplify the process of probing depth profiles [8].

References

1. M. Thompson, P. Kluth, R.P.P. Doerner, N. Kirby, C. Corr, Probing helium nano-bubble formation in tungsten with grazing incidence small angle x-ray scattering. Nucl. Fusion **55**, 42001 (2015). https://doi.org/10.1088/0029-5515/55/4/042001
2. M. Thompson, R. Sakamoto, E. Bernard, N. Kirby, P. Kluth, D. Riley, C. Corr, GISAXS modelling of helium-induced nano-bubble formation in tungsten and comparison with TEM. J. Nucl. Mater. **473**, 6–12 (2016). https://doi.org/10.1016/j.jnucmat.2016.01.038
3. M. Thompson, P. Kluth, R.P.P. Doerner, N. Kirby, D. Riley, C.S.S. Corr, Measuring helium bubble diameter distributions in tungsten with grazing incidence small angle x-ray scattering (GISAXS). Phys. Scr. **T167**, 14014 (2016). https://doi.org/10.1088/0031-8949/2016/T167/014014

4. R.P. Doerner, D.L. Rudakov, C.P. Chrobak, A.R. Briesemeister, C. Corr, G. De Temmerman, P. Kluth, C.J. Lasnier, A.G. McLean, D.C. Pace, R.A. Pitts, O. Schmitz, M. Thompson, V. Winters, Investigation of He–W interactions using DiMES on DIII-D. Phys. Scr. **T167**, 14054 (2016). https://doi.org/10.1088/0031-8949/T167/1/014054
5. F. Sefta, K.D. Hammond, N. Juslin, B.D. Wirth, Tungsten surface evolution by helium bubble nucleation, growth and rupture. Nucl. Fusion **53**, 73015 (2013). https://doi.org/10.1088/0029-5515/53/7/073015
6. B. Lee, S. Seifert, S.J. Riley, G. Tikhonov, N.A. Tomczyk, S. Vajda, R.E. Winans, Anomalous grazing incidence small-angle x-ray scattering studies of platinum nanoparticles formed by cluster deposition. J. Chem. Phys. **123**, 74701 (2005). https://doi.org/10.1063/1.1999627
7. H. Okuda, M. Kato, S. Ochiai, Y. Kitajima, Anomalous grazing incidence small-angle scattering of capped Ge nanodots at the Si K absorption edge. Appl. Phys. Express **2**, 126501 (2009). https://doi.org/10.1143/APEX.2.126501
8. C.S. Corr, S. O'Ryan, C. Tanner, M. Thompson, J.E. Bradby, G. De Temmerman, R.G. Elliman, P. Kluth, D. Riley, Mechanical properties of tungsten following rhenium ion and helium plasma exposure. Nucl. Mater. Energy. **12**, (2017). https://doi.org/10.1016/j.nme.2017.04.012